Characterisation of an FPGA-based Data-Acquisition System for Pulse Height Analysis

SUBMITTED BY

Sebastian Kaiser

Characterisation of an FPGA-based Data-Acquisition System for Pulse Height Analysis

Bachelor Thesis

Institute for Experimental Particle Physics (ETP)
Faculty of Physics
at the Karlsruhe Institute of Technology
Karlsruhe

submitted by

Sebastian Kaiser

Karlsruhe, 11.07.2024

First supervisor: Prof. Dr. Günter Quast
Second supervisor: Dr. Joachim Wolf

ABSTRACT

This study tests the Red Pitaya STEMlab 125-14 for its suitability as a physical data acquisition system for recording γ-spectra with NaI(Ti)- and HPGe-detectors. In addition, the corresponding Multi-Channel-Pulse-Height-Analyzer (MCPHA) software, developed by Pavel Denim, is tested for its usability in the physics lab at the Karlsruhe Institute of Technology. For this purpose, the combination of the Red Pitaya and the MCPHA is compared with the already existing and proven Multichannel Analyzers and based on this comparison, conclusions are drawn about the performance of the Red Pitaya system.

In the course of the study it was shown that the Red Pitaya STEMlab 125-14 is suitable for recording γ-spectra and can replace the outdated, more expensive and larger Multichannel Analyzers in the physics lab. The analysis of the recorded γ-spectra, detected with the NaI(Ti)-detector, indicate that the resulting small non-linearities in the energy calibration and the maximum relative energy resolution for the Red Pitaya system are comparable to those of the Leybold Cassy system. Furthermore, the visualized and analysed measurement data demonstrate that the Red Pitaya is also suitable for resolving the sharp photopeaks of HPGe-detectors and can thereby replace far more complex experimental set-ups.
At the time of the publication of the thesis, the MCPHA represents a suitable data acquisition software for gamma spectroscopy, even though the software does not use the calibration data from the EEPROM memory and is therefore not suitable for measuring precise absolute voltage values. The internal Pulse generator provides the possibility for a wide range of pile-up studies by generating exponentially increasing and decreasing pulses. Due to the open-source and freely expandable MCPHA software, the Red Pitaya STEMlab 125-14 allows to cover a broad field of spectroscopy and other physical applications.

CONTENTS

Abstract ii

1 Introduction to the Red Pitaya STEMlab 125-14 1
- 1.1 Built-in Technology . . . 1
- 1.2 Built-in Oscilloscope and Signal Generator in OS 2.00-30 . . . 2
- 1.3 Introduction to MCPHA by Pavel Denim . . . 3
  - 1.3.1 Spectrum-Analyzer . . . 4
  - 1.3.2 Pulse Generator . . . 5
  - 1.3.3 Oscilloscope . . . 6

2 Oscilloscope and Signal Generator 7
- 2.1 Analysis of the ADC Linearity Based on the DC Voltage Behaviour in the 0-1V Range . . . 7
- 2.2 Analysis of the Pulse Generator . . . 12

3 Theory behind the Analysis of Radioactive Spectra 20
- 3.1 Physics behind Radioactive Decay . . . 20
- 3.2 Functionality of Radiation Detectors . . . 24
  - 3.2.1 NaI(Ti)- Scintillation Counter . . . 24
  - 3.2.2 HPGe- Semiconductor Detector . . . 25
  - 3.2.3 Energy Resolution . . . 26
  - 3.2.4 Signal Processing . . . 27
    - 3.2.4.1 Signal Form . . . 27
    - 3.2.4.2 Signal Processing and Digitisation . . . 27
- 3.3 Methods to Analyze the Recorded Spectra . . . 28
  - 3.3.1 Recorded Spectra . . . 28
  - 3.3.2 Mathematical Foundations . . . 29
    - 3.3.2.1 Maximum Likelihood . . . 29
  - 3.3.3 Negative Log-Likelihood NLL . . . 29
  - 3.3.4 Binned Likelihood Fit . . . 30
  - 3.3.5 Error Estimation . . . 30
  - 3.3.6 Goodness of Fit . . . 31
  - 3.3.7 Parameter Estimation in kafe2 . . . 31
    - 3.3.7.1 Fit Function . . . 31
    - 3.3.7.2 Fitting Procedure . . . 32

4 Comparison of Red Pitaya and the Leybold Cassy System 34
- 4.1 Experimental Set-Up . . . 34
- 4.2 Recording of the γ-Spectra and Energy Calibration . . . 35
- 4.3 Comparison of the Relative Energy Resolution Φ of the Red Pitaya/MCPHA and the Leybold Cassy System . . . 39

5 Comparison of Red Pitaya and the MCA-System by Fast ComTec 41
5.1 Experimental Set-Up . . . 41
5.2 Comparison of the Relative Energy Resolution Φ of Red Pitaya/MCPHA and the FAST ComTec System . . . 42
5.3 Comparison of Red Pitaya STEMlab 125-14 Low Noise and Red Pitaya STEMlab 125-14 . . . 44

6 Conclusion and Outlook 46

A Program Code, Tables & Plots 47
A.1 Example of Analysis Code for Photopeaks . . . 47
A.2 Measurement Tables . . . 50
A.2.1 Chapter 1 - Analysis of the ADC linearity . . . 50
A.2.2 Chapter 1 - Analysis of the Pulse Generator . . . 50
A.3 Additional Plots . . . 53
A.3.1 Chapter 4- Comparison of Red Pitaya and the Leybold Cassy System . . . 54
A.3.1.1 Energy Calibration . . . 54
A.3.1.2 Comparison of Relative Energy Resolution Φ . . . 67
A.3.2 Chapter 5 - Comparison of Red Pitaya and the MCA-System by FAST ComTec . . . 69

B Auto DC-Calibration in OS 2.00-30 71

Bibliography 82

Acknowledgement 84

CHAPTER 1

INTRODUCTION TO THE RED PITAYA STEMLAB 125-14

Within this chapter, a brief introduction to the Red-Pitaya STEMlab 125-14 is given, which technical components are installed and also the applications used on it for this study are briefly explained. For a more detailed description and functionality of the technical components, please refer to the Red Pitaya documentation [Doc] and external specialised literature or open sources from the Internet, which are mentioned below.

1.1 Built-in Technology

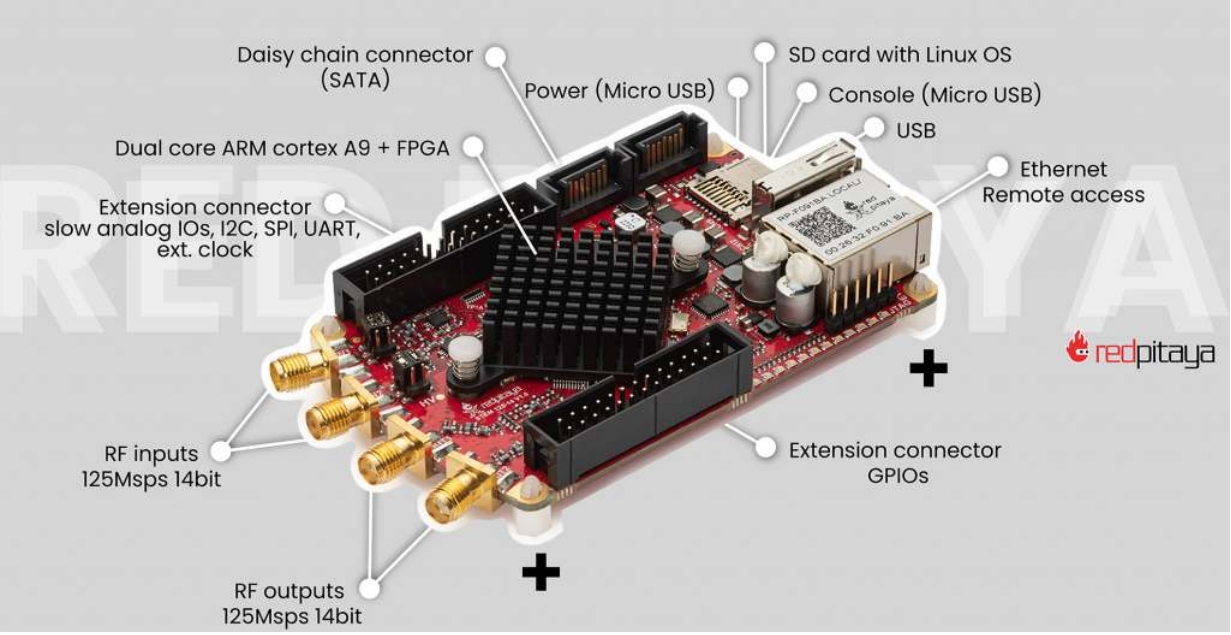

Figure 1.1: Product view of the Red-Pitaya STEMlab 125-14 with a description of the installed hardware (Figure is taken from [ST125-14])

The STEMlab 125-14 is distributed by Red Pitaya and is described as a powerful and precise open-source multifunction measuring device. It is intended to replace expensive and bulky laboratory equipment and is mainly designed for a variety of applications in research and teaching and provides the possibility of free programming, specific technical extensions and customizations.

The board is a System-on-a-Chip (SoC), based on the Xilinx Zynq 7010 SoC FPGA[1] module

[1] „Field Programmable Gate Arrays (FPGAs) are integrated electronic components that can be programmed to realise any type of digital circuits [...].“ [PC19]

with ARM CORTEX A9 Dual Core processor and 512 MB DDR3L SDRAM (cf. Figure 1.1). Furthermore, it has WI-FI, Ethernet and USB 2.0 interfaces and two built-in RF inputs and outputs with a sample rate of 125 Msps each at an ADC resolution of 14 bits. As noted in the documentation [DocHW], there are simplified hardware schematics for the Red Pitaya and a listing of the built-in hardware, but the Full Hardware schematics are not publicly accessible, so it is not actually a full open source project. A complete table of the installed hardware, part numbers and characteristics of the built-in Hardware can be found under [DocHW].

On the software side, the STEMlab 125-14 is well equipped. It offers the option of running C and Python applications and open FPGA-programming as well as the option of developing your own operating system. In addition, the in-house Debian-based Linux operating system "Red Pitaya OS" offers the option of using pre-installed web-based applications such as the Oscilloscope & Signal Generator or the Spectrum Analyzer. Instructions for all these applications as well as a Developer Guide can be found with a list of available applications under [Doc]. The functionality of the Oscilloscope & Signal Generator in OS version 2.00-30 is explained in more detail below. It should be noted that a detailed Quick-Start Guide for setting up the Red Pitaya can be found under [DocSW].

1.2 Built-in Oscilloscope and Signal Generator in OS 2.00-30

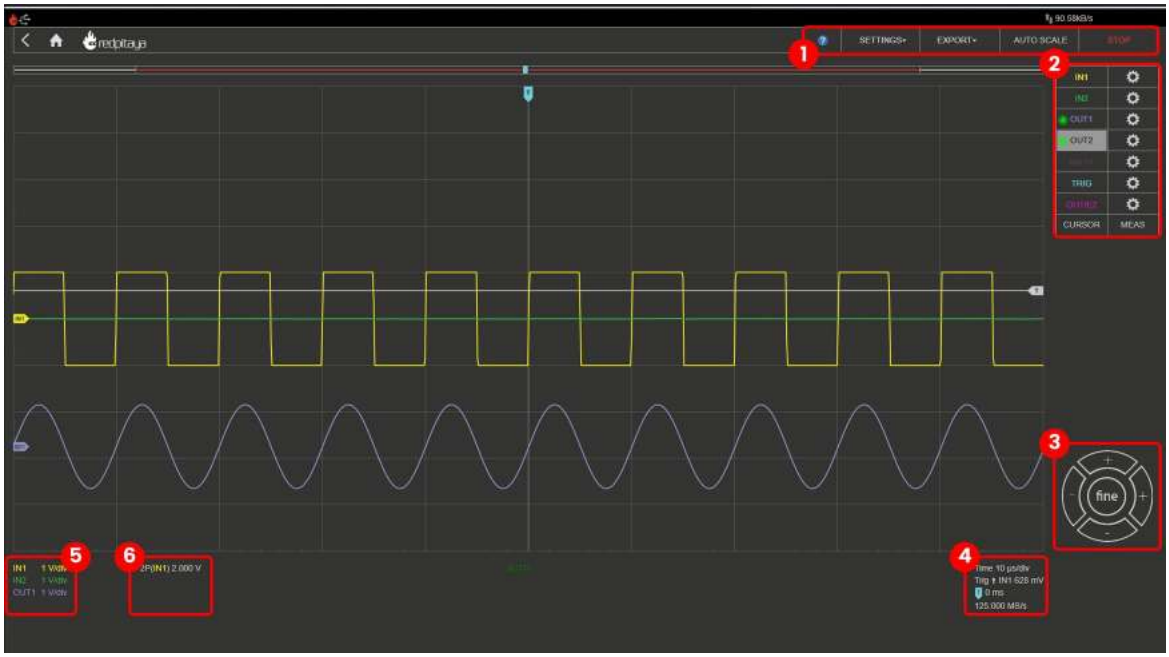

Figure 1.2: GUI of the Oscilloscope & Signal generator with pre-configured signal forms (Figure is taken from [DocSW])

The Oscilloscope & Signal Generator application 1.2 used under OS 2.00-30 is one of the most popular applications of the Red Pitaya. According to the manufacturer, the oscilloscope promises a bandwidth of 50 MHz, with a resolution of 14 bit and a memory depth of 16k sam-

ples.[2] The two possible RF inputs are DC coupled and it should be noted that the input range depends on the jumper orientation and therefore covers a range of ±1 V or ±20 V.

The Signal Generator also provides a resolution of 14 bits, with a frequency range of 0-50 MHz, DC-coupled and a signal buffer[3] of 16k samples. However, it should be noted that the output range is only ±1 V.
It is also important for developers to know, that the complete source code is published on GitHub [Git-RP]. There is also a comprehensive documentation of the functions of the application, which is linked under [OscSig], making it easier to use. With the help of these instructions it is possible to reproduce the settings of all forthcoming measurement series.

1.3 Introduction to MCPHA by Pavel Denim

The analysis tool used in this study to record the γ-spectra is the Multichannel-Pulse-Height-Analyzer (MCPHA), developed by Pavel Denim. It is a freely accessible tool for recording spectra, oscillograms and generating signals with the Red Pitaya. The source code of the application is available via GitHub [GitHub-MCPHA] and is continuously updated and adapted, thus offering the possibility of customization. The developer also provides a brief description of the software, a Quick-Start Guide and an explanation of the sequence of hardware components used. During the development of this thesis, continuous version updates have been made and a version specialised for the use in the physics lab at the Faculty of Physics at the Karlsruhe Institute of Technology has also been published by Prof. Dr. Günter Quast [GitLab-MCPHA]. This version is the one used in the study and has been designed for physical applications and provides, among other things, axis labelling in physical units.[4] The possible application settings are briefly explained below so that all subsequent measurement series can be reproduced.

[2] In the case of an oscilloscope, memory depth is defined as the maximum possible recording length for an acquisition and depends on the relationship „Record length= Sample Rate · Acquisition Time“, a higher memory depth is therefore directly linked to a better resolution (cf. [RS]).

[3] In this case it is understood as a data buffer and thus as a memory for the temporary storage of data, in this case, voltage values.

[4] A description of the installation of the software is available under [GitLab-MCPHA].

1.3.1 Spectrum-Analyzer

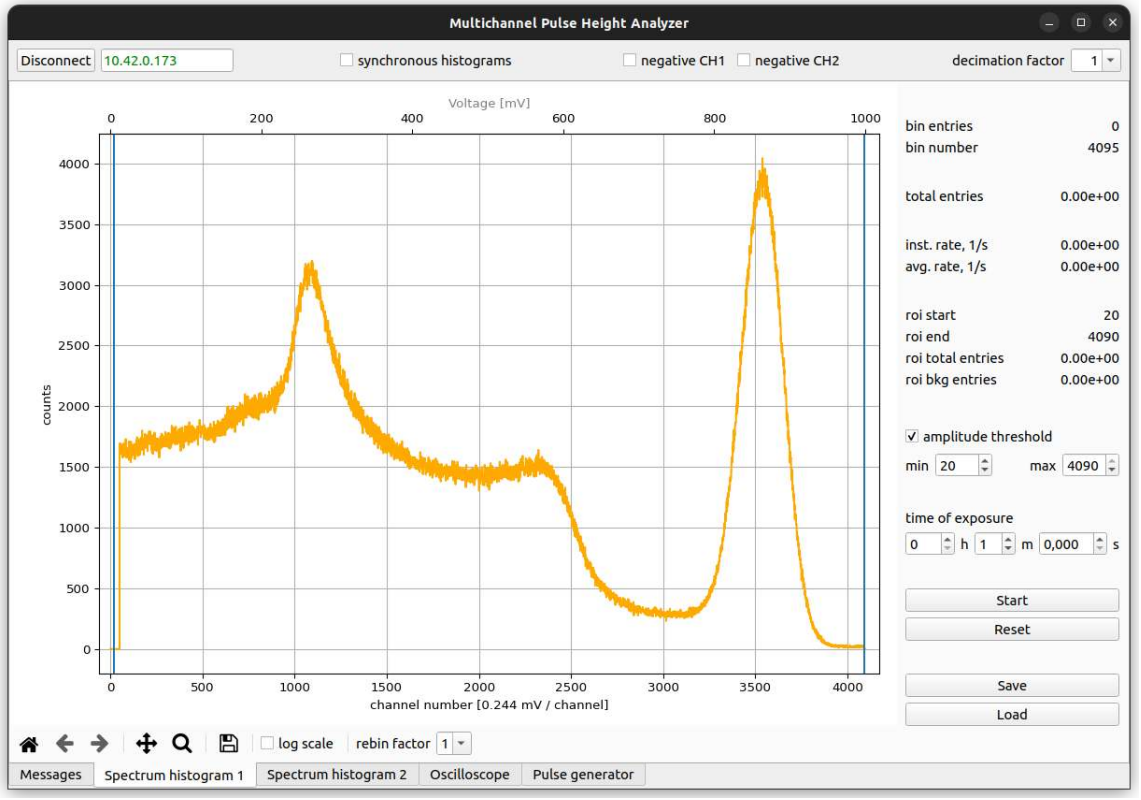

Figure 1.3: GUI of the Spectrum-Analzser and the measured γ-spectrum of Cs137

The MCPHA offers the option of recording spectra simultaneously via the IN1 and IN2 inputs (see Figure 1.3). Pulses recorded via the analog-to-digital converter (ADC) are filtered using CIC[5] and FIR[6] algorithms and then histogrammed according to their height. The determination of the height is based on the difference measurement between the stored ADC count when the signal rises and the ADC count when the signal falls again and is therefore based on a simple change in the sign of the 1st derivative of the signal curve. This difference value is then histogrammed. The adjustable decimation factor can be used to set the sampling rate in the CIC-filter and thus how many of the recorded samples are averaged over and stored as a single value in the ring buffer[7]. The decimation factor 1 is always used when recording the γ-spectra. The version used of the MCPHA limits the analysis to 4096 channels and thus 12 bit resolution; although 16384 channels are possible due to the theoretical 14 bit resolution. The reasons for this are to be found in the signal noise, as the additional two subdivisions of the 14-bit resolution are in the noise range. The measurement series are limited to the input range of $\pm 1\,\mathrm{V}$ in the Low Voltage Mode and only differences up to $\Delta U = 1\,\mathrm{V}$ are correctly histogrammed in the spectrum. This means that no rebinning is done and the factor is always left at 1. Setting the amplitude threshold is particularly important for recording the spectra; this is usually set to the range 50 to 4000 to prevent high count numbers at the edges of the

[5] Cascaded-Integrator-Comb filter, which is integrated in the FPGA and in this case serves as a decimation filter to enable the sampling rate to be changed.

[6] Finite-Impulse-Response filter, i.e. a digital filter with a finite impulse response, which drops to 0 after a certain time. These filters are used for noise suppression or signal-smoothing.

[7] Memory for the temporary storage of data, whereby data can be read in and out according to the first-in-first-out principle and the oldest data is overwritten when the memory is full.

spectra, which occur in the upper range of the spectra mainly due to exceeding the maximum detectable voltage difference and in the lower range due to small pulses without any physical significance (cf. Chapter 4.2). The recorded histograms can be saved as .hst files and read out preferably with the -Python programming language for visual representation and analysis.

1.3.2 Pulse Generator

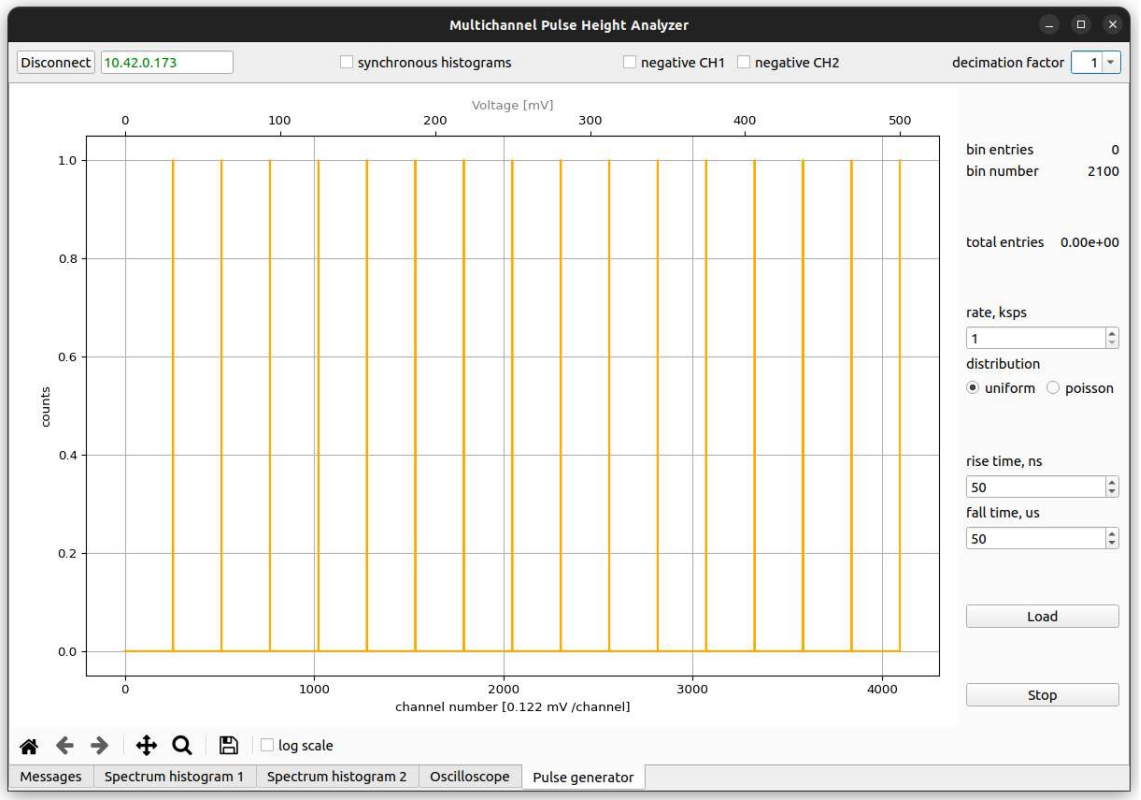

Figure 1.4: GUI of the Pulse generator and an illustrative spectrum with pulses spaced 256 channels apart.

The integrated Pulse generator 1.4 offers the option to generate exponentially rising or falling pulses and output them via two IIR filters[8] and a digital-to-analog converter (DAC) by OUT1. The shape of these pulses can be defined using the rise time in ns and the fall time in μs. The amplitudes or voltage maxima of these pulses are determined by the position in the spectrum and are therefore dependent on the channel number, whereby the 4096 channels allow voltage maxima of up to 500 mV. The rate in kilo samples per second (ksps) can also be used to set the number of pulses per second. In the case of the uniform distribution setting, this corresponds to the actual time interval between the pulses; in the case of the poisson distribution, it corresponds to the expectation value of the time between two pulses, whereby the effects of pile-up[9] can be analysed. Which pulse is chosen in the spectrum is determined by a random generator. A

[8] Infinite-Impulse-Response filter, whose impulse response does not become 0 over time and is often used as a high-pass or low-pass filter in signal processing.

[9] In nuclear physics, pile-up is defined as the occurrence of several events, in this case voltage pulses, which occur within such a short time that it is shorter than the time width of a single signal and as a result the two signals overlap. As a result, the pulse height of the individual pulses cannot usually be determined correctly and they are therefore histogrammed incorrectly in the spectrum.

predefined script for creating your own spectra to load into the Pulse generator can be found under [GitLab-MCPHA]. Chapter 2.2 examines this Pulse generator in more detail.

1.3.3 Oscilloscope

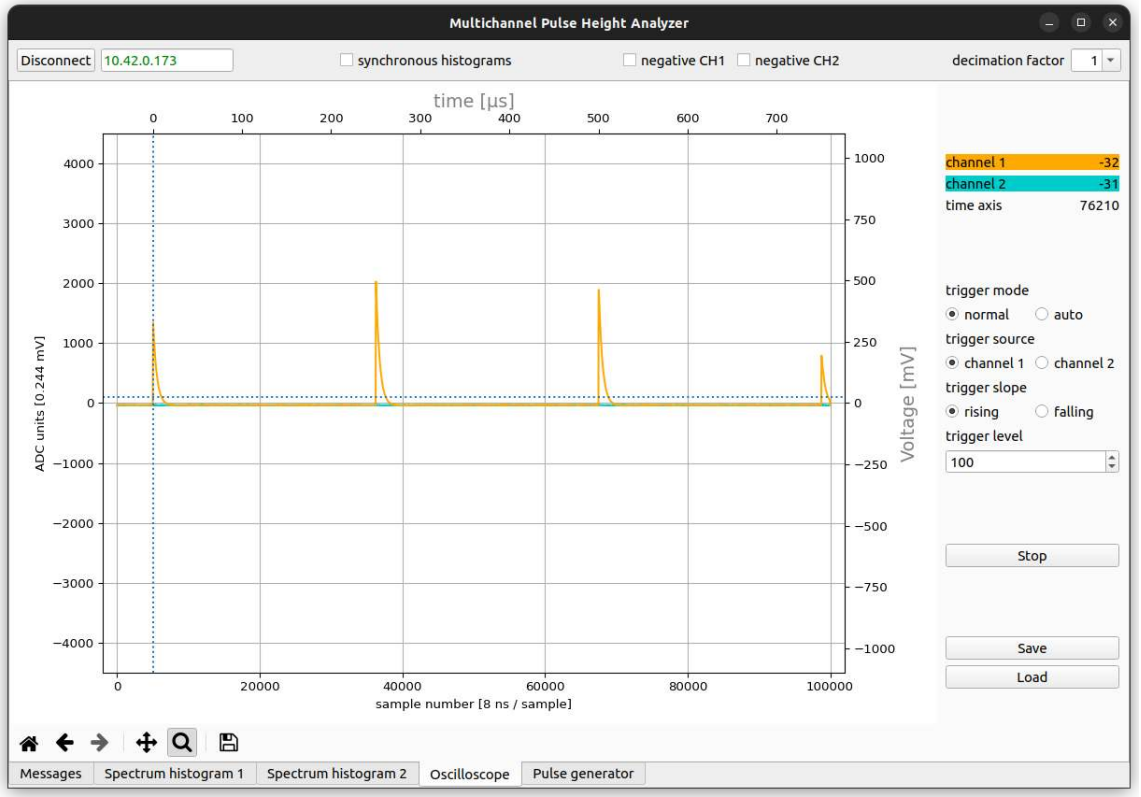

Figure 1.5: GUI of the Oscilloscope and generated pulses by the Pulse generator.

The integrated Oscilloscope can simultaneously display the signals that are recorded via IN1 and IN2, similar to the Spectrum Analyzer processed via CIC- and FIR-filters. For the version of the MCPHA in use, the displayable range covers voltages of $\pm 1\,\mathrm{V}$. However, the range $\pm 20\,\mathrm{V}$ (High-voltage mode) can also be displayed, although the axis labelling would have to be changed here. At that version, it only provides basic functions and is often used in the subsequent chapters to view the pulse shapes when recording the spectra and to analyze pile-up effects. As the inputs of the Red Pitaya record 125 million samples per second, a sample is recorded every 8 ns. The decimation factor can again be used to define the averaging over the samples and simple trigger conditions can be set using the trigger mode. This can be done via the trigger level and so the Oscilloscope only starts recording and displaying once this set threshold value has been reached. The Oscilloscope data can also be saved and read out, a predefined script for reading out the data can also be found under [GitLab-MCPHA].

CHAPTER 2

OSCILLOSCOPE AND SIGNAL GENERATOR

This chapter examines and compares the oscilloscopes and signal/pulse generators in the Low Voltage Mode of the two applications described in the previous chapter. Particular attention is paid to the usability for student physics labs. For the recording of γ-spectra and the usability of the Red Pitaya STEMlab 125-14 as a pulse height analyzer for energy calibration, it is essential that the ADCs form an almost exact linear relationship between the input and output variables. In this context, the Red Pitaya is also analysed for Offset[1] and Gain error[2] of the ADCs. Therefore this chapter is intended to provide an overview on how the system works, which is not specific to any particular application purpose.

2.1 Analysis of the ADC Linearity Based on the DC Voltage Behaviour in the 0-1V Range

The Red Pitaya STEMlab 125-14 is supplied by the manufacturer with the ADCs and DACs already calibrated (factory-Calibration). To test this calibration, a DC voltage source is connected to the Red Pitaya and the recognised voltages are read out in the oscilloscope. The measurement setup is shown in Figure 2.1. Using a laboratory power supply, the outgoing voltage can be set by a rotary control and checked with a precision of three decimal places by using a True-RMS multimeter connected in parallel to the Red Pitaya. For the Oscilloscope application in OS 2.00-30 a total of three series of measurements were recorded. One with the manufacturer's calibrated ADC/DAC settings, one with the Default uncalibrated ADC/DAC settings and one with the Auto DC calibration settings. The procedure for your own Auto-DC calibration with a laboratory power supply unit is described in appendix B and can be understood as a calibration manual.

[1] The Offset can be described as the voltage value that the uncalibrated ADC outputs when the voltage 0 V is applied to it.

[2] Gain error refers to the difference between the slope of the uncalibrated ADC's transfer function and that of the ideal ADC. The Offset- and Gain error can usually be corrected by software calibration.

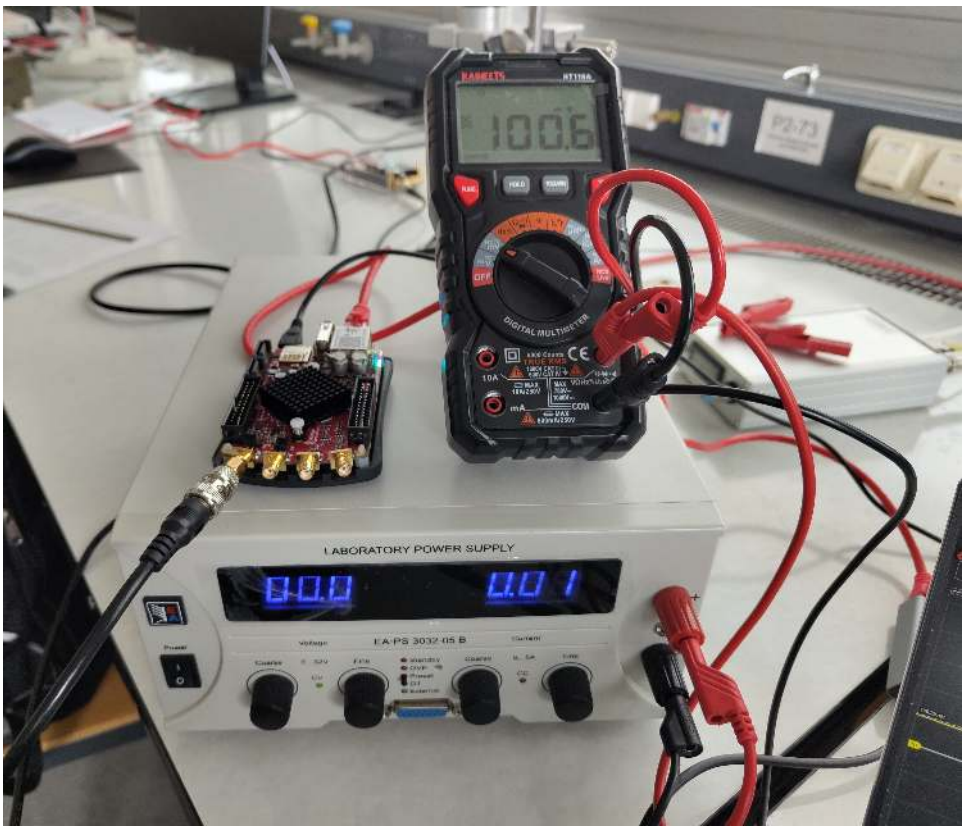

Figure 2.1: Experimental set-up for the series of measurements with DC voltage. The picture shows the laboratory power supply unit used, the Red Pitaya STEMlab 125-14 and the True-RMS multimeter.

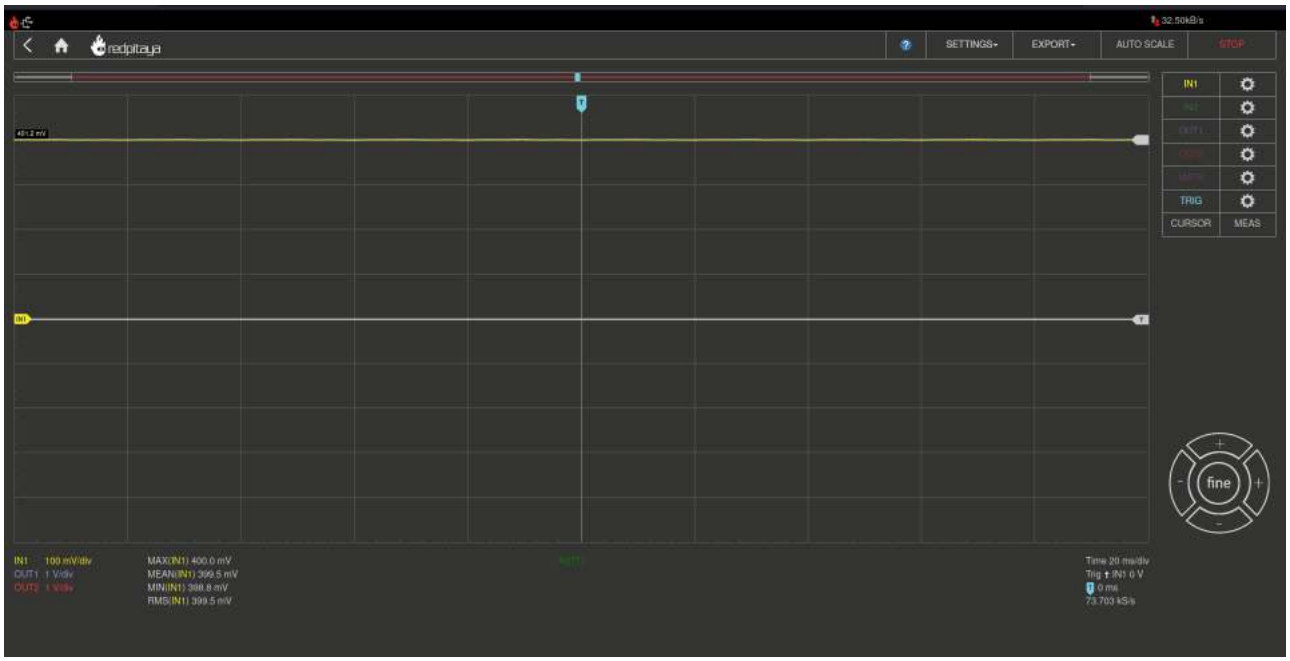

Figure 2.2: Example of a DC voltage measurement with the Oscilloscope under OS 2.00-30.

To record the measurement data, the RMS value or MEAN is read out in the Oscilloscope application via the MEAS function for IN1 (see Figure 2.2), so that this value does not fluctuate

too much. The time axis was set to 20 ms/div in order to be able to read it out more easily, as this also changes the number of samples per second. Table A.1 shows the measurement results[3].
It should be noted that several calibration processes were carried out for the Auto DC calibration, which nevertheless lead to slightly different results in the calibration parameters despite the use of the same reference voltages and cables.

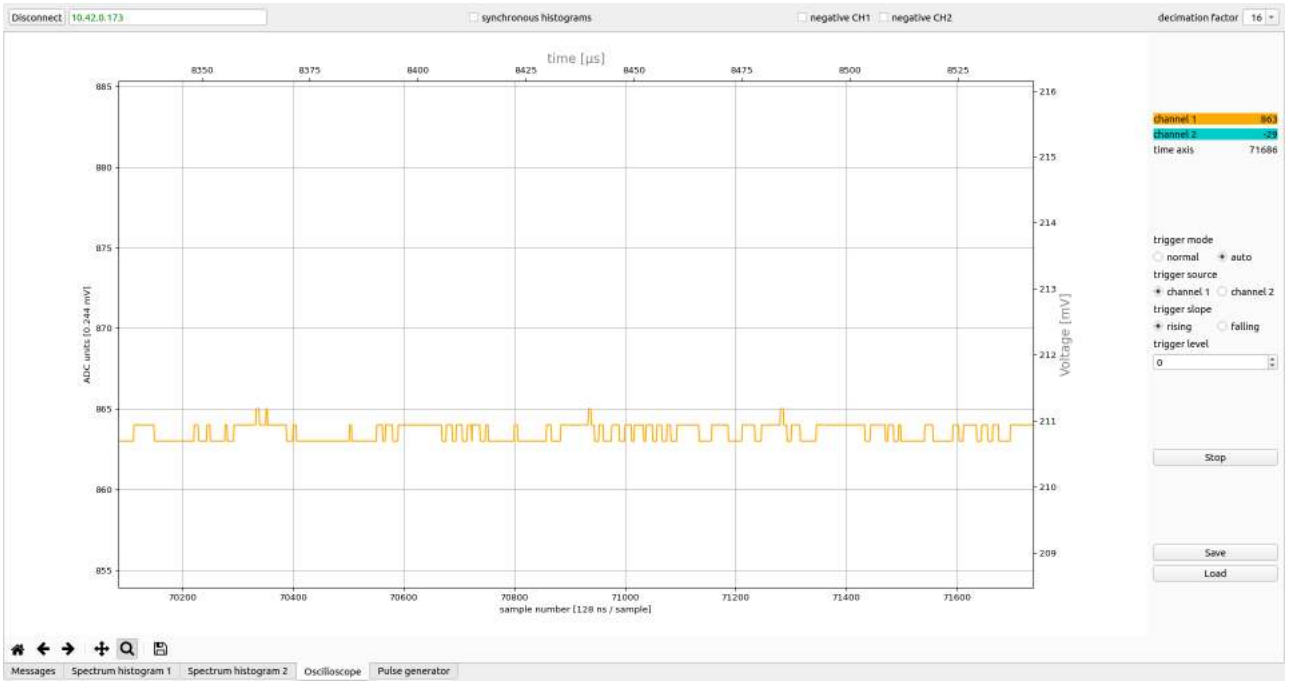

Figure 2.3: Example of a DC voltage measurement with the Oscilloscope of the MCPHA by Pavel Denim.

The same experimental set-up 2.1 is used to analyse the oscilloscope of the MCPHA. For the measurements with the MCPHA, it is important to note that these were carried out with a decimation factor of 16 (see Figure 2.3), as the values are therefore relatively stable. In contrast to the oscilloscope application in OS 2.00-30, there are no other functions for reading out values apart from the option of zooming in and thus better estimate the value.
Within this series of measurements, it was found that the MCPHA does not use any calibration data. If the Red Pitaya STEMlab 125-14 is calibrated under OS 2.00-30, OS 2.00-23, OS 1.04-28 or OS 1.04-18 according to B, this does not influence on the voltage values in the MCPHA and the result is always the same as in Table A.2. At the time of publication of this study, the MCPHA is therefore not suitable for absolute measurements of voltages. Adding the possibility to use calibration data would change this.
To estimate the extent of the non-linear effects of analog to digital conversion and to check whether a linear relationship exists despite the strong deviations from the actual input voltages, the measured values from Tables A.1 and A.2 are plotted against the actual input voltages. The results of this are shown in Figure 2.4.

[3] Due to the limitation of the input, the value at an input of 1000 mV for Auto DC calibration is not correct, as this is above the maximum voltage and all detected voltage values above this limit are displayed as 1000 mV.

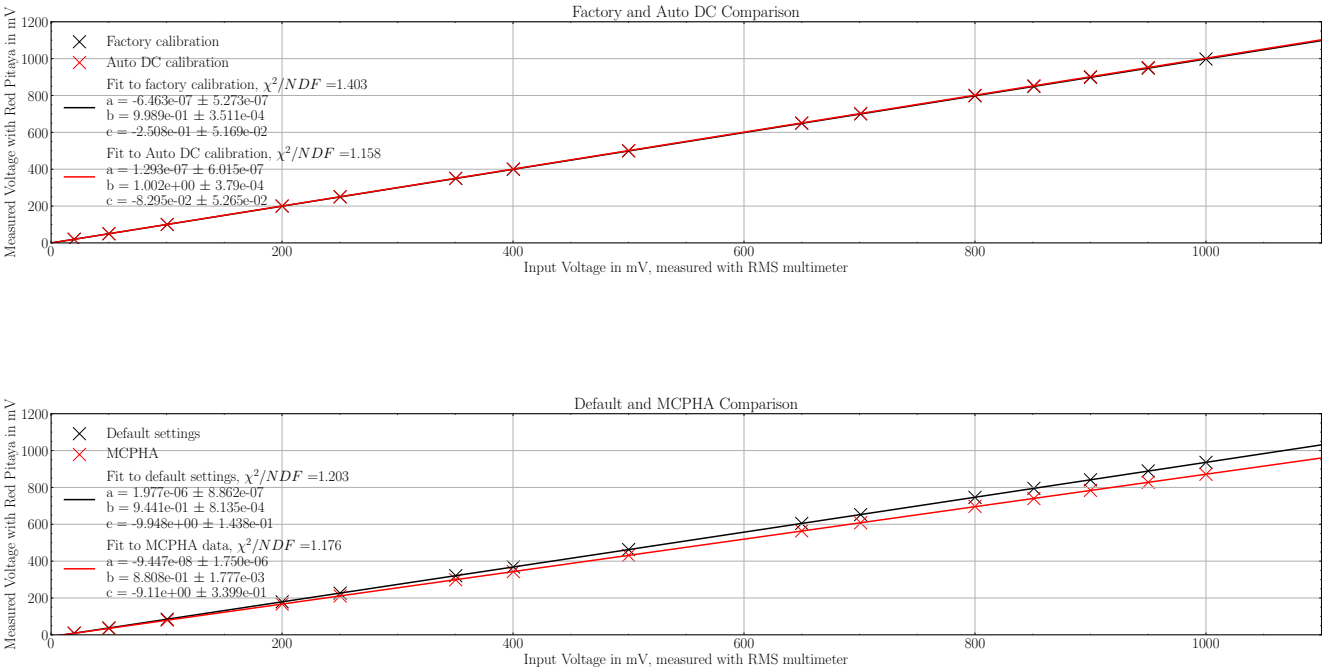

Figure 2.4: Voltages measured with the Red Pitaya STEMLab 15-14 plotted against the voltage reference.

The fitting tool used here is *kafe2* [kafe2], whereby the χ^2-cost function was used. Further details on the basics of parameter estimation and the -package *kafe2* can be found in Chapter 3.3. As can be seen, the effect of non-linearity is modelled by a quadratic term $f(U) = a \cdot U^2 + b \cdot U + c$. The values of the fitted parameters and their uncertainties are given in Figure 2.4. With the help of the *XYFit* from *kafe2*, both the reading errors on the multimeter as errors on the values of the x-axis and the reading errors on the GUI of the Red Pitaya applications as errors on the values of the y-axis could be included in the fit as systematic errors.[4] In any case, the non-linearity accounts for a very small part of the measured voltages compared to the linearity. It can also be seen that the uncertainties determined by *kafe2* are so large that the confidence interval of the parameter a and thus that of the non-linearity includes the case for a=0 for the measurement with the Oscilloscope of the MCPHA and the measurement with the Auto DC Calibration in OS 2.00-30. In the case of the measurements in OS 2.00-30 with default and factory settings, the value a=0 is also close to the confidence intervals.

The Gain-factor of the factory calibration settings can be reproduced using the parameter

[4] The systematic error that arises due to the inaccuracy of the multimeter is not taken into account in this study. The manufacturer Kaiweet specifies the error on the display of the multimeter with up to a maximum of ±0.5% on the measured value ± 3 digits in the first decimal place. Whereby this specification of uncertainty is given over the entire possible measuring range from 0.1 mV to 1000 V and are overestimated in case of doubt. For the considered range from 20 mV to 1000 mV, these errors are therefore quite small. The measurement was also checked with two other RMS-multimeters, which both displayed the same voltage value each time. Another reason for not taking this uncertainty into account is the fact that the Red Pitaya has to be calibrated using a multimeter and that no information about the accuracy of the input voltage could be specified during this process. The accuracy of the multimeter thus also influences the voltage detection of the Red Pitaya. In addition, the systematic error in the accuracy of the y-data is unknown, since these are based on the calibration. Red Pitaya only provides information on DC Offset error and Gain error, which are specified as $< 5\%$ and $< 3\%$ respectively [DocHW]. To conclude, the values of χ^2/NDF shown in Figure 2.4 indicate that the errors on the x- and y-data have been correctly estimated and the reading error can be interpreted as the dominant uncertainty.

b, as the parameter b acts as a straight line slope. The ratio of the parameter b of the factory calibration to that of the default settings, and therefore Gain 1, reproduces the Gain factor of the factory calibration. This results in a value of

$$\text{Gain} = \frac{b_{\text{factory}}}{b_{\text{default}}} = 1.05814 \pm 0.00098. \tag{2.1}$$

This results in a relative deviation of 0.21% from the actual value $\text{Gain}_{\text{factory}} = 1.05587$.
The Offset parameter of the factory calibration settings can also be reproduced using the default measured voltage values. As measurements were taken within the Low Voltage mode, i.e. in the range from $-1\,\text{V}$ to $1\,\text{V}$, the 14-bit resolution of the Red Pitaya results in a resolution of 13 bits for the 0-1 V range and therefore nominally $\frac{1000\,\text{mV}}{2^{13}} \approx 0.122\,\text{mV}$ per ADC unit . The measured offset is $(-9.95 \pm 0.14)\,\text{mV}$ and therefore simple division results in an estimated ADC Offset of

$$\text{Offset} = -81.51 \pm 1.15. \tag{2.2}$$

The actual value, which is -81, is therefore within the confidence interval. At the time of publication of this study, the Gain-factors and Offsets of the factory calibration of a total of 4 Red Pitaya STEMlab 125-14 could be read out, resulting in an average of

$$\hat{\text{Gain}}_{\text{IN1}} = 1.05508 \pm 0.003 \tag{2.3}$$

$$\hat{\text{Offset}}_{\text{IN1}} = -114.0 \pm 40.9 \tag{2.4}$$

$$\hat{\text{Gain}}_{\text{IN2}} = 1.05494 \pm 0.002 \tag{2.5}$$

$$\hat{\text{Offset}}_{\text{IN2}} = -65.75 \pm 29.52. \tag{2.6}$$

These results of the measurements with the Default settings in OS 2.00-30 and the measurements with the oscilloscope of the MCPHA thus provide direct information about the quality of the installed electronic components. It is therefore not possible to use the oscilloscope integrated in the MCPHA as a reliable measuring instrument in physics labs without using the calibration data from the EEPROM memory. Even a simple scaling of the y-axis (voltage axis) within the GUI of the MCPHA, using the average Gain and Offset results, would only produce adequately accurate measurement results, if the voltage Offset between the Default measurement and the MCPHA measurement would be comparable for every single Red Pitaya STEMlab 125-14, and most important the ratio of the straight line slopes barely varies between the individual devices. The two calibration parameters can also be adjusted independently using the manual calibration function, as explained in appendix B.

It is also possible to perform an auto- as well as a manual frequency calibration. This was not done for a number of reasons. First because no very precise, freely adjustable frequency generator with different signal shapes was available and secondly because frequency analysis is not essential for the main part of this study. The behaviour of the Red Pitaya STEMlab 125-14 with AC voltage in the 0-1 V range was also investigated with the Oscilloscope in OS 2.00-30 for various frequencies of a sine-wave signal. However, it was not possible to examine the entire specified bandwidth of 50 MHz, as the signal generator that was used was only able to send stable signals with frequencies up to 6 MHz and the multimeter could only detect the voltage correctly up to 1 MHz. In this range up to 1 MHz, the Red-Pitaya was able to display the signal without any problems and correctly detected and displayed the voltage amplitude and the frequency.

2.2 Analysis of the Pulse Generator

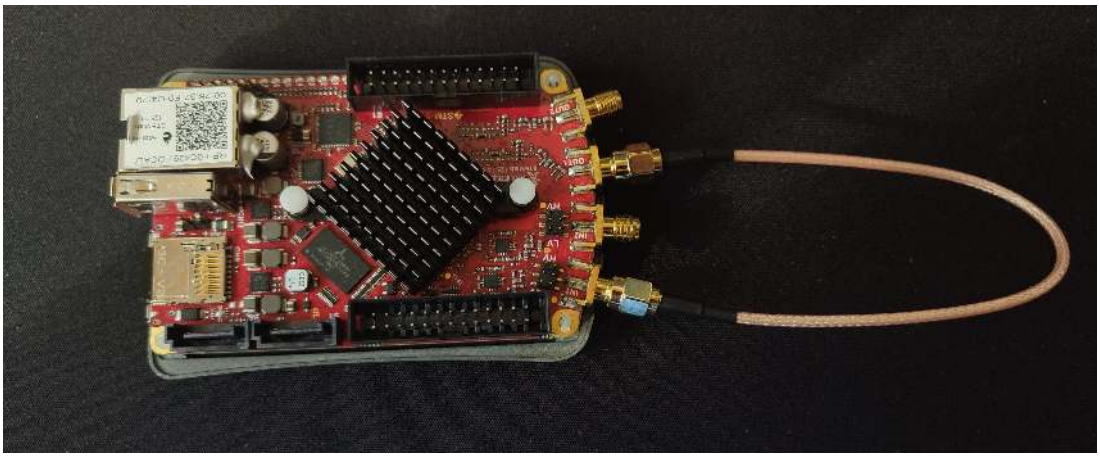

Figure 2.5: Set-up for analysing the Pulse generator of the MCPHA by Pavel Denim.

This section analyses the Pulse generator of the MCPHA. The set-up used for this is shown in Figure 2.5. OUT1 is connected to IN1 via an SMA-cable, so that the pulses of the signal generator can be displayed in the spectrum. Since pulses with a defined exponential rise- and fall time can be generated within the Pulse generator, the aim of this chapter is to describe the range of the pulse rate in which these can be correctly recognised.
There are several aspects to consider here. Firstly, the distance between two pulses in the signal generator corresponds to half the distance in the spectrum of IN1, as the signal generator has a nominal resolution of 0.122 mV per channel on a total of 4096 channels and the spectrum has a nominal resolution of 0.244 mV per channel on a total of 4096 channels. In addition, it was shown in the previous chapter that the MCPHA does not access the calibration data in the EPROM memory, as both ADC and DAC calibration data are used here, which can lead to large shifts.
For this reason, it is not the absolute positions in the spectrum that are analysed, but the relative distances to each other and the shifts of the absolute positions for various fall times as well as pulse rates. For this purpose, 16 pulses are loaded into the spectrum of the MCPHA at a distance of 256 channels from each other. In theory, this corresponds to distances of 31.25 mV and should lead to distances of 128 channels in the spectrum of the MCPHA. It can be assumed that for correct evaluation of the pulses, there must be no or minimal overlap of the pulses. Therefore

$$\kappa = \text{fall time} \cdot \text{rate} < 1 \tag{2.7}$$

must apply.

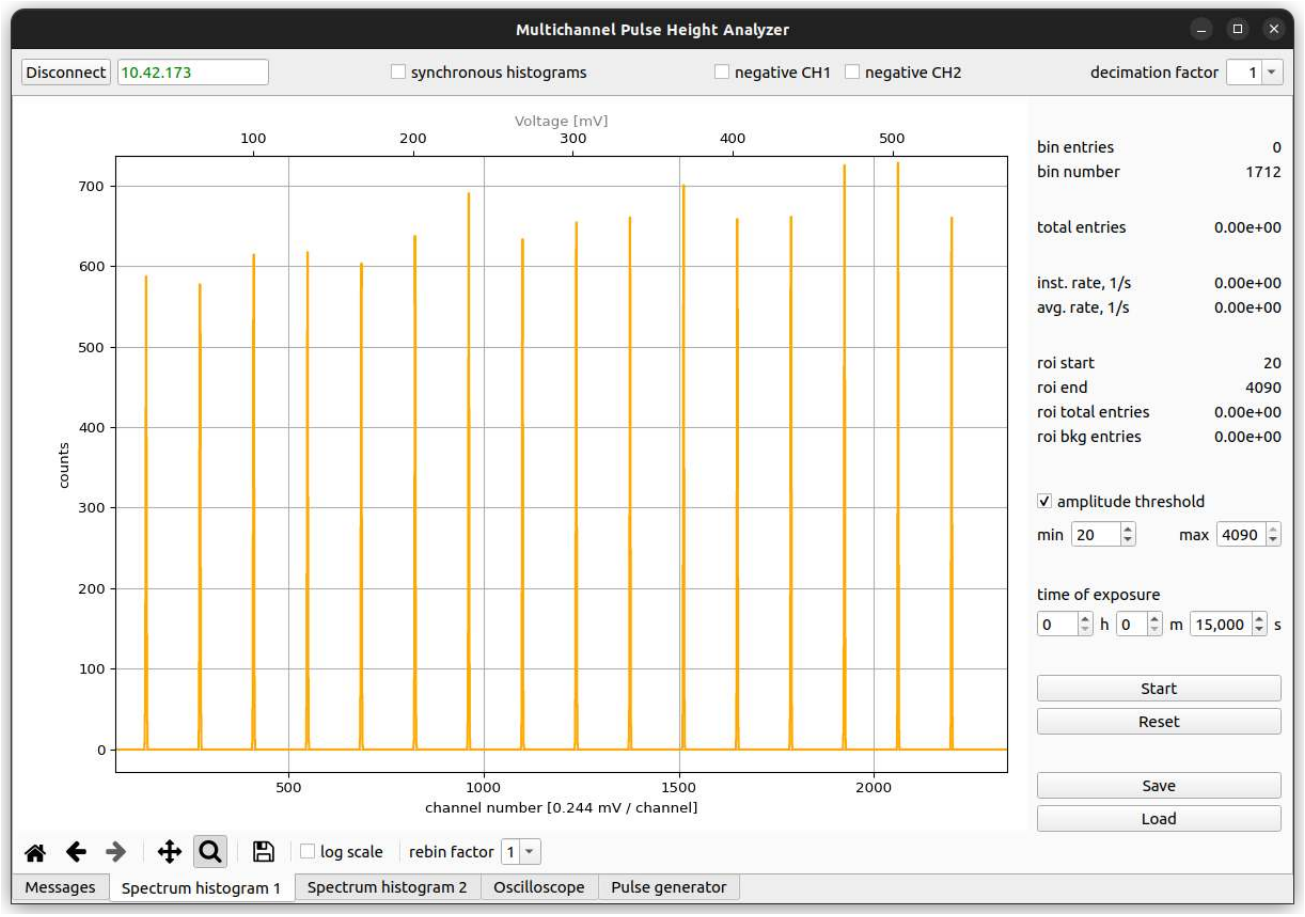

Figure 2.6: Example of a recorded spectrum of pulses from the signal generator

This evaluation is limited to the decimation factor 1, as short pulses are considered in some cases. In addition, the recorded measurement series were carried out with the uniform distribution, as pile-up always occurs in the case of the poisson distribution, as the pulse rate only represents the expectation value there.
For this purpose, for certain pulse rates [1,3,5,10,20,30,50] in kilo samples per second (ksps), the fall time of the pulses is constantly varied [5,8,10,20,40,50,70,80,90,100] μs and the rise time is left constant at 50 ns, as this is always at least one order of magnitude smaller than the fall time. The measurement data is shown in Tables A.3-A.8. The peaks in the spectrum (see Figure 2.6) are analysed using the $kafe2$ module $HistFit$, whereby a normal distribution is assumed as the probability density function (p.d.f.), as this describes the smeared peaks sufficiently accurately; an examplary analysis is shown in Figure 2.13.[5]

[5] No uncertainties are given for the results in this chapter; instead, this chapter is intended to help to understand how the signal generator works and how the pulse height analysis of the MCPHA works.

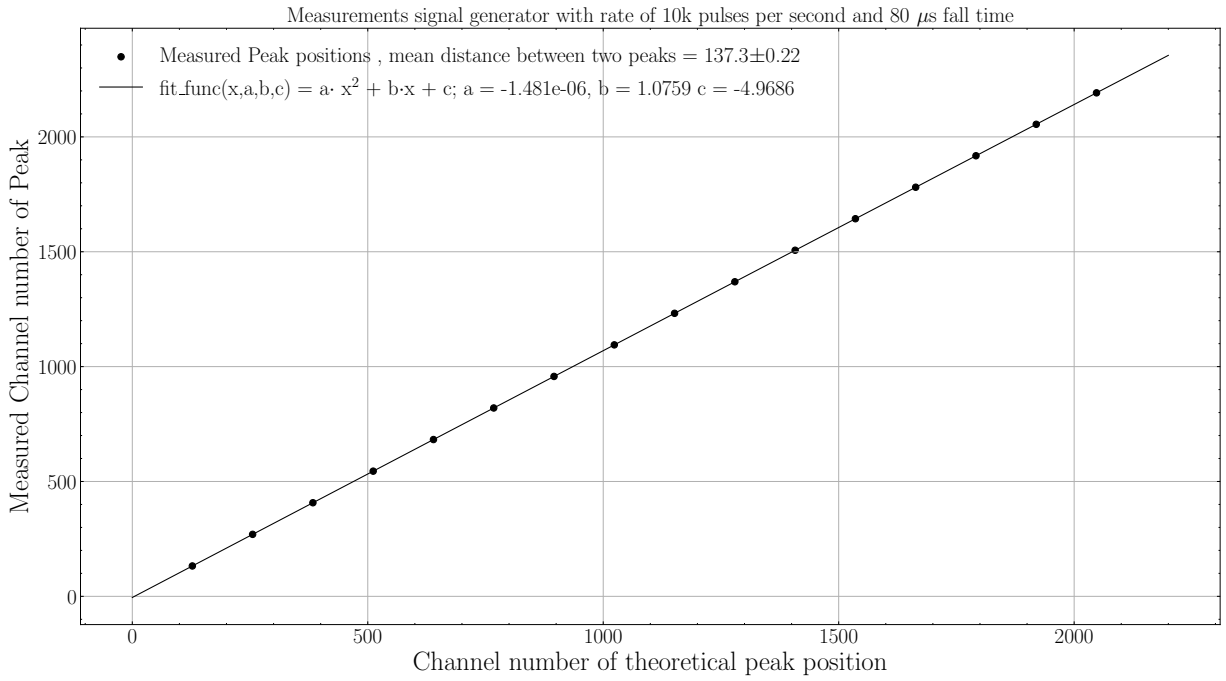

Figure 2.7: Measured channel plotted over the theoretical channel.

In the first step of the evaluation, the measured position of the fitted peaks is plotted against the theoretical position of the peaks. The case of the pulse rate 10 ksps and 80 μs fall time is shown in Figure 2.7 to symbolise the results of this study. In this case, deterministic pulse overlap is clearly recognisable in the oscilloscope. This case is selected because radioactive sources are used in the physics lab experiments, which achieve maximum rates of 10 ksps at a minimum distance from the detector and optimal settings of the operating voltage amplifier. Despite the overlap recognised in the oscilloscope, this approximate linear progression and a non-linearity $NL = \frac{a \cdot x}{b}$ of 0.003 in 2200 channels shows that the Red Pitaya shifts the peaks, but in good approximation linearly and does not change the mean peak distance of 137.3 channel significantly, as the mean distance shows a standard deviation of ± 0.22.[6]

[6] With increasing channel number of the peaks, the shape of the peaks in the spectrum deviates more and more from a Gaussian, since a higher channel number is associated with a bigger voltage pulse and these pulses overlap significantly more with other pulses than smaller pulses.

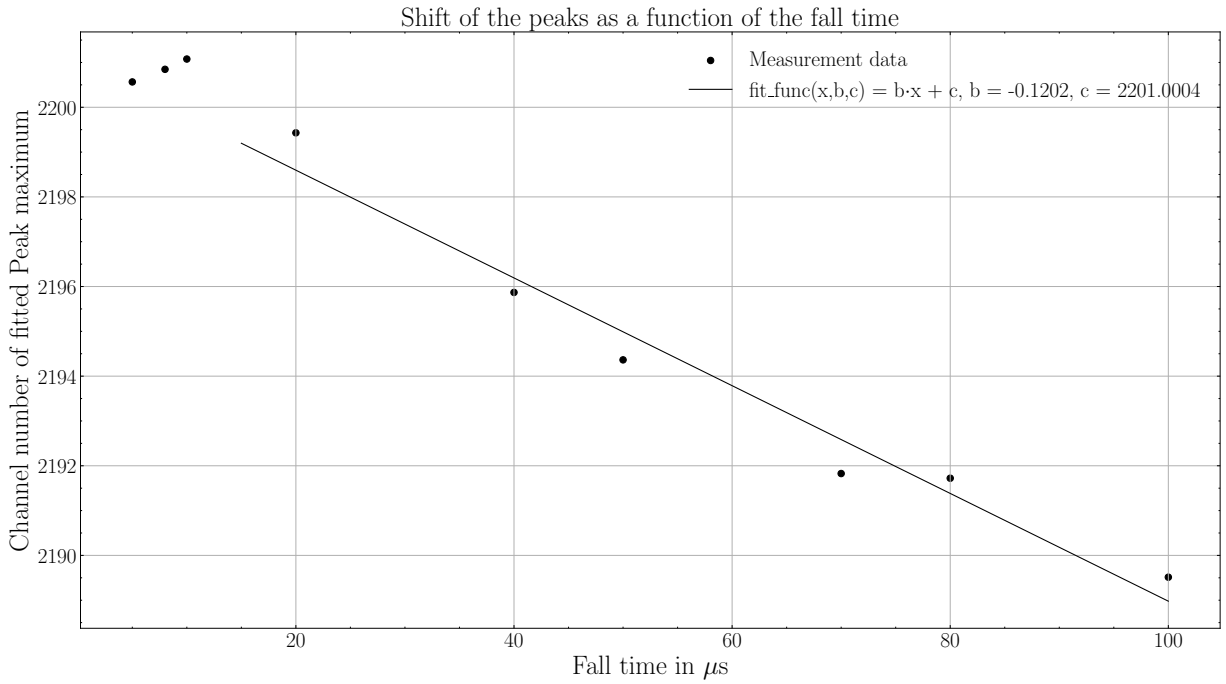

Figure 2.8: Progression of the absolute position of peak 16 with increasing fall time and constant pulse rate = 10 ksps.

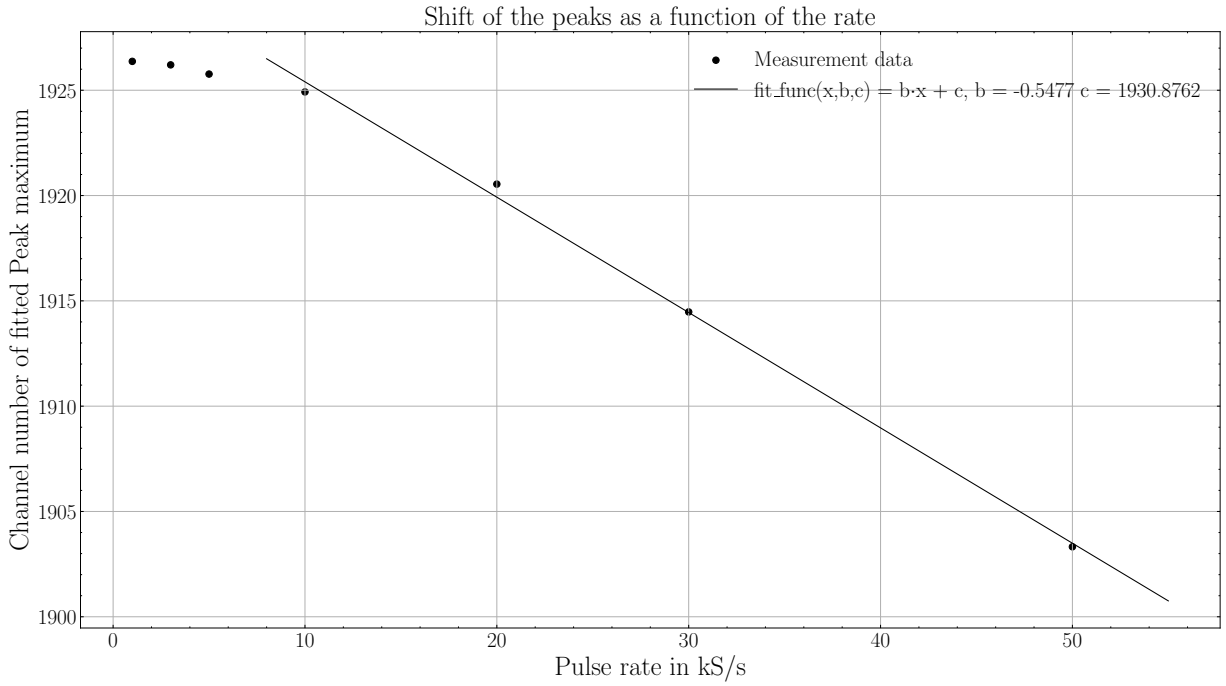

Figure 2.9: Progression of the absolute position of peak 14 with increasing pulse rate and constant fall time = 20 μs.

In the second part of the evaluation, the peak position and the corresponding fall time are plotted against each other for a constant pulse rate. Vice versa, the peak position is also plotted against the increasing pulse rates for a constant fall time. Figures 2.8 & 2.9 can be considered as an example of the measurement results. This reflects what is determined by several series of measurements. For $\kappa < 0.10$ there is approximately no shift in the peak maxima position μ

for varying pulse rates and fall times. This is shown in Figures 2.8 & 2.9 by the fact that the first three measurement points are approximately the same size and deviate from the regression line[7] of the remaining data points. It should be noted here that for multiple recordings of the measurement series, the data points located in this area are those that fluctuate strongly around a horizontal line, in contrast to those data points with $\kappa > 0.10$. For these measured data points, it should be noted that overlap can be visibly recognised in the oscilloscope, as can be seen from the red markings in Tables A.3-A.8. In general, it was found that the progression of the shifts is approximately linear up to $\kappa \approx 1$. For $\kappa > 1$, the shape of the smeared peaks

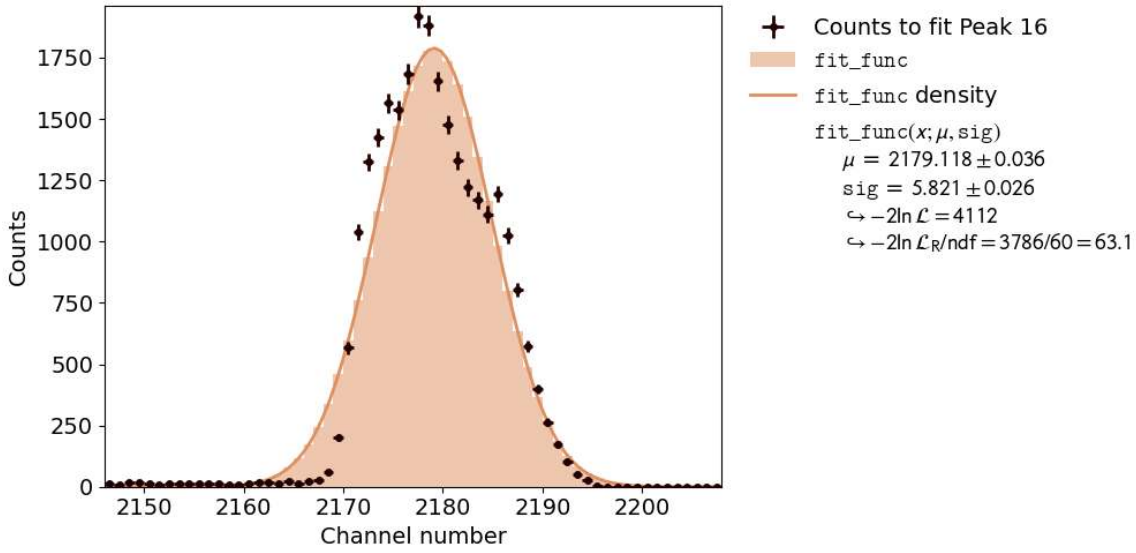

Figure 2.10: Deviation of the peak from a normal distribution for $\kappa > 1$, shown at Peak 16 for 30 ksps pulse rate and 40 μs fall time.

deviates too much from a gaussian curve and background begins to appear under the peaks, as shown in Figure 2.10. The result is misshapen widening, splitting of the peaks and skewing. This is triggered by increased overlap, as the pulses now add up in such a way that they can no longer be fully detected in LV-mode, as their addition exceeds the detection limit of 1 V.

[7] In the course of the evaluation, several models were adapted to the measurement data, including exponential, logarithmic or nth-order Polynomials. It turns out that the measurement data is best reflected by straight lines.

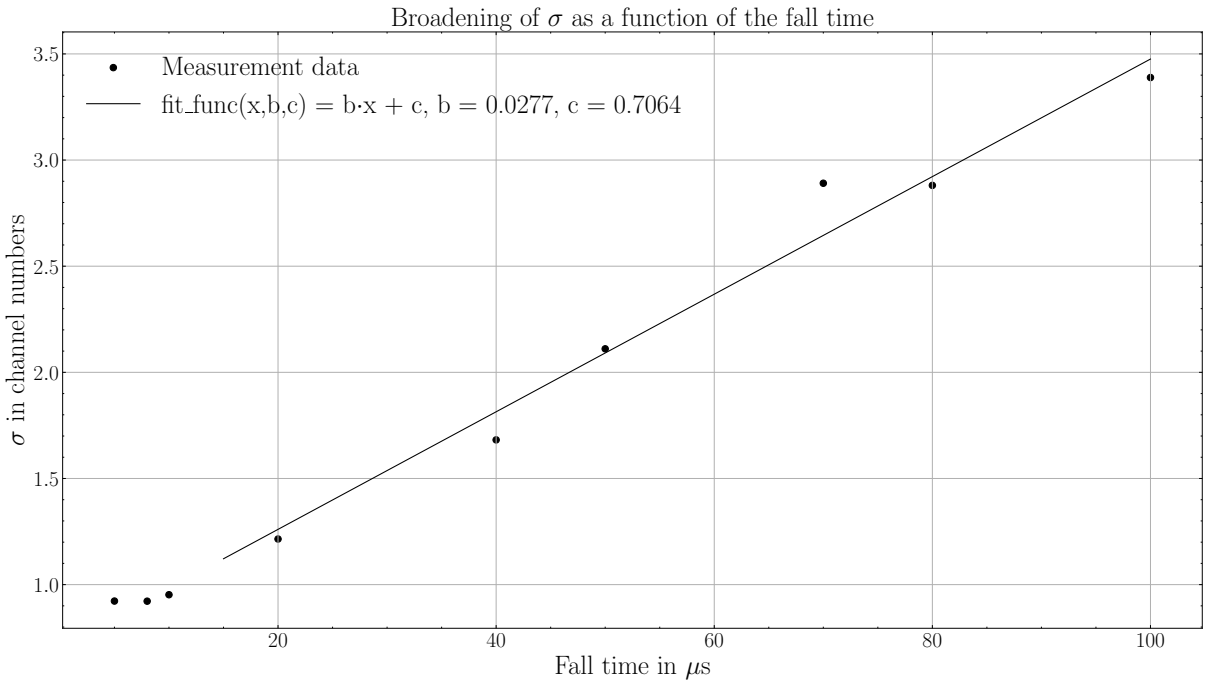

Figure 2.11: Progression of σ of peak 16 with increasing fall time and constant pulse rate = 10 ksps

If the change in the width of the peaks, represented by σ, for constant pulse rate and increasing fall time is plotted against each other, this results in a linear rise with increasing fall time (analogue to the measurement of the fitted peak positions). This relationship is shown as an example in the Figure 2.11 and also explains the fact that the peaks lose height and become wider with increasing fall time at the same pulse rate. For κ<0.10 the values of σ also fluctuate around a horizontal line within repeated measurements.
For pulse rates up to 10 ksps, measurement series were also recorded with the poisson distribution. Due to the permanent occurrence of pile-up, the peaks now have a significantly stronger background towards the left flank of the peak. These peaks can still be analysed and in most cases can be well approximated by fitting only the right flank and the upper peak area of the left flank. This results in only small and often negligible shifts in the absolute peak positions compared to the uniform distribution, as can be seen in Figures 2.13 & 2.14.

In the last part of the analysis of the Signal generator, the fall time is analysed. Due to a lack of documentation on how this is defined in the MCPHA, an attempt is made to reconstruct this based on the measurement results. In the assumed model, the voltage pulse after reaching the maximum is described by a decreasing exponential function.

$$\mathrm{V(t)} = \mathrm{V_0} \cdot \exp\left(-\frac{\mathrm{t} - \mathrm{t_{V_0}}}{\tau}\right) - \mathrm{Offset} \tag{2.8}$$

According to this ansatz, the fall time is defined by the time difference t_f for which the following applies

$$\mathrm{t}_f = \mathrm{t}_2 - \mathrm{t}_1 = \tau \cdot (\ln(x) - \ln(y)) \tag{2.9}$$

whereby x and y are defined by

$$\frac{V(t_1)}{V_0} = x \tag{2.10}$$

$$\frac{V(t_2)}{V_0} = y. \tag{2.11}$$

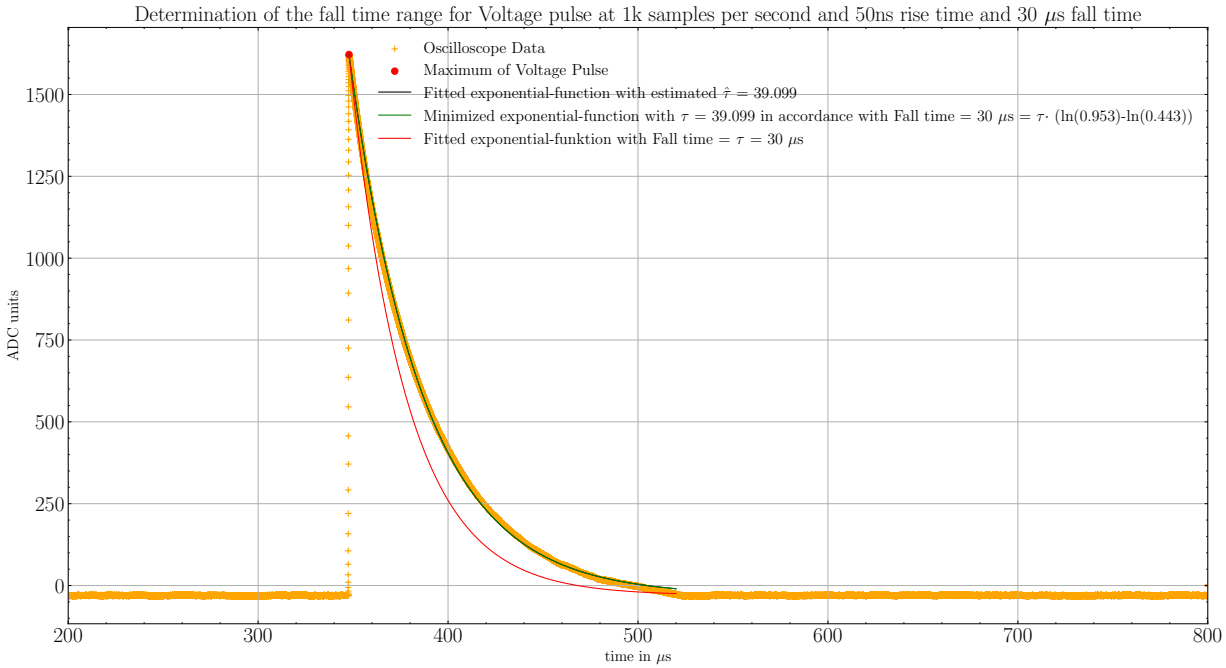

Figure 2.12: Reconstruction of the fall time with a voltage pulse of 30 μs fall time

Performing an exponential fit to the measured voltage pulse, the estimated $\hat{\tau}$ is determined. Furthermore, the parameters x and y are optimised using eq. 2.9 so that the deviation is as little as possible from the estimated $\hat{\tau}$.[8] An example graph can be seen in figure 2.12. Analyses of various pulses result in the following average

$$x = 0.926 \pm 0.016 \tag{2.12}$$

$$y = 0.423 \pm 0.018. \tag{2.13}$$

If these bounds are indeed chosen in this way, they represent an unusual choice of parameterisation, as $x \in [0.9, 0.8]$ and $y \in [0.2, 0.1]$ are chosen as standards for such systems. The choice of $\tau =$ fall time was also considered, but this generally deviates strongly from the measured data, as shown in Figure 2.12. It can nevertheless be assumed that the case $\tau =$ fall time is used and the strong deviations arise based on inaccuracies in the electronic implementation.

In conclusion, at the time of publication of this study, the system consisting of Red Pitaya STEMlab 125-14 and MCPHA is not suitable for measuring absolute voltage values. Since this appears to be a software problem, it could be solved by adjusting the source code. Nevertheless, the analysis presented in this chapter provides a basis for testing the Red Pitaya and the MCPHA for their usability in recording γ-spectra, since the analog-to-digital conversion appears to be linear.

[8] The maximum deviation limit was set to $\epsilon < 0.0001$.

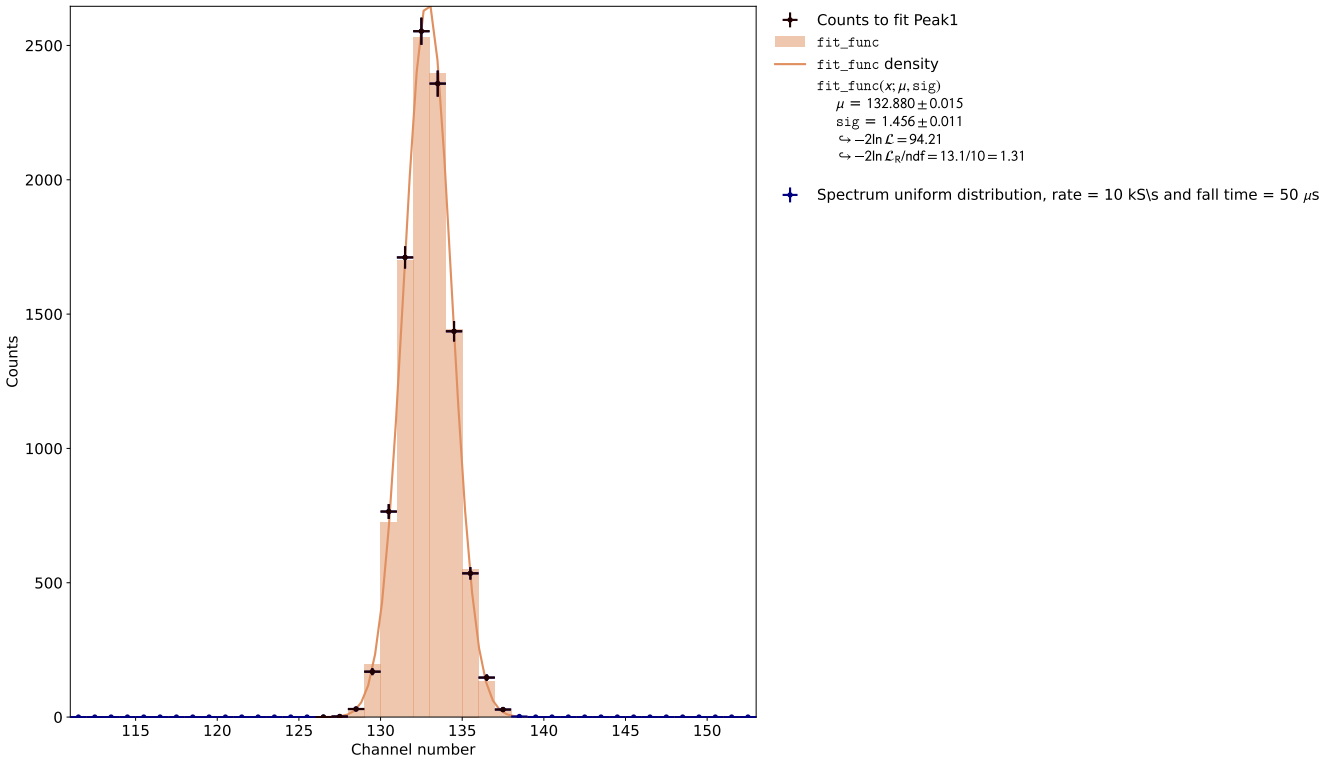

Figure 2.13: Fit of peak 1 for uniform distribution and 10 ksps pulse rate and 50 μs fall time

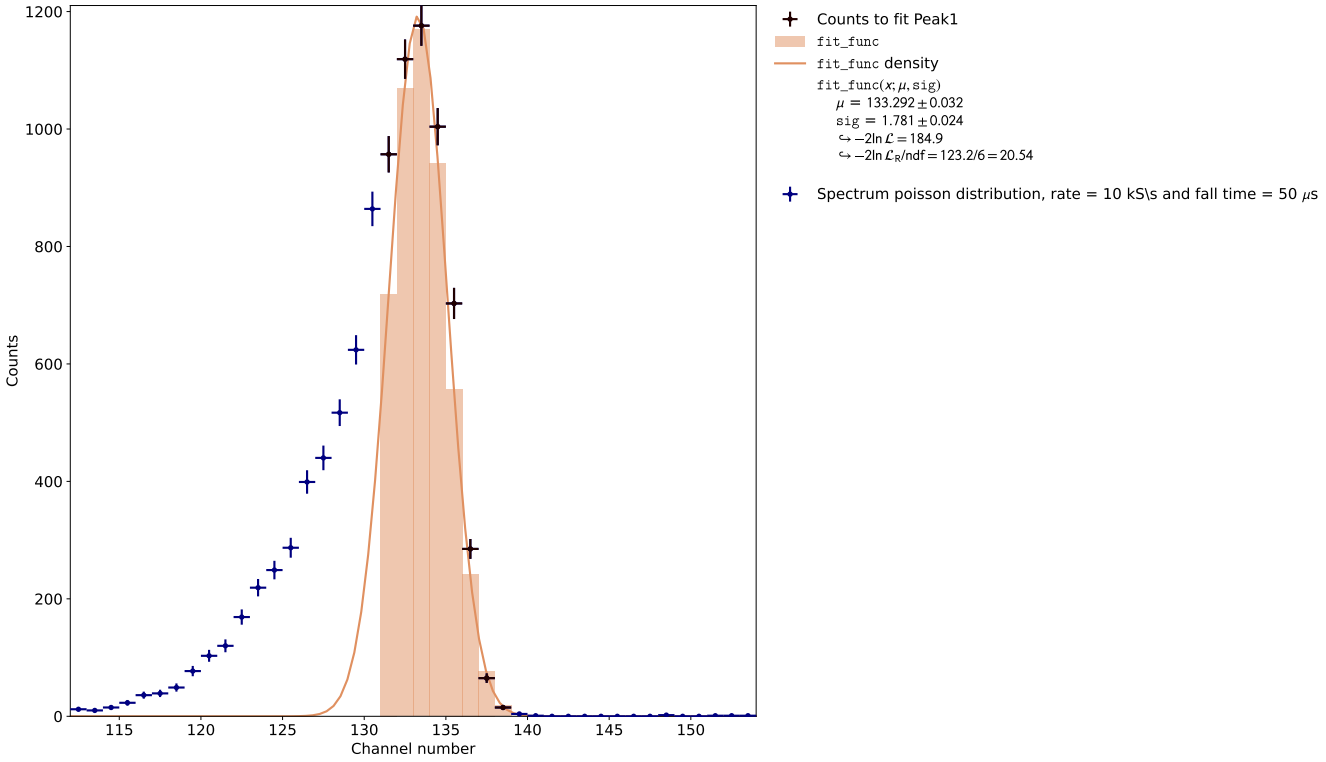

Figure 2.14: Fit of peak 1 for poisson distribution and 10 ksps pulse rate and 50 μs fall time

CHAPTER 3

THEORY BEHIND THE ANALYSIS OF RADIOACTIVE SPECTRA

This Chapter briefly describes the most important physical concepts for understanding the analysis of radioactive γ-spectra. For a deeper understanding of these concepts, please refer to the mentioned literature.

3.1 Physics behind Radioactive Decay

With a view to the decay of unstable or excited nuclei, the three most important decay types of α-, β- and γ-decay must be described. Radioactive decay is the transformation of an unstable or excited atomic nucleus into another atomic nucleus or nuclear state by emitting ionising radiation; these unstable nuclei are called radionuclides. Within the context of the "liquid-drop model" of nuclear physics, the total binding energy of a nucleus can be determined approximately using the simplified Bethe-Weizsäcker formula (cf. [Dem17]; Chapter 2.6.3, pp.28-30)

$$E_{\mathrm{B}} = a_{\mathrm{V}} \cdot A - a_{\mathrm{S}} \cdot A^{\frac{2}{3}} - a_{\mathrm{C}} \cdot Z^2 \cdot A^{-\frac{1}{3}} - a_{\mathrm{A}} \cdot \frac{(N-Z)^2}{A} + \frac{\delta}{A^{\frac{1}{2}}} \tag{3.1}$$

where δ is zero for odd A, δ_0 for even Z and N, -δ_0 for odd Z and N.
Z is the nuclear charge number, A is the mass number and N is the neutron number. The coefficients a_i are determined experimentally and depend on the optimisation range. The values for a possible fit to nuclear data with A $>$ 40 are therefore in MeV [DK23]

$$\text{Volume term} : a_V = 15.58 \tag{3.2}$$
$$\text{Surface term} : a_S = 16.91 \tag{3.3}$$
$$\text{Coulomb term} : a_C = 0.71 \tag{3.4}$$
$$\text{Asymmetry term} : a_V = 23.21 \tag{3.5}$$
$$\text{Pairing term} : \delta_0 = 11.46. \tag{3.6}$$

It should be noted that this formula only describes the binding energy of nuclei approximately and fails in the range of small mass numbers A and for nuclei with the so-called magic numbers. In this respect, the Fermi gas model and the nuclear shell model represent a more precise method for describing atomic nuclei (cf. [Pov14]). Nevertheless, the Bethe-Weizsäcker formula can be used to model the course of the binding energy and thus make a statement about the stability of a nucleus.

The decay of a nucleus takes place through different types of physical processes. Since radioactive decay is not a deterministic process and is generally subject to Poisson statistics, a so-called decay probability λ can be defined for each radionuclide. This is defined as the reciprocal of the mean lifetime τ. In order to model the number of undecayed radionuclides N as a function of time t, the decay law is obtained [DK23]

$$N(t) = N_0 \cdot \exp(-\lambda \cdot t). \tag{3.7}$$

The three most important decay types are briefly explained below, with a focus on the γ-decay. For a better understanding of the processes and a heuristic motivation of equation 3.1, please refer to Povh et al. [Pov14], the "Einführung in das Kern- und Teilchenphysikalische Praktikum" by Joachim Wolf [Wol23] or the corresponding Wikipedia articles, which usually provide good explanations.

α-decay

The α-decay of a radionuclide X to Y is based on the reaction equation

$$ {}^{A}_{Z}\mathrm{X} \rightarrow {}^{A-4}_{Z-2}\mathrm{Y} + {}^{4}_{2}\mathrm{He} + \Delta E \tag{3.8} $$

[Wol23]. The ^{4}He-nucleus represents the so-called α-particle. This type of decay cannot be described in classical physics and is based on the quantum mechanical tunnelling effect. In simplified terms, particles within a nucleus are subject to strong interaction, so the potential within the nucleus resembles a potential barrier with finite depth and width. An α-particle formed in the nucleus is also subject to this potential, but outside the nucleus it only feels the Coulomb potential. For the α-particle with positive energy, it is now possible to pass through the potential barrier. The condition for α-decay, which is a two-body decay, is the greater mass of the parent nucleus compared to the sum of the masses of the daughter nuclides. The energy released due to the mass defect ΔE is distributed to the daughter nuclei as kinetic energy according to the conservation of momentum and energy. It should be noted that all α-instable nuclei have a mass number $\mathrm{A} > 150$.

β-decay

The β-decay can be divided into three different decay processes and is a weak interaction process, due to the decay by emission of a virtual W-boson. If the mass of the mother nucleus is greater than the mass of the daughter nucleus and an electron, β^- decay is possible

$$ {}^{A}_{Z}\mathrm{X} \rightarrow {}^{A}_{Z+1}\mathrm{Y} + \mathrm{e}^- + \overline{\nu}_e \tag{3.9} $$

[DK23]. This occurs in the case of neutron-rich nuclei.
In the event of an excess of protons, the β^+ decay is possible

$$ {}^{A}_{Z}\mathrm{X} \rightarrow {}^{A}_{Z-1}\mathrm{Y} + \mathrm{e}^+ + \nu_e \tag{3.10} $$

[DK23]. Moreover, this decay is only possible if the daughter nucleus and the rest mass of an electron have a lower mass than the parent nucleus. Conversely, in atomic mass units, this means that the parent atom must be heavier than the daughter atom by at least two electron masses, as reducing the atomic number leaves an excess electron. The mass of the electron neutrino ν_e or antineutrino $\overline{\nu}_e$ is neglected in both cases, as it can be given an upper bound with [Col22]

$$ \mathrm{m}(\nu_e) < 0.8\,\mathrm{eV} \tag{3.11} $$

and it is thereby much lighter than the other constituents, e.g. $\mathrm{m(e)} = 511\,\mathrm{keV}$.
Electron capture is based on the non-vanishing probability of an electron being inside of the nucleus. As a result, especially for heavy cores with large core radii, the reaction

$$ {}^{A}_{Z}\mathrm{X} + \mathrm{e}^- \rightarrow {}^{A}_{Z-1}\mathrm{Y} + \nu_e \tag{3.12} $$

[DK23] is possible. As this usually occurs with electrons from the K-shell close to the nucleus, this process is also known as K-capture, which can release characteristic X-rays, as electrons from higher shells successively occupy the energetically more favourable energy levels that are released. Another possibility is the Auger effect, whereby a so-called Auger electron is excited and emitted due to the binding energy released during the process.

γ-decay

Within this study, the focus is on analysing and gaining knowledge from recorded γ-spectra. γ-radiation is produced during the transition from excited nuclear states to the ground state or generally to more energetically favourable energy levels and it thereby represents electromagnetic radiation. This electromagnetic radiation can generally be described as a superposition of various multipole radiation, both electrical and magnetic. It should be noted here that the conservation of angular momentum must be ensured during a transition from one nucleus state to the other. For a transition J_i to J_f, where J describes the total spin of the nucleus, the following inequality must be fulfilled (cf. [Pov14]; Chapter 3.4, pp.36-39)

$$|J_i - J_f| \leq l \leq J_i + J_f, \tag{3.13}$$

where l describes the angular momentum of the emitted photon. The parity P must also be conserved and so a photon of magnetic multipolarity has the parity $(-1)^{l+1}$ and a photon with electric multipolarity has the parity $(-1)^l$. In general, the transition probability decreases with increasing multipolarity and the lifetime of excited states approximately covers a range from 10^{-9}s to 10^{-15}s.
Regarding to γ-radiation, the interaction with matter is particularly important. Here, the photoelectric effect, Compton-scattering and pair production must be described phenomenologically.

Photoelectric effect

The photoelectric effect generally describes the absorption of a photon and ionisation of the atom.

$$\gamma + \text{atom} = \text{atom}^+ + e^- \tag{3.14}$$

In this process, the photon provides all the necessary ionisation energy in accordance with

$$E_\gamma = h \cdot f, \tag{3.15}$$

the electron receives the remaining energy in the form of kinetic energy. The photoelectric effect is associated with several secondary processes, such as the ionised atom returning to its ground state by capturing electrons and emitting characteristic radiation or the Auger effect, whereby a second electron leaves the atomic shell.
The photopeak is important for the following analysis of the spectra. Since a detector usually measures the kinetic energy of electrons, the output signal of a detector should be directly proportional to the energy of the incoming γ-quantum and so it is important that the entire energy of that γ-quantum is converted into kinetic energy of the electrons. This is achieved by several secondary processes, whereby the part of the binding energy required for ionisation, is now also converted. These secondary processes take place in the order of 10^{-8} seconds, which is usually less than the collection time of a detector and is therefore detected as a single signal

(cf. [Wol23]; Chapter 3.2.2.2, pp.36-38)
It should also be noted that, due to the natural line width, the effects of line broadening, secondary atomic processes and the limited energy resolution of detectors, no classic line (δ-peak) is to be expected in the spectra, but rather a peak with a Gaussian curve shape.

Compton-scattering

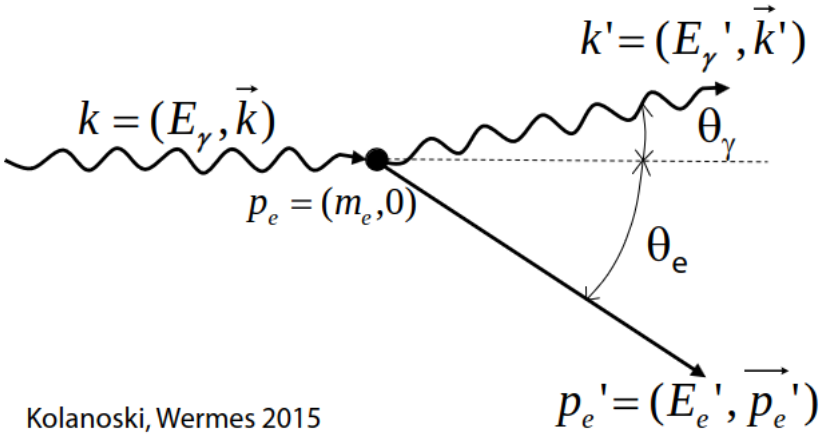

Figure 3.1: Visualised kinematics of the Compton effect (Figure is taken from Chapter 3.5.4 of [KW20])

The Compton effect is the scattering of γ-quants from free and mostly charged particles (see Figure 3.1). The charged particle (in this example an electron) contains a change in energy $E'_{\mathrm{e}}(\theta)$ (as a function of the scattering angle $\theta = \theta_\gamma$) compared to before the collision (electron at rest) of

$$E'_{\mathrm{e}}(\theta) = E_\gamma - E'_\gamma(\theta) = E_\gamma \left(1 - \frac{1}{1 + \frac{E_\gamma}{m_{\mathrm{e}}c^2}(1 - \cos(\theta))}\right). \tag{3.16}$$

The differential cross-section, and thus a measure of the probability of a certain scattering angle, occurring between the two particles, can be determined for unpolarised photons using the Klein-Nishina formula

$$\frac{\mathrm{d}\sigma}{\mathrm{d}\Omega}_{\text{Klein-Nishina}} = \frac{r_e^2}{2[1 + \epsilon(1 - \cos(\theta))]^2} \left(1 + \cos^2(\theta) + \frac{\epsilon^2(1 - \cos(\theta))^2}{1 + \epsilon(1 - \cos(\theta))}\right), \tag{3.17}$$

where $\epsilon = \frac{E_\gamma}{m_e c^2}$ [KW20].
Using Formulas 3.16 & 3.17, it can be seen that the Compton spectrum is continuous in the range of $0 < \theta \leq 180°$. Since the electrons in an atom are not free but bound, these electrons can only be assumed to be quasi-free at photon energies far above the binding energy.

Pair production and Annihilation

Pair production is the physical process in which a photon (in general a boson), with at least the energy of

$$E_\gamma = 2E_0 \cdot \left(1 + \frac{E_0}{M_0 c^2}\right) \tag{3.18}$$

[Wol23], produces a particle- anti-particle pair and vanishes. This does not simply correspond to twice the rest energy E_0 of the particle, as pair production is not possible in a vacuum due to the laws of conservation of energy and momentum, but is only possible in the field of a charged particle (M_0 corresponds to the restmass of this charged particle). The same applies to annihilation, although the conservation laws prohibit the annihilation into a single quantum, but allow the annihilation into two or more quanta.

3.2 Functionality of Radiation Detectors

This Chapter provides a brief introduction to the detector types used in the study. A basic understanding of how radiation detectors work and the physical processes behind them, requires a solid understanding of solid-state physics, such as the band model or the physics of semiconductors and the theory of particle detectors. In the following, the function of the radiation detectors is therefore explained in a descriptive manner and reference is made to the textbooks "Festkörperphysik" by Gross & Marx [GM12], "Particle Detectors" by Kolanoski & Wemers [KW20] , as well as "Einführung in das Kern- und Teilchenphysikalische Praktikum" by Joachim Wolf [Wol23] .

3.2.1 NaI(Ti)- Scintillation Counter

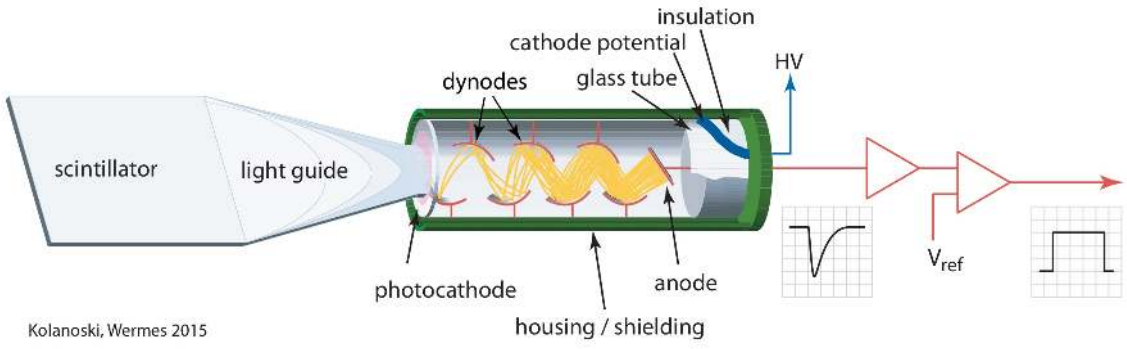

Figure 3.2: Visualised structure of signal processing chain in a scintillation detector (Figure is taken from Chapter 13.1 [KW20])

The used NaI(Ti) scintillation detector, is based on the detection of radiation through the emission of light. Here, the inorganic crystal compound sodium-iodide (NaI) is excited by ionising γ-radiation to emit light.
In general, a scintillation detector therefore consists of a scintillation crystal and a photodetector, a so-called photomultiplier, to transform visible light into electrical signals.
An ideal inorganic crystal can generally be described by the band model, whereby supplying

energy to the crystal can excite transitions from occupied bands (usually the valence band) to unoccupied bands (usually the conduction band). This results in electron-hole pairs, which can recombine with each other and release the excitation energy again, but the energy released in this recombinations is usually associated with a photon wavelength outside the visible range and is thereby irrelevant for the scintillation (cf. [KW20]; Chapter 13.3.1, p. 514).
By doping with thallium(Ti), so-called activator centres are formed, which on the one hand capture quasiparticles, the excitons, produced due to the correlation of electrons and holes, and on the other hand also capture free charge carriers or at which recombination can take place directly. These activator centres are excited by all these processes and can emit photons, in the visible range, when they return to their ground state.
The total energy emitted by the scintillator in the form of light, also known as the Light yield L, should therefore ideally be proportional to the incoming particle energy. In general, the specific Light yield per distance dx is given by Birk's formula

$$\frac{\mathrm{dL}}{\mathrm{dx}} = \frac{S \cdot \frac{\mathrm{dE}}{\mathrm{dx}}}{1 + q \cdot B \cdot \frac{\mathrm{dE}}{\mathrm{dx}}} \tag{3.19}$$

(cf. [KW20]; Chapter 13.2.3), where S is the scintillation efficiency, $\frac{\mathrm{dE}}{\mathrm{dx}}$[1] the energy loss of the particle per path length in the scintillator, B is a material-specific constant and q is the quenching parameter.[2] In the case of γ-radiation, the thickness of the scintillation crystal must be designed so that the interaction processes, described in the previous section, are highly likely to occur and to transfer the energy to the crystal.

A standard set-up of a scintillation detector with a photomultiplier (PMT) is shown in Figure 3.2. This photomultiplier consists of a closed, evacuated glass tube, whereby the incoming light from the scintillator first hits a photocathode and triggers photoelectrons there. These photoelectrons are multiplied via a series of metal electrodes, the dynodes, as secondary electrons can be released there (secondary electron multiplier (SEV)). Thereby the electrons are focussed and directed by electric fields, usually realised by a voltage divider. The electron pulses arriving at the anode can have amplification factors of up to 10^8, where the output pulse should be proportional to the incoming γ-energy at the scintillator and can then be further amplified and shaped. For this further processing, it should be noted that the PMT usually already contains an amplifier that is integrated in the voltage divider.

3.2.2 HPGe- Semiconductor Detector

Another type of detector that is used, which promises a high energy resolution, is the High Purity Germanium detector (HPGe). It is a semiconductor detector and is based on similar physical principles as a diode. For a deeper understanding of how semiconductor detectors work, Chapter 8 in [KW20] and Chapter 10 in [GM12] are highly recommended.

The interaction between the energy states of the bound atoms in the solid crystal lattice causes the energy levels to split up and broaden and so-called energy bands are formed, since the energy levels of certain level groups lie energetically dense. These bands are separated from each other by an energy gap, with the two uppermost occupied bands being described as the

[1] For charged particles, the mean energy loss through matter can be approximated by the "Bethe-Bloch formula"(cf. [KW20]; Chapter 3.2)

[2] Quenching refers to a process in which emission is suppressed and non-radiative transitions are increased and thus q represents the fraction of the non-radiative to the total number (cf. [KW20], Chapter 13.3).

valence band and the conduction band. In the case of semiconductors, all states are almost completely occupied in the valence band and almost unoccupied in the conduction band. Due to the weaker bonding of the neighbouring atoms in semiconductors than in insulators, this uppermost band gap is very small for semiconductors, whereby this gap can be overcome by thermal or electrical excitation and free electrons and holes (defect electrons) are created. The distribution of electrons is thereby described by a Fermi-Dirac distribution[3].
In most cases, however, the conductive properties of semiconductors are changed by doping with impurity atoms. Here, p-doping or n-doping creates space for additional discrete energy states. Acceptor atoms are inserted into the crystal structure by p-doping, which creates an acceptor level above the valence band edge, allowing electrons from the valence band to be bound and free holes in the valence band to be created. Conversely, n-doping with donor atoms provides a donor level below the conduction band edge to donate free electrons to the conduction band.

By connecting a p- and n-doped semiconductor materials, a so-called p-n junction is created, which provides the basis for a detector. This creates a depletion zone, free of charge carriers, triggered by a diffusion current and the accompanying drift current. A curvature of the potential occurs within this zone and a diffusion voltage is generated. The width of this zone depends on the doping and also on what external voltage is applied. Semiconductor detectors are always operated in reverse bias and therefore the positive potential is applied to the n-doped side and the negative potential to the p-doped side, which enlarges the depletion zone. This additional electric field is usually generated by vapour-deposited electrodes on the semiconductor crystal. The γ-radiation entering the depletion zone can now emit its energy there by interacting with the medium and generating electron-hole pairs. These are accelerated towards the electrodes, where they generate an electrical signal that can be measured and whose form depends on the electron-hole pairs generated, their movement towards the electrodes and the shape of the electrodes.

In the case of Germanium, the band gap is 0.66 eV and the average energy for generating electron-hole pairs is 2.96 eV (cf. [KW20]; Chapter 8.2, Table 8.2). This leads to a high energy resolution for Germanium, but also to the indispensability of cooling with liquid nitrogen to minimise thermal transitions.

3.2.3 Energy Resolution

The relative energy resolution of the detector and the subsequent electronics is particularly important for the analysis of the spectra. As the aim of this bachelor thesis is to characterise the Red Pitaya by comparing it to other Multichannel Analyzers, a benchmark must be found for this comparison. The relative energy resolution Φ

$$\Phi = \frac{\sigma_E}{E_\mu} \tag{3.20}$$

can be used for this purpose (cf. [KW20]; Chapter 15.4.3). A better resolution therefore corresponds to a smaller value for Φ. Here σ_E is defined as the σ[4] of the Gaussian peak and E is the associated energy at the maximum μ of the curve. The energy resolution is particularly influenced by statistical processes during transport and the interaction of matter, and thus by

[3] $f(E) = \frac{1}{1+\exp(E-E_F)/k_BT}$, where E_F is the Fermi-energy and k_B is the Boltzmann constant.

[4] It is also common to define the full width at half maximum (FWHM) as σ_E, whereby FWHM $= 2\sqrt{2\ln 2}\sigma$ for a Gaussian peak. In this case, equation 3.20 changes only by the factor $2\sqrt{2\ln 2}$.

electronic and thermal noise.
For scintillation detectors, the energy resolution is primarily determined by the number of scintillation photons generated (cf. [KW20]; Chapter 13.5.2.2). In the case of semiconductor detectors, it is determined by the number of electron-hole pairs (cf. [KW20]; Chapter 15.4.3). A higher number of generated particles is directly linked to a better energy resolution.
Since the energy required to generate charge carrier pairs in the case of HPGe detectors is lower than in scintillation detectors, the energy resolution of HPGe detectors is thereby significantly better (cf. [KW20]; Chapter 13.3).

3.2.4 Signal Processing

3.2.4.1 Signal Form

The theoretical voltage pulse shapes that are registered in the two several detector types differ. Since the Ge-semiconductor counter is a detector with space charge, the voltage pulse results in

$$V(t) = -e\frac{a - bx_0}{b \cdot d \cdot C} \cdot \left(\exp\left(\frac{t}{\tau_h}\right) \cdot \Theta(T^+ - t) - \exp\left(-\frac{t}{\tau_e}\right) \cdot \Theta(T^- - t)\right) \tag{3.21}$$

(cf. [KW20]; Chapter 5.4, eq. 5.86 and Chapter 8.4, eq. 8.82). Here, T^+ and T^- represent the arrival times of the electrons or holes at the electrodes, d the length of the depletion zone, $\tau_{h/e}$ the charactristic charge collection times, a or b constants that describe the applied electric field and x_0 the origin of the charge-carrier pair production. Due to the nature of the space charge zone, this form of a diode can be described as a plate capacitor with a filled dielectric medium, in this case Germanium, which results in the capacitance C. It should be noted that this assumption only applies until the arrival of both charge carriers, i.e. $t < T^-, T^+$. The actual voltage pulse shape of the utilized HPGe-detector, amplified and shaped by the Linear amplifier connected to the detector and digitized with the Red Pitaya STEMlab 125-14, can be seen in Figure 5.4.

In the case of a scintillation detector, the voltage pulse shape is characterised by

$$V(t) = \frac{Q_0}{C} \cdot \frac{\tau_{RC}}{\tau_{RC} - \tau_{dec}} \cdot \left(\exp\left(-\frac{t}{\tau_{RC}}\right) - \exp\left(-\frac{t}{\tau_{dec}}\right)\right) \tag{3.22}$$

(cf. [KW20], Chapter 13.2.4), τ_{dec} represents the average lifetime of the excited emission centres (activator centres) and is therefore a material-specific constant. Q_0 represents the entire charge, integrated in the preamplifier. Since a typical readout chain usually consists of a load resistor R and a capacitor C connected in parallel, this also has an influence on the readout signal, which is where the further time constant τ_{RC} of this chain comes from. As it is usually a common method to represent pulse shapes of scintillators by sums of exponential functions, equation 3.22 ist thereby a reasonable approximation for inorganic crystal scintillators, whereas for Na(Ti) a τ_{dec} of 245 ns can be assumed (cf. [KW20]; Chapter 13.3.2, table 13.3). The actual voltage pulse shape of the utilized Na(Ti)-detector, digitized with the Red Pitaya STEMlab 125-14, can be seen in Figure 4.5.

3.2.4.2 Signal Processing and Digitisation

An overview with helpful explanations regarding signal processing and digitisation is given in [KW20] Chapter 17&18. For this reason, the following is only a brief description of the process

steps that the signal passes through from the detector to digital analysis with the computer.
The signal coming from the detector must first be further processed for digitisation and evaluation. The analog detector pulse is usually a current or voltage pulse, which usually has to be amplified or shaped. If the detector pulses are current pulses, they are usually converted into voltage pulses in order to improve the signal-to-noise ratio or to reduce pile-up, which is usually done using a resistor R and a capacitor C.
In the subsequent amplifiers, the pulses are usually shaped by a sequence of RC-Differentiation or RC-Integration, whereby these function in a simplified manner like high-pass or low-pass filters.
In a subsequent analog-to-digital converter (ADC), these analog continuous pulses are converted into discrete numerical sequences. These discrete numerical values correspond to a certain range in which the part of the voltage signal readout is categorised. By specifying the bits and the voltage range of an ADC, its resolution is defined. These recorded numbers can now be saved on a computer. In the case of the Red Pitaya, voltages in the range of $[-1\text{V}, 1\text{V}]$ can be digitized in Low Voltage Mode with the help of a 14-bit ADC and thus be broken down into 2^{14} equidistant ranges. Such ADCs can often be integrated into Multichannel Analyzers. In the case of the system consisting of the Red Pitaya STEMlab 125-14 and the MCPHA, the pulse height analysis is not performed directly by the ADC, but the integrated FPGA is used to analyze the digitized pulses and to histogram it.
The recorded data can now be stored on a computer and be further processed.

3.3 Methods to Analyze the Recorded Spectra

3.3.1 Recorded Spectra

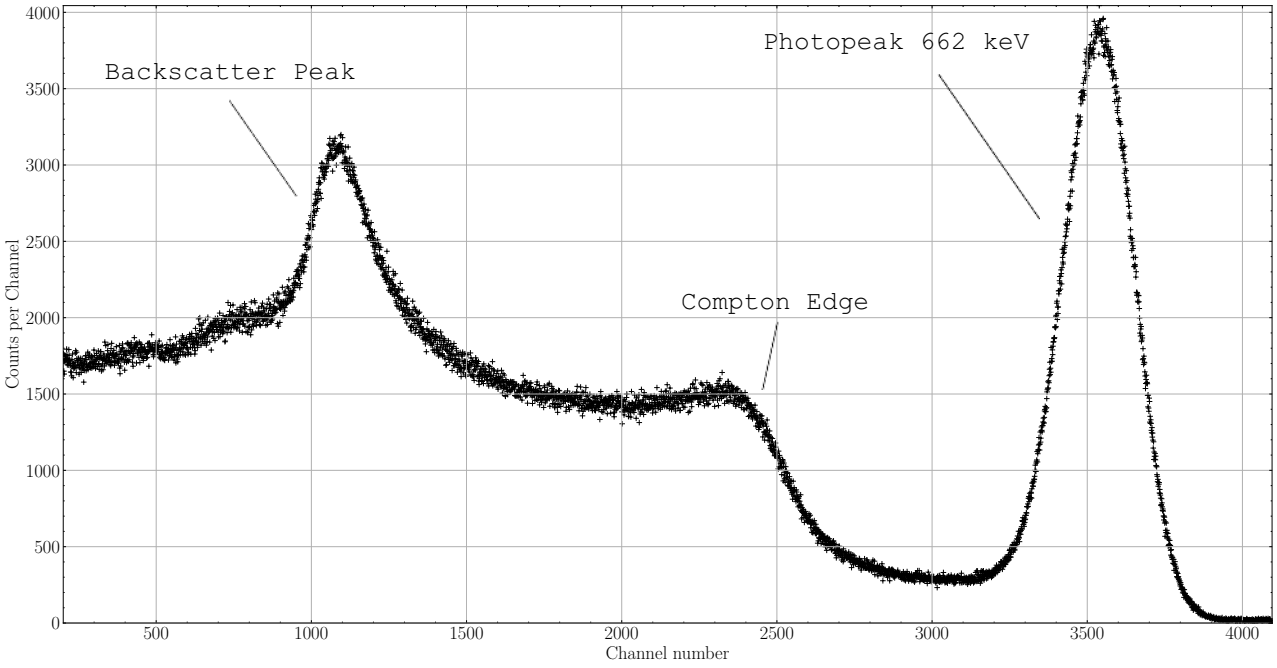

Figure 3.3: γ-spectrum of Cs137 with the NaI(Ti)detector and characteristics

An example of a typical recorded γ-spectrum is shown in Figure 3.3 in the form of a Cs137-spectrum. Here, the counts counted per channel are plotted over the channel number. The

recorded spectrum can be divided into several sections.
Firstly, the significant photopeak can be recognised, it is associated to events where the photon entering the detector releases its entire energy to the crystal through the photoelectric effect. The second recognisable peak is the backscatter peak, i.e. the peak that is created when incident photons are not scattered with electrons inside the crystal but outside by the Compton-effect, re-enter the crystal and completely release their energy there.
The Compton continuum and the Compton edge can also be recognised, which, as explained in Section 3.1, is created by the scattering of the photon on the electrons of the crystal and thus represents a continuous spectrum. However, only the photopeaks are examined for the analyses in this paper. In principle, the Compton edge and its position are also suitable for determining the photon energy using the equation 3.16, but this is not done due to the inaccuracies caused by the smearing of the edge, which is triggered by the finite energy resolution, statistical effects and atomic secondary processes.

3.3.2 Mathematical Foundations

The photopeaks are analysed by parameter estimation using the Binned Likelihood method. The most important mathematical principles are briefly explained in the following section. For a deeper understanding, it is highly recommended to read Chapters 6 & 7 of the textbook "Statistical Data Analysis" published by Glen Cowan [Cow98] and the mathematical foundations in the documentation of $kafe2$ [kafe2].

3.3.2.1 Maximum Likelihood

The Maximum Likelihood method is a method of parameter estimation $\theta = \theta_j, ..., \theta_m$ for given measurement data $x_i, ..., x_k$ and a hypothesis for their probability density function (p.d.f.) $f(x; \theta)$. Assuming the independence of the parameters, the likelihood function $\mathcal{L}$ results in

$$\mathcal{L}(\theta) = \prod_{i}^{k} f(x_i, \theta) \tag{3.23}$$

The estimated parameters $\hat{\theta}$ result from the maximisation of $\mathcal{L}$ according to

$$\frac{\partial \mathcal{L}}{\partial \theta_a} = 0, \text{ for a = j,....,m} \tag{3.24}$$

[Cow98].

3.3.3 Negative Log-Likelihood NLL

For reasons of numerical efficiency, the maximum likelihood method is not usually used to determine the estimated parameters. As it is usually not possible to determine the maximum analytically when there are several estimated parameters θ, a transformation

$$\mathcal{L} \rightarrow -2 \log(\mathcal{L}) \tag{3.25}$$

is performed. This is permitted because the logarithm is a strictly monotonically increasing function. This results in the function to be minimised

$$NLL(\theta) = -2 \sum_{i=1}^{k} \log(f(x_i, \theta)). \tag{3.26}$$

This creates efficiency advantages for the calculation by computers, as sums instead of products have to be minimised and not maximised, since most algorithms minimize functions.

Assuming normally distributed data $x_i, ..., x_k$, centered about their means $\mu_i, ..., \mu_k$ and dropping additive terms not depending on the parameters θ, the NLL results in

$$NLL(\theta) = \sum_i^k \Big(\frac{y_i - \lambda_i(\theta)}{\sigma_i} \Big)^2 = \chi^2(\theta), \tag{3.27}$$

where $\lambda_i(\theta)$ represents the values of the model function for data point x_i, whereby $\mu_i = \lambda_i$ can be assumed and σ_i are the uncertainties to our data point x_i (cf. [Cow98]; Chapter 7.1) This is also called the method of least squares, as the sum of the residual squares is minimised.

3.3.4 Binned Likelihood Fit

When analysing γ-spectra, it should be noted that the measured entries $n_i, ..., n_k$ per bin are Poisson distributed due to the underlying radioactive decay. The likelihood in this case therefore results in

$$\mathcal{L} = \prod_{i=1}^{k} \frac{\nu_i^{n_i}}{n_i!} \cdot \exp(-\nu_i) \tag{3.28}$$

[Cow98], where ν_i represents the expected entries in the bin. As these are binned data, their expected values are characterised by

$$\nu_i(\theta) = \nu_{\text{tot}} \cdot \int_{\text{bin}_i}^{\text{bin}_i+1} h(x_i, \theta), \tag{3.29}$$

where $\nu_{\text{tot}} = \sum_{i=1}^{k} \nu_i$. If there is no functional relation between ν_{tot} and θ, we assume $\hat{\nu}_{\text{tot}} = \sum_{i=1}^{k} n_i = n_{\text{tot}}$. In the fit function shown later, however, n_{tot} is also optimised as a fit parameter, as it is also subject to Poisson statistics. The function $h(x_i, \theta)$ represents the p.d.f.-fit function to be optimised, depending on the fit parameters θ. The NLL to be minimised thus results in

$$NLL(\theta) = 2 \sum_{i=1}^{k} -n_i \cdot \log(\nu_i(\theta)) + \nu_i(\theta). \tag{3.30}$$

[kafe2].

3.3.5 Error Estimation

Since the optimised parameters are estimates, it is essential to specify their uncertainty. For normally distributed estimators $\hat{\theta}_i, ..., \hat{\theta}_j$, the variance V_{ij} can be determined, using the Rao-Cramer-Frechet (RCF) inequality in the large sample limit

$$V_{ij} = -\frac{2}{\frac{\partial^2 NLL}{\partial\theta_i \partial\theta_j}}\Big|_{\theta=\hat{\theta}} \tag{3.31}$$

[kafe2]. This leads to

$$\sigma_{\theta_i} = \sqrt{V_{ii}}. \tag{3.32}$$

For this case of a normally distributed estimator, the limits of the so-called "1σ-confidence interval" are symmetrical around $\hat{\theta}$.

For the case of non-normally distributed estimators $\hat{\theta}_i, ..., \hat{\theta}_j$ a different method, the profile likelihood, must be used. A graphical method is used to determine the 1σ interval limits. For this purpose

$$\Delta NLL(\theta_i; (\theta_{\text{rest}})) = NLL(\theta_i; (\theta_{\text{rest}})) - NLL(\hat{\theta}_i, (\theta_{\text{rest}})) \tag{3.33}$$

is minimised (cf. [kafe2]). The notation is to be understood in such a way that the parameter θ_i is fixed for several values around the region of $\hat{\theta}_i$ and the remaining parameters θ_{rest} are optimised. The parameters θ_{rest} are called nuisance parameters and the method is called profiling. For this method it can be shown that

$$\Delta NLL(\hat{\theta}_i \pm N \cdot \sigma_{\theta_i}, (\theta_{\text{rest}})) = N^2 \tag{3.34}$$

whereby the limits of the 1σ interval can be read from the profile likelihood (N=1). For a normally distributed estimator, this is equivalent to those symmetrical limits determined according to the Equations 3.31 & 3.32 (cf. [Cow98]; Chapter 9.6).

3.3.6 Goodness of Fit

To evaluate how well the model and the data match, a test metric must be introduced. The method of goodness of fit per degree of freedom (GoF/NDF) implemented in $kafe2$ is used for this purpose. This states that if a χ^2-cost function [5] is assumed, the ratio

$$GoF/NDF = \frac{\chi^2}{NDF} \tag{3.35}$$

represents a metric, here χ^2 is the sum of the squared residuals and NDF is the number of degrees of freedom(cf. [Cow98]; Chapter 7.5).
If the NLL is used instead of the least square method, the metric results in

$$GoF/NDF = \frac{NLL(\hat{\theta}) - NLL_{\text{sat}}(\theta)}{NDF}. \tag{3.36}$$

Here $NLL_{\text{sat}}(\theta)$ represents the so-called saturated NLL(cf. [Cow98]; Chapter 6.11). This represents the minimum that the NLL can have and therefore, in the case of equation 3.28, the situation where $\nu_i = n_i$.
In the case of the correct assumption of the model and the uncertainties of the data, the expression 3.35 & 3.36 should be approximately equal to 1 for both cases.

3.3.7 Parameter Estimation in kafe2

3.3.7.1 Fit Function

The -Python programming language is used to analyse the spectra. The additional -libraries *numpy*, *scipy*, *matplotlib* and $kafe2$ are mainly used for this purpose. The fit function to be

[5] In our case, a cost function is an optimisation function or metric that shows how well the model matches the data.

optimised is of the following form

$$f(x, N, a, \mu, \sigma, \mathrm{c}_\mu, s, r, l) = \tag{3.37}$$

$$N \cdot \left(\mathrm{a} \cdot \frac{1}{\sqrt{2\pi}\sigma} \cdot \exp\left(-\frac{1}{2} \cdot \left(\frac{\mathrm{x} - \mu}{\sigma} \right)^2 \right) + (1 - \mathrm{a}) \cdot \frac{(\mathrm{c}_\mu + (\mathrm{x} - \mu) \cdot \mathrm{s})}{(\mathrm{c}_\mu - \mu \cdot \mathrm{s}) \cdot (\mathrm{r} - \mathrm{l}) + \frac{1}{2} \cdot (\mathrm{r}^2 - \mathrm{l}^2) \cdot \mathrm{s}} \right). \tag{3.38}$$

The parameters r and l represent the limits of the fit range. They are generally freely selectable, but should limit the complete range of the peak and its immediate surroundings. They are fixed during the fitting procedure.

The parameter N represents the total number of counts in the interval [r,l], N is not fixed but is subject to Poisson statistics and is therefore constraint under the error $\sqrt{N}$. This error results from the Gaussian error propagation under the fact that the number of counts per bin is poisson distributed and the measured value is simultaneously interpreted as the mean value of the measurement (Expectation value). Fitting the parameter N also shows that 3.37 is not a p.d.f., but an actual absolute distribution.

The parameter a represents the proportion of counts in the fit interval that can be attributed to the peak and thus to the signal events that are of interest to us.

The first summand of the fit function thus represents the approximation of the peak by a Gaussian, given by its expectation value μ and its standard deviation / width σ.

As the peak is generally not located on a flat background, the last summand represents the normalized modelling of the background, approximated by a straight line. This straight line is parameterised around the mean value μ of the peak, with a slope s and the height c_μ of the background at the point μ.

This parametrization aims to minimize the correlation of the fit-parameters. The analyses of the photopeaks in the subsequent Chapters have shown that c_μ and s are particularly strongly correlated, especially in the case of a deviation of the shape of the background from a straight line. Likewise, in some cases there is a correlation between the parameters a and σ as well as a and μ. Since a is directly responsible for how many of the total counts in the fit interval are assigned to the peak and thus to the relevant signal, a has a direct influence on the peak's characetristics σ and μ.

3.3.7.2 Fitting Procedure

The basic structure and the most important part of the analysis code is described and explained in this section. A code example is provided in A.1, as the code varies slightly for each spectrum. The Karlsruhe Fit Environment 2 (*kafe2*) is used to determine the parameters, because it directly offers the possibility to perform binned histogram likelihood fits, with the aforementioned mathematical conditions, and so stands out from all other fitting tools in this respect. As the analysis code runs semi-automatically, the starting values for fitting are determined using the tools of the -library *scipy*.

Firstly, suitable starting values of the fit parameters must be found for the convergence of the fit. The *scipy* function

```
scipy.signal.find_peaks()
```

is suitable for estimating the position of the peaks and their characteristics. This provides the option of searching for peaks with certain properties such as height, width or distance to each other and is dependent on these function arguments in this respect. This function returns a list containing the position of the maximum, the width and the prominence of a peak found. The position and the width of the peak, which approximately represents the FWHM, are used directly as starting values for μ or $\sigma \approx \frac{\mathrm{FWHM}}{2.3548}$. A starting value can also be assigned to the fit parameter a from the prominence of the peak and its height by

$$a \approx \frac{\text{Prominence of the Peak}}{\text{Height of the Peak}}. \tag{3.39}$$

For the actual fitting, the class

```
kafe2.fit.histogram.HistFit()
```

is used. The created histogram and the defined fit-function for adjusting the data are passed to this class. The following settings have been selected for the transferred arguments

```
density = False
bin_evaluation = "simpson"
cost_function = "nll_poisson"
```

, since our fit function is not a p.d.f. and the “simpson“-method for numerical integration is performed quickly. To obtain a converging fit result, it is important to assign start values to the fit parameters via

```
HistFit.set_parameter_values()
```

and also limit resp. constrain the parameters by

```
HistFit.limit_parameter()
HistFit.add_parameter_constraint()
```

. In order to obtain correct errors, the following should also be checked when starting the fit

```
HistFit.do_fit(asymmetric_parameter_errors = True)
HistFit.report(asymmetric_parameter_errors = True)
```

, as asymmetrical error bounds can be present in general.
The plotting of the photo peaks and the fitting results is carried out using the

```
matplotlib.pyplot
```

library.

CHAPTER 4

COMPARISON OF RED PITAYA AND THE LEYBOLD CASSY SYSTEM

The main purpose of this study is to evaluate the suitability of the Red Pitaya STEMlab 125-14 and the MCPHA for the acquisition of γ-spectra and the subsequent energy calibration. In the "Beginners physics lab P2", the Leybold Cassy system, consisting of the Leybold Sensor-Cassy, the Leybold VKA-Box and the Leybold Cassy Lab 2, were used to record the γ-spectra in the experiment "Gamma Spectroscopy and Statistics" until the winter semester 2023/2024. This proven but outdated system is used as a benchmark for the performance of the Red Pitaya STEMlab 125-14 in Low Voltage Mode and the MCPHA by Pavel Denim.

4.1 Experimental Set-Up

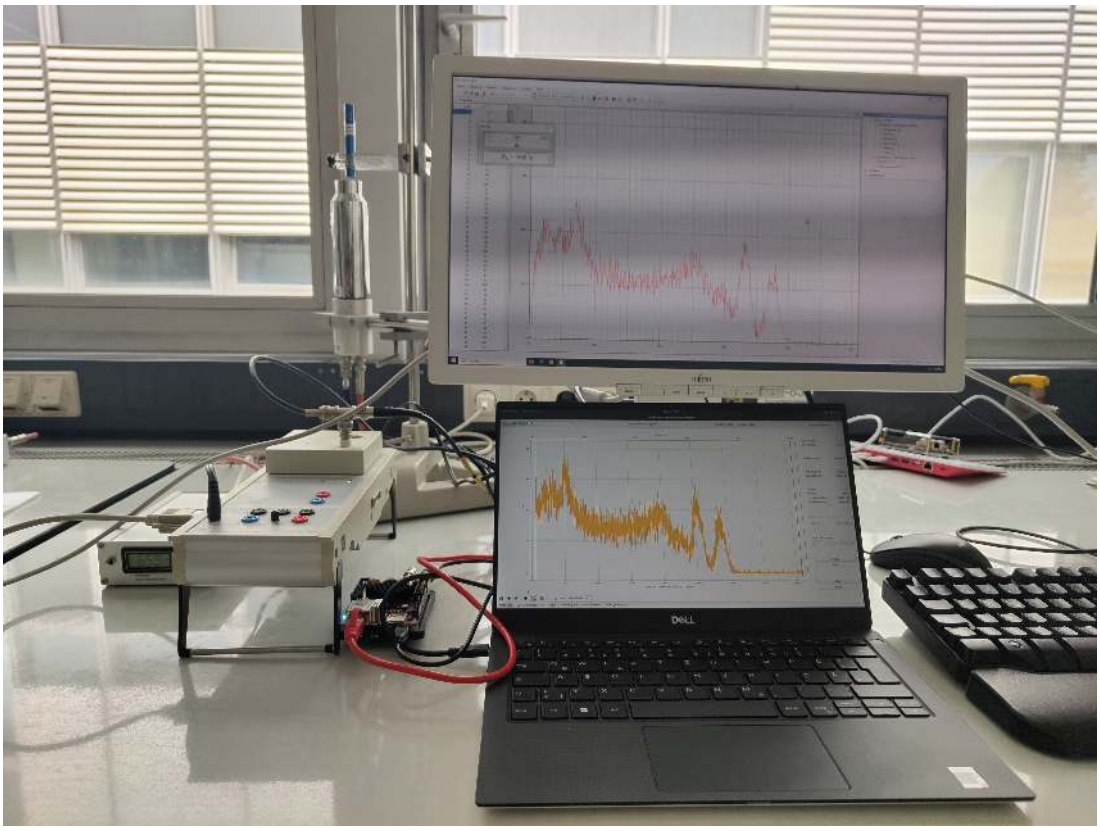

Figure 4.1: Experimental Set-up, consisting of NaI(Ti)-detector, Cassy System and Red Pitaya STEMlab 125-14.

A total of four radioactive sources are used to record the γ-spectra. These consist of Radium-226, Caesium-137, Sodium-22 and Cobalt-60. The experimental set-up used is shown in Figure

4.1. The distance between the mounted radioactive samples above the NaI(Ti)-detector can be adjusted, and thus also the rate of the γ-quanta entering the detector. The detector from Bicron consists of a NaI(Ti)-scintillation crystal (1"×1", diameter × height) from Saint Gobain Crystals and a Photomultiplier with a 14-stage SEV and a 1.5" (diameter)-photocathode, with an integrated preamplifier (c.f [Sim]). The operating voltage of the detector at the photomultiplier can be adjusted using a small wheel at the power supply unit. For optimal utilisation of the dynamic range, this voltage should be in the range of 650-900 V. With the help of a BNC-splitter, simultaneous measurements can be taken with the Red Pitaya and the Cassy system. The data transfer between the Leybold Sensor-Cassy and the computer with CassyLab2 is done via an RS-232 interface, whereby the signals from the detector are received directly by the Red Pitaya via a BNC-cable and an SMA-adaptor to IN1.

4.2 Recording of the γ-Spectra and Energy Calibration

For a comparable energy calibration between the two Multichannel Analyzers, the operating voltage at the photomultiplier must be selected so that the peak with the highest γ-energy is on the right-hand edge of the spectrum and can still be fully recorded. This is the Co60 photopeak at 1332 keV, which results in an operating voltage of 679 V, which means that it can still be fully resolved in the MCPHA spectrum. Since the Cassy system has a larger voltage range, the amplification factor must be set to 5.52 or 906 mV internally in the Cassy Lab 2 in order to also shift the photopeak to the right edge of the spectrum. The distance of the radioactive sources from the detector must also be regulated; on the one hand, the rate for the MCPHA should be in the range of 1-10 ksps in order to reduce pile-up and, for time reasons, not to exceed a maximum measurement time of 10 minutes, the distance for the measurement series can therefore be selected to approximately 1 cm for operational voltages up to 850 V.[1] For the Cassy system, it is also possible to choose between multi-channel measurements and single-channel measurements, but only multi-channel measurements with 1024 channels are used in this study. An example of such a recorded spectrum with the MCPHA is shown in Figure 1.3. For the Red Pitaya, the amplitude threshold must be set so that the channel range 50-4050 is covered, in order to not detect the high number of pulses at the edges of the spectrum, which are either larger than the maximum pulse height of 1V or extremely small and appear as small spikes in the oscilloscope, but are insignificant for the analysis of the spectra.

The photopeaks are analysed using the methods described in chapter 3.3.7. To ensure that the errors were handled correctly, the profiles of the parameters were always considered and it was found that these were clearly symmetrical with minimal deviations to the parabolic approximation of the normal distribution. For this reason, only the errors from the parabolic approximation are included in the following. An example of the evaluation is shown in Figure 4.2, which illustrates why the approximation of the background by a straight line is better than that of a constant background. The analyses of the remaining photo peaks and conversion lines are shown in A.3.1 in the appendix.

[1] For the radioactive sources available, no dependency of the peak position μ on the count rate was recognized in several measurement series.

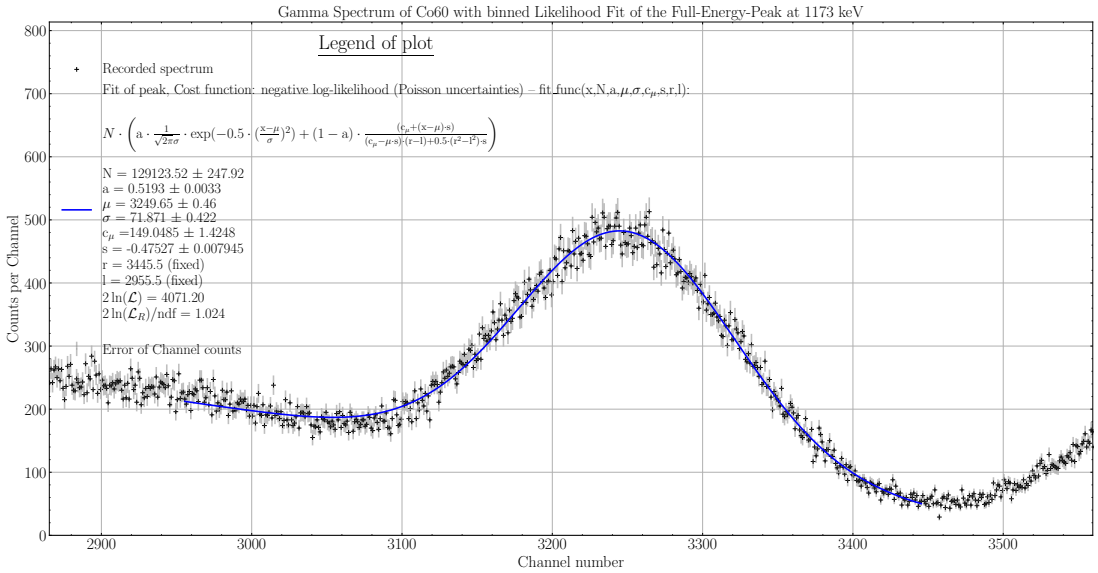

Figure 4.2: Analysis of the Co60 1173 keV photopeak at a detector voltage of 679 V, recorded with the MCPHA by Pavel Denim; $\Phi = 0.0221$.

To perform an energy calibration, the theoretical photpeak energies must now be plotted against the estimated μ of the fitted photpeaks. In the ideal case of a perfectly working detector, which generates voltage pulses exactly proportional to the incident γ-energies and a perfectly working Multichannel Analyzer, there should be a linear relationship between the channel number and energy. In order to estimate the size of a possible non-linearity, a second-degree polynomial is fitted to this curve

$$\mathrm{E}(\mu) = a \cdot \mu^2 + b \cdot \mu + c. \tag{4.1}$$

A measure of the size of the non-linearity is the relative non-linearity Φ, which can be calculated by

$$\Omega = \frac{a \cdot \mu}{b} \approx \frac{a \cdot \mathrm{E}_{\max}}{b^2}, \tag{4.2}$$

with a maximum energy of 1332 keV.

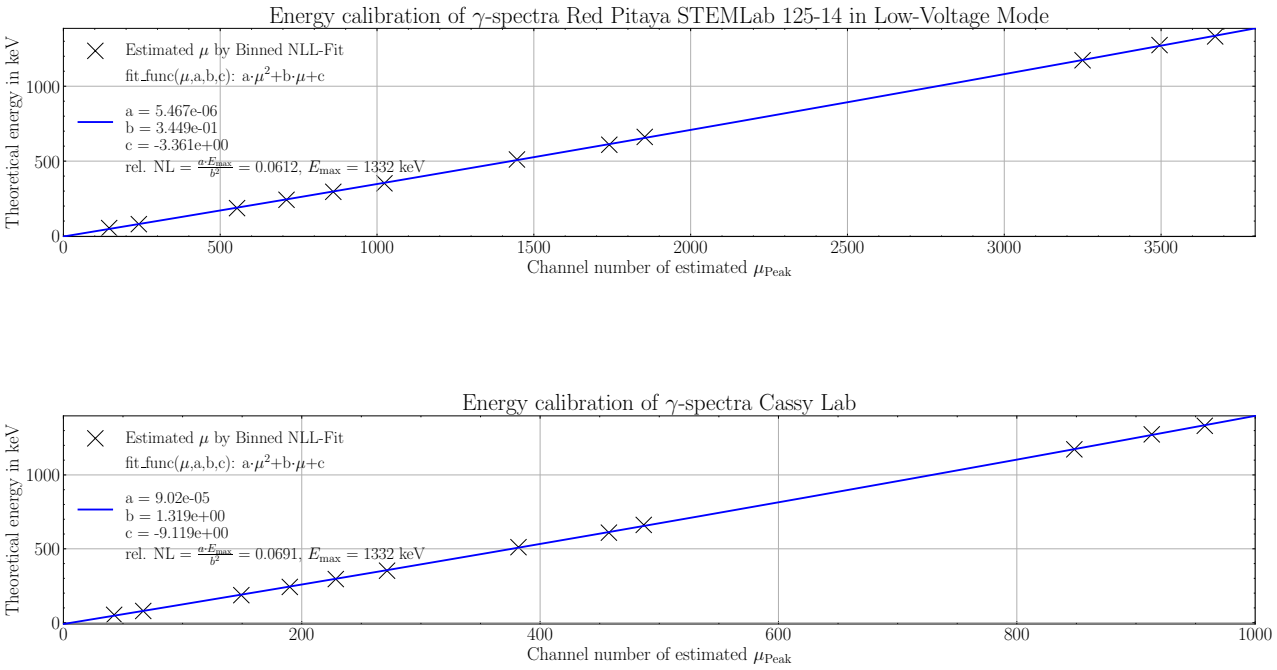

Figure 4.3: Energy calibration of MCPHA and Cassy in a direct comparison without considering data-uncertainties.

In Figure 4.3 uncertainties of the data are not considered to give a preliminary idea of the situation. Since the given inaccuracies for the μ of the analyzed photopeaks in A.3.1 are to be considered only as statistical errors and are extremely small, the systematic errors, which are caused by approximations in the model assumption of an Gaussian with a linear background, inaccuracies in the correct determination of the fit interval and the starting values of the fits as well as the dominant uncertainty of the stability and accuracy of the experimental set-up, are to be assumed to be significantly larger.
Furthermore, the theoretical γ-energies of the photopeaks are known in terms of their values to the second decimal place in keV. The data provided by Eckert & Ziegler "Strahlen- und Medizintechnik AG"[Zie10a]-[Zie10b] and Leybold Didactic [Did] are used for these theoretical values as well as the data from the IAEA [Age]. The IAEA data show that the uncertainties in the theoretical γ-energies are very small and only affect the third decimal place in keV.
If a $XYFit$[2] is now executed with the help of $kafe2$ and only the statistical errors of the μ and the uncertainties of the theoretical γ-energies are considered [3], then χ^2/NDF, according to 3.35, corresponds to a value that differs from 1 by several orders of magnitude, whereby this indicates that the errors are significantly underestimated or the fit model is not appropriate. To establish the Goodness of our fit and to improve the χ^2/NDF, the errors of the μ would have to be scaled to an extent, which the shape of the recorded spectra in any case would not admit.
However, it is extremely important to note that the spectra were recorded at different times. Instabilities in the experimental set-up, such as the setting of the operating voltage of the photomultiplier or temperature fluctuations, as well as instabilities within the dynode-chain, mean that the exact reproducibility of the measurements is not given and can lead to energy

[2] Under A.3.1.1 it is described why the 53.23 keV and 79.3 keV peaks of the Ra226 spectrum were included in the analysis, although they significantly increase the non-linearity.

[3] Since the peak at 79.3 keV represents the superposition of several K_α-conversion lines, its uncertainty is estimated to be 5 keV, as indicated in the literature.

shifts between the measurements of the γ-spectra, even if the measurements are only 20 minutes apart.
This allows the hypothesis of an additional systematic error due to these instabilities in the experimental set-up, whereby this can be taken into account in the fit of the energy calibration by an absolute error on the measured μ and thereby the x-data. As can be seen from the Figure 4.4, a reasonable χ^2/NDF value is obtained by an additional x-error of 12 channels for the Red Pitaya system and 3 channels for the Cassy system. The fact that the MCPHA has exactly four times as many channels as the Cassy system and the additional x-error is exactly four times as large, causing both systems to produce almost the same χ^2/NDF value, indicates that the error has been correctly estimated, since such an error in relation to the 4096 or 1024 channels only represents a shift of about 0.3%.

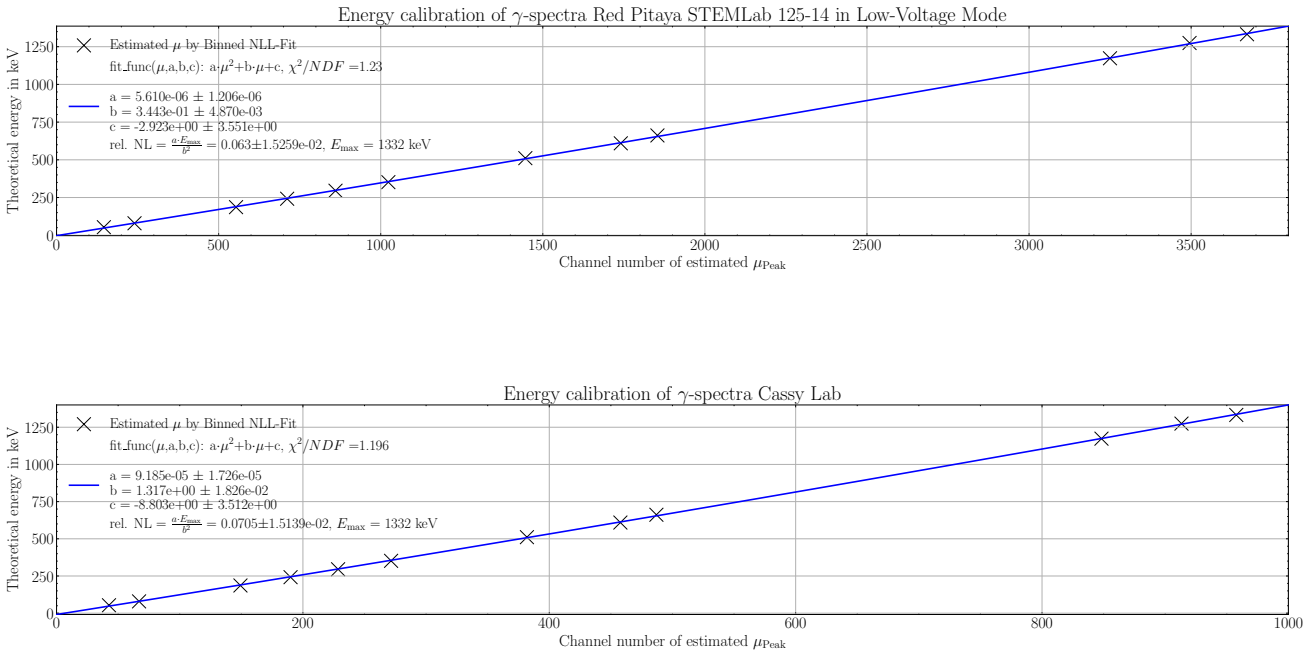

Figure 4.4: Energy calibration of MCPHA and Cassy in a direct comparison with considering data-uncertainties.

For the Red Pitaya STEMlab 125-14 results $\Omega_{\text{MCPHA}} = 0.063 \pm 0.015$ and for the Cassy system $\Omega_{\text{Cassy}} = 0.071 \pm 0.015$ in 1332keV respectively. The confidence intervals of both results therefore overlap, although these errors should be viewed with caution for the reasons given above. Further reasons for the occurrence of this non-linearity may be related to the scintillation crystal, since electrons can leave the detection medium due to statistical effects or due to excessive kinetic energy and thus not release their entire kinetic energy in the sensitive detector medium. This means that the energy stored in the detector, and in the following the Light yield L of the scintillation photons sent to the photomultiplier, are no longer directly proportional to the energy of the incident γ-quantum; the correct pulse height is thereby reduced. These effects are likely to occur at higher energies, which is where the non-linearity can be caused. The aim of this study is not to find errors in the experimental set-up, but to compare the Red Pitaya and the Cassy system. In relation to the results of energy calibration, the Red Pitaya is able to replace the Leybold Cassy system.
However, due to the small size of the non-linearity, a linear relationship between μ of the peaks and the associated energy E can be assumed for both the Red Pitaya and the Cassy system.

4.3 Comparison of the Relative Energy Resolution Φ of the Red Pitaya/MCPHA and the Leybold Cassy System

Lastly, the relative energy resolution Φ of the two systems is compared. For this purpose, the Cs137 photopeaks at 662 keV are compared here as an example. The comparison of Φ for the remaining spectra, where the optimal operating voltage of the photomultiplier is selected for each radioactive source, can be seen in A.3.1.2 and reflects the results discussed here. The optimum voltage at the detector is 730 V for the MCPHA and 877 V for the Cassy, whereby an amplification factor of 1 can be set for the Cassy system in Cassy Lab 2. A typical oscillogram for the MCPHA is shown in Figure 4.5 and shows that, despite rates of up to 11 kS/s, pile-up effects can be assumed to be small. First of all, the relative resolution Φ for the Red Pitaya is $\Phi_{\mathrm{RP}} = 0.0316$[4] and for the Cassy system $\Phi_{\mathrm{Cassy}} = 0.0329$. This shows that the relative resolution Φ of both systems is therefore comparable.

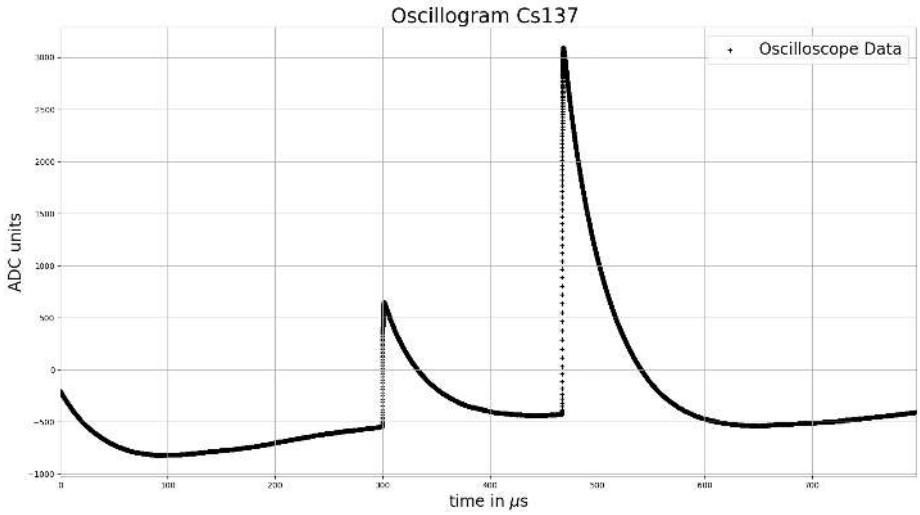

Figure 4.5: Recording from the oscilloscope during measurement of the Cs137 spectrum at 730V operating voltage.

Due to the higher operating voltage when measuring with the Cassy system, more pile-up occurs in comparison to the measurement with the Red Pitaya. This becomes clear when comparing Figures 4.6 and 4.7. The Cassy, however, has problems with pile-up and so the quality of the fit, $2\ln(\mathcal{L}_R)/\mathrm{ndf} = 5.325$, shows, what can apparently also be seen, that the peaks cannot be described very accurately by the fit function. In the range up to 850 V this had hardly any visible influence and only becomes apparent upon closer analysis. As can be seen from the remaining analysis of Φ, the two systems never deviate from each other by more than 8% and are never larger than $\Phi = 0.04$ with respect to the energy considered and with optimal operating voltage settings.

The conclusion of the comparison between the Leybold Cassy system and the Red Pitaya

[4] The uncertainty is not given because it is purely statistical in nature and the small statistical uncertainties on μ and σ do not provide much information. These uncertainties are highly dependent on the specified fit interval and the selected starting parameters, as well as the validity of the fit model.

system can be summarized as follows: The system consisting of the Red Pitaya STEMlab 125-14 and MCPHA by Pavel Denim can replace the Leybold Didactic system. It is not only the more cost-effective, modern and space-saving system, but also combines modern measurement methods with a transparent software architecture. At the time of publication of this study, the Red Pitaya system has been in use for a total of three months in the beginners physics lab at the Faculty of Physics in the experiment "γ-spectroscopy" and has received only positive feedback so far.

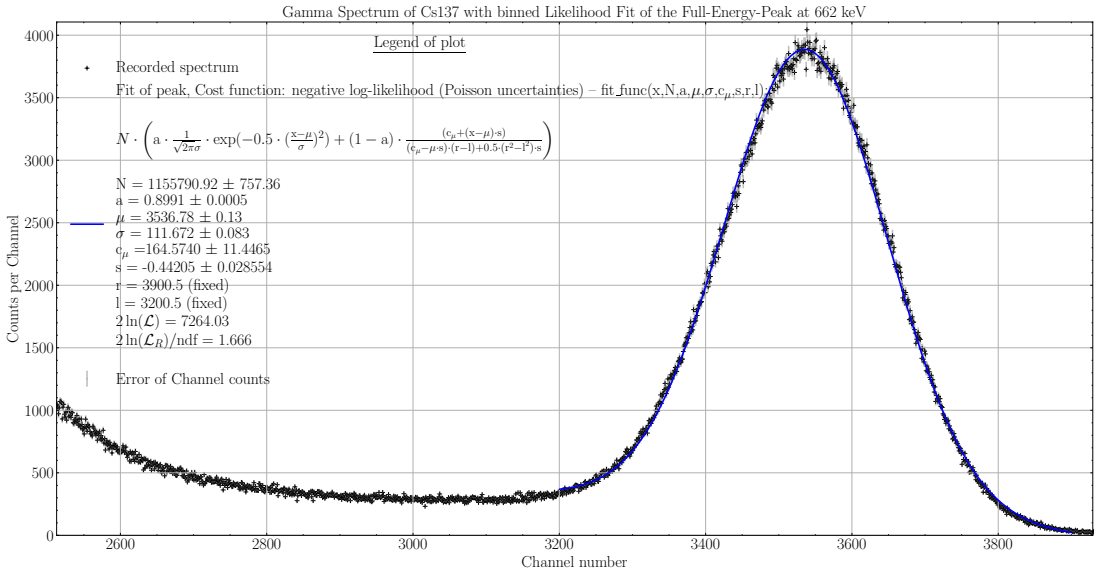

Figure 4.6: Analysis of the Cs137 662 keV photopeak at a detector voltage of 730 V, recorded with the MCPHA by Pavel Denim.

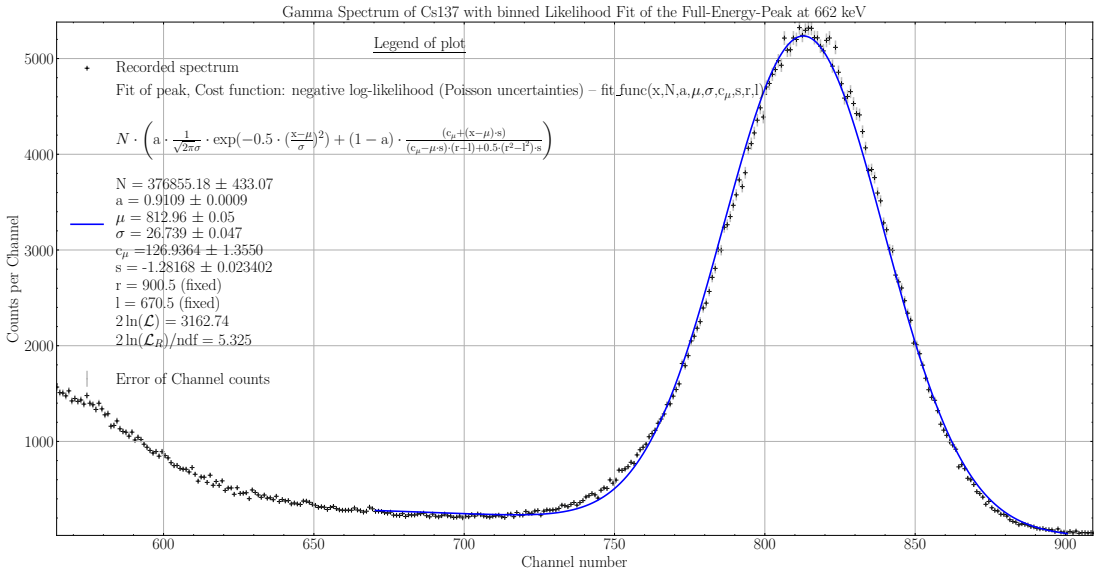

Figure 4.7: Analysis of the Cs137 662 keV photopeak at a detector voltage of 877 V, recorded with the Cassy Lab2.

CHAPTER 5

COMPARISON OF RED PITAYA AND THE MCA-SYSTEM BY FAST COMTEC

Since the previous chapter demonstrated that the system consisting of the Red Pitaya STEM-lab 125-14 and the MCPHA is suitable for recording γ-spectra using a NaI(Ti)-detector, this chapter covers the approach to use the system for recording γ-spectra using an HPGe-detector. Since semiconductor detectors promise a significantly better energy resolution, the Gaussian photopeaks are now significantly sharper. To evaluate the usability of the Red Pitaya, the already existing FAST ComTec system of the "γ-coincidence spectroscopy" experiment from the advanced physics lab of the Karlsruhe Institute of Technology is used.

5.1 Experimental Set-Up

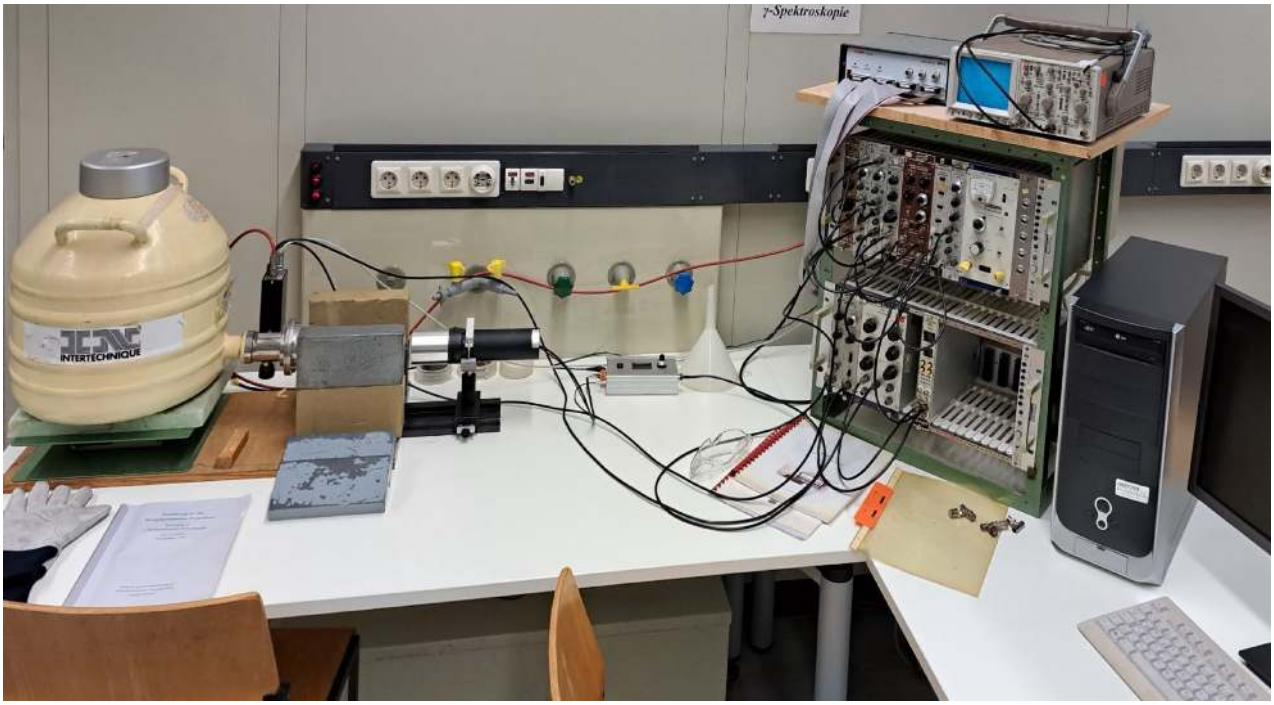

Figure 5.1: Experimental set-up of the "γ-coincidence spectroscopy"-experiment (Figure is taken from Chapter 7.9 [Wol23])

The fundamental experimental set-up used is shown in Figure 5.1. First of all, a Schlumberger HPGe detector type EGPP N° PP 102 with SBDF 9020 cryostat and an INTERTECHNIQUE liquid-nitrogen dewar are used.
A linear amplifier from ORTEC, MODEL 410, is used to amplify and shape the signals coming from the detector. It should be noted that for all measurement series, only the signal was amplified using the fine and coarse gain control dials, while the other settings, for integrating

and differentiating the signal, were retained.
The pulses from the unipolar Output of the amplifier are then either recorded via the IN1 of the Red Pitaya STEMlab 125-14 or via the QUAD ADC 7074 from FAST ComTec GmbH. In the case of the FAST ComTec system, the SPA-3 Singleparameter Data Acquisition System is used to record and process the signals, and the MPANT-software installed on the PC is used to graphically display and save the γ-spectra.
Due to a technical problem in the measurement setup, the cause of which is unclear, no measurement series longer than two minutes have been recorded, because the detector regularly "jumps" and shifts the position of the detected pulses in the spectrum. This "jumping" can be easily recognized by the course of the photopeak when observing the spectrum recording and the measurement can therefore be repeated when this effect occurs.

5.2 Comparison of the Relative Energy Resolution Φ of Red Pitaya/MCPHA and the FAST ComTec System

In the context of this study, multichannel measurements with 4096 channels are carried out for both the Red Pitaya system and the FAST ComTec system. To ensure optimal comparability of the relative energy resolution Φ, the photopeaks of the respective radioactive source in the spectra are shifted to the last third of the spectrum by adjusting the signal amplification, with the aim of achieving a similar channel number for the peak position through fine adjustment. The analysis of the photopeaks is carried out in the same way as in the previous chapter, whereby only Cs137 and Co60 sources were used.

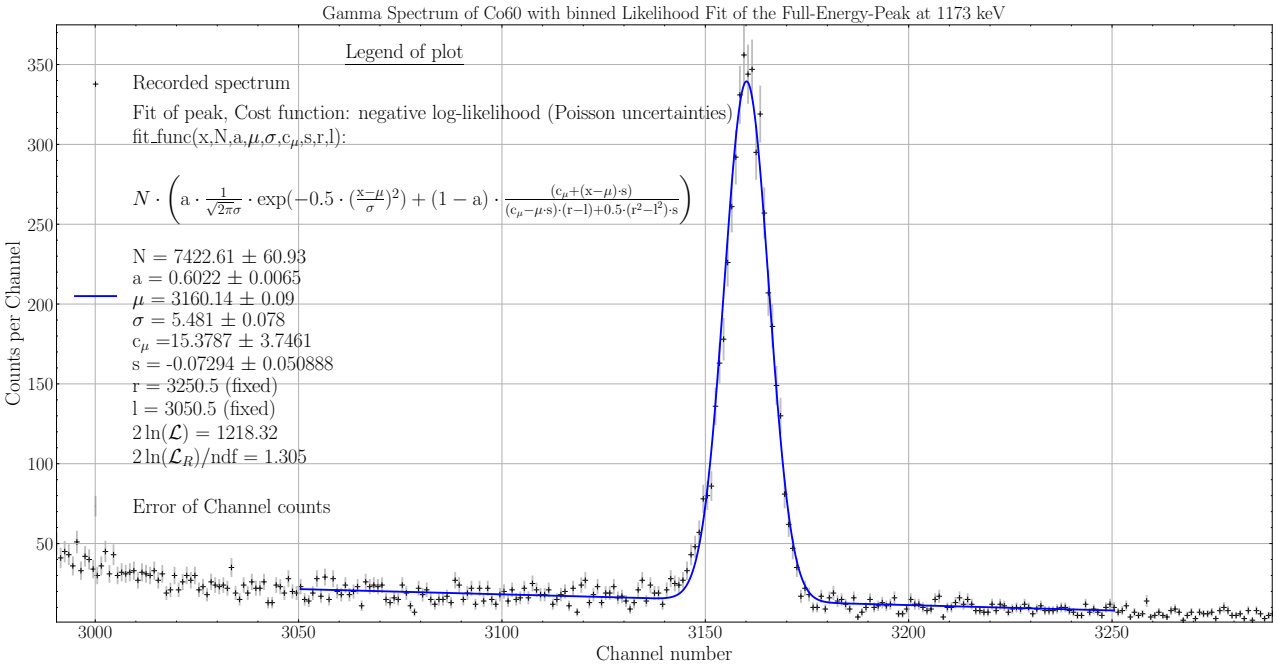

Figure 5.2: Analysis of the Co60 1173 keV photopeak, recorded with the MCPHA by Pavel Denim.

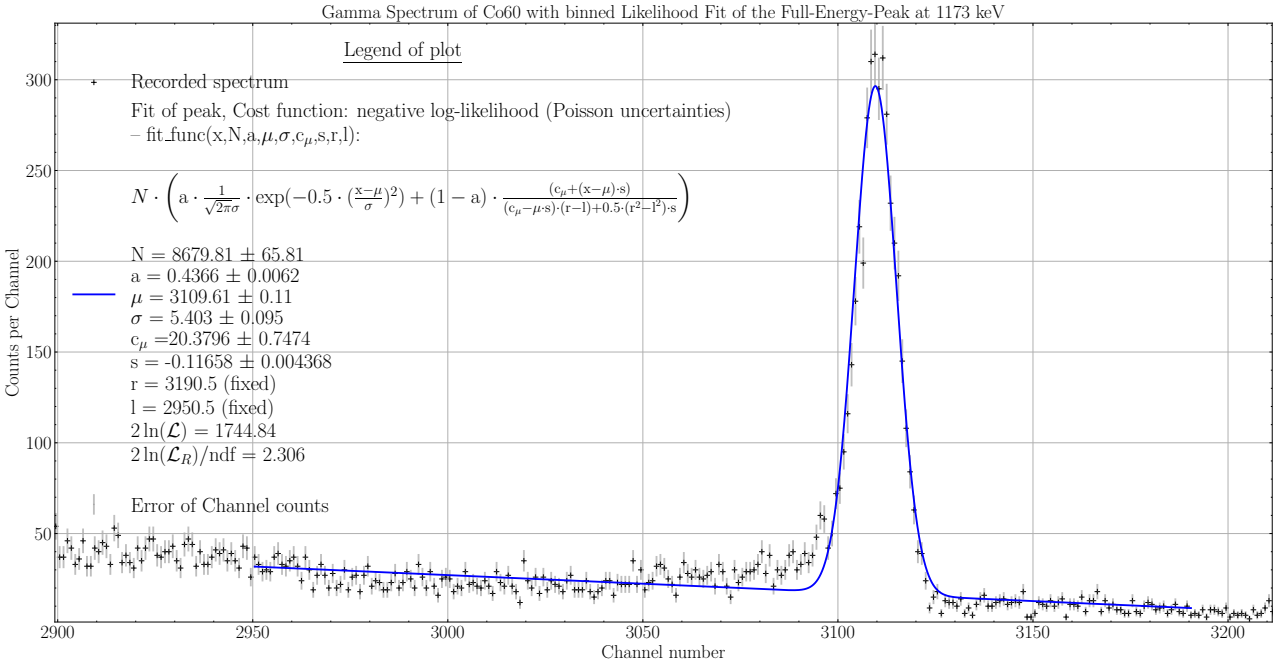

Figure 5.3: Analysis of the Co60 1173 keV photopeak, recorded with MPANT by FAST ComTec.

The results of this study are shown in Figures 5.3 & 5.2, illustrated by the Co60 photopeak at an energy of 1173 keV. The system consisting of Red Pitaya STEMlab 125-14 and MCPHA has a relative energy resolution of $\Phi_{\mathrm{RP}} = 0.00173$[1] in 1173 keV, and the FAST ComTec system has a relative energy resolution of $\Phi_{\mathrm{FC}} = 0.00174$ in 1173 keV. A similar result is provided by the analysis of the Cs137 photopeak at 662 keV, which is shown in the appendix A.3.2. There the relative energy resolution Φ is slightly better for the FAST ComTec system, but the deviations from the model are also stronger, especially the top of the peak, and the energy to be resolved is lower.
Both spectra indicate that the shape of the spectrum at the lower left flank of the peak, as well as at the top of the peak, differs significantly from that of a Gaussian with a linear background. This is much less noticeable for the Red Pitaya system than for the FastComtec system (c.f $2\ln(\mathcal{L}_R)/\mathrm{ndf}$). For this reason, only the right-hand side of the peak, including the upper left part, or only the upper part in the area around $\mu \pm \mathrm{FWHM}/2$, were analyzed during several fit procedures, which only produced insignificant changes in σ and μ in comparison to fitting the whole peak and are therefore not listed here.
Looking at the temporal course of the pulses, shown in Figure 5.4, which were recorded using the MCPHA-oscilloscope, it is clear that the pulses exhibit a bipolar pulse tail, despite unipolar pulse shaping. The reasons for this are to be found in the pulse shaping electronics (cf. [KW20]; Chapter 17.3).
The deviations of the spectra among themselves and from the model[2] can be explained by the fact that, on the one hand, the model is only a credible approximation, but on the other hand

[1] As in the previous chapter, the uncertainty is not given because it is purely statistical in nature and the small statistical uncertainties on μ and σ do not provide much information. These uncertainties are highly dependent on the specified fit interval and the selected starting parameters, as well as the validity of the fit model.

[2] Significant deviations of the recorded peaks from a Gaussian with a linear background always manifest themselves in the analysis as large uncertainties in the fit parameters s and c_μ, which, as in Figures 5.2 and 5.3, can become very large and often deviate from the parabolic approximation. Since this does not apply to the other parameters, this effect can be neglected.

the FAST ComTec system is more exposed to pile-up due to the stronger signal amplification, as can be seen during the measurement in the oscilloscope, and due to the different pulse height analysis between MCPHA by Pavel Denim and the MCA by FAST ComTec, especially the determination of the baseline level. The extensions on the lower left flank of the peaks may also arise from boundary effects caused by electrons escaping from the sensitive volume (cf. 4.2), which always results in shifts to smaller values, never to larger ones.

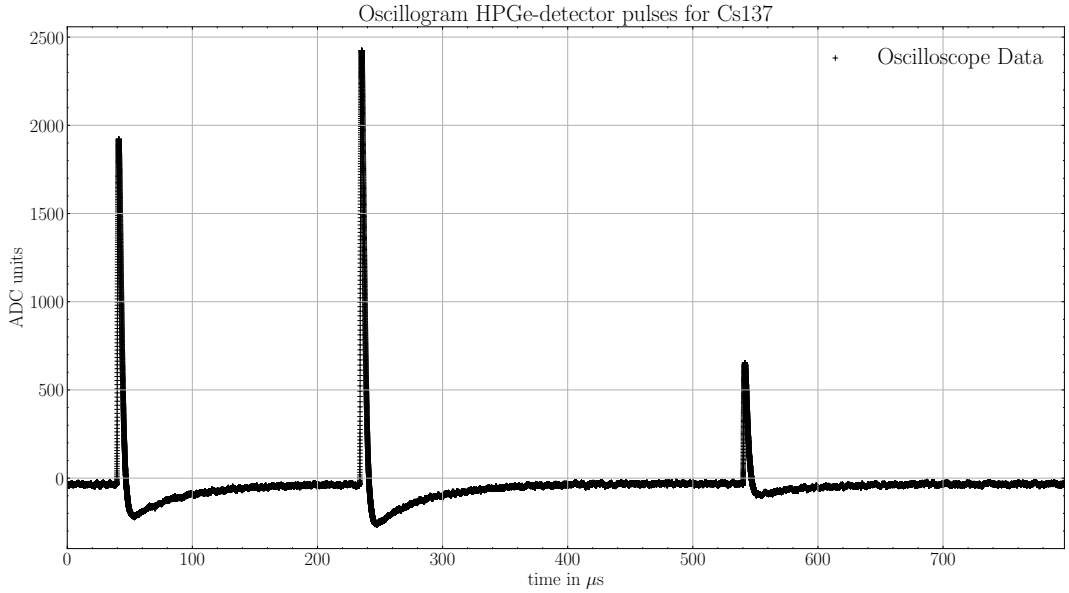

Figure 5.4: Recording from the oscilloscope during the Red Pitaya STEMlab 125-14 measurement of the Cs137 spectrum with the HPGe-detector.

5.3 Comparison of Red Pitaya STEMlab 125-14 Low Noise and Red Pitaya STEMlab 125-14

In the last part of this study, the analysis of the relative energy resolution between the Red Pitaya STEMlab 125-14 and the Low-Noise variant is done. This is also demonstrated by the Co60 photopeak at 1173 keV, as shown in Figures 5.5 and 5.6. The same settings were used in the amplifier electronics for both measurements. To minimize the recording time, as this also helps to prevent the detector from "jumping", a total of three identical Co60 sources are used, which increases the signal rate while the oscilloscope shows almost no pile-up.
For the Low-Noise variant, this results in a relative energy resolution of $\Phi_{\mathrm{LN}} = 0.00145$ and for the standard variant $\Phi_{\mathrm{St}} = 0.00152$. This result is reflected in several series of measurements, with the Red Pitaya STEMlab 125-14 Low Noise always providing a slightly better relative energy resolution for various radioactive sources and signal amplifications. Thereby for the recording of γ-spectra and a focus on energy resolution, the Low-Noise variant does not provide any significant benefits in relation to its higher price.

In conclusion, this study allows us to state that the Red Pitaya STEMlab 125-14 and the MCPHA are suitable for recording γ-spectra with HPGe-detectors and can replace the FAST ComTEC system in terms of energy resolution. Its ease of use allows data to be recorded and analysed much faster and, due to the additionally integrated oscilloscope, it is significantly more space-saving and also better in terms of price-performance than the outdated FAST ComTec

system.

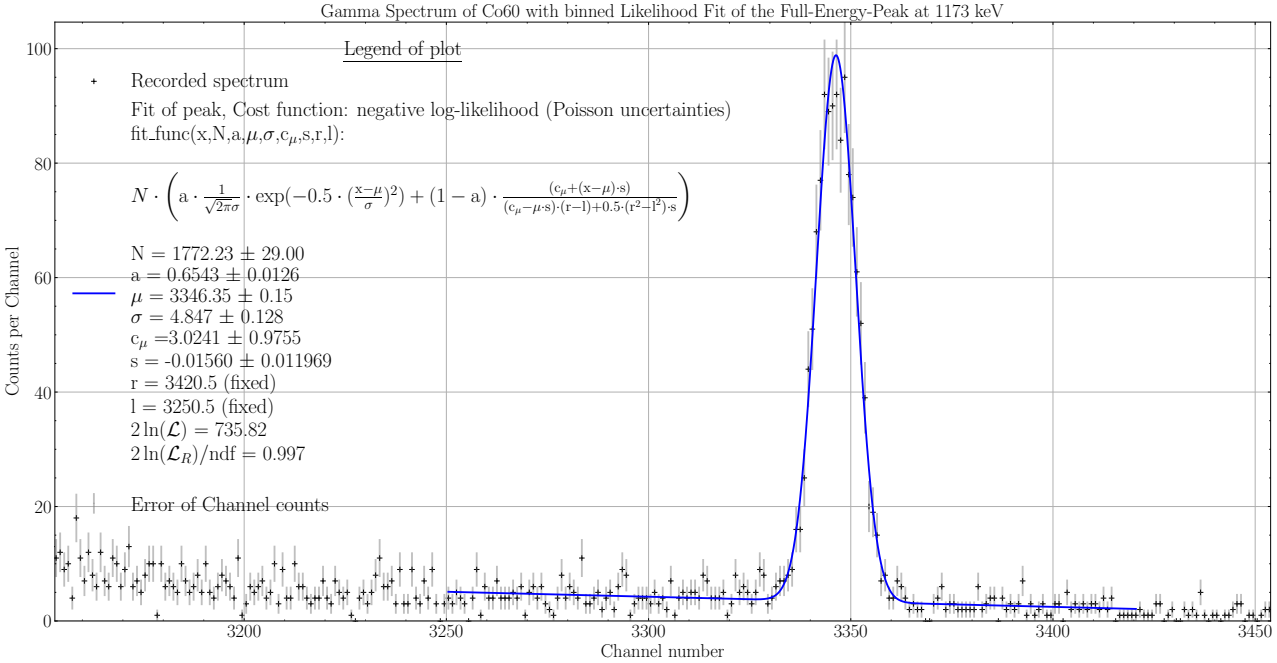

Figure 5.5: Analysis of the Co60 1173 keV photopeak, recorded with the MCPHA by Pavel Denim - Low Noise Red Pitaya STEMlab 125-14

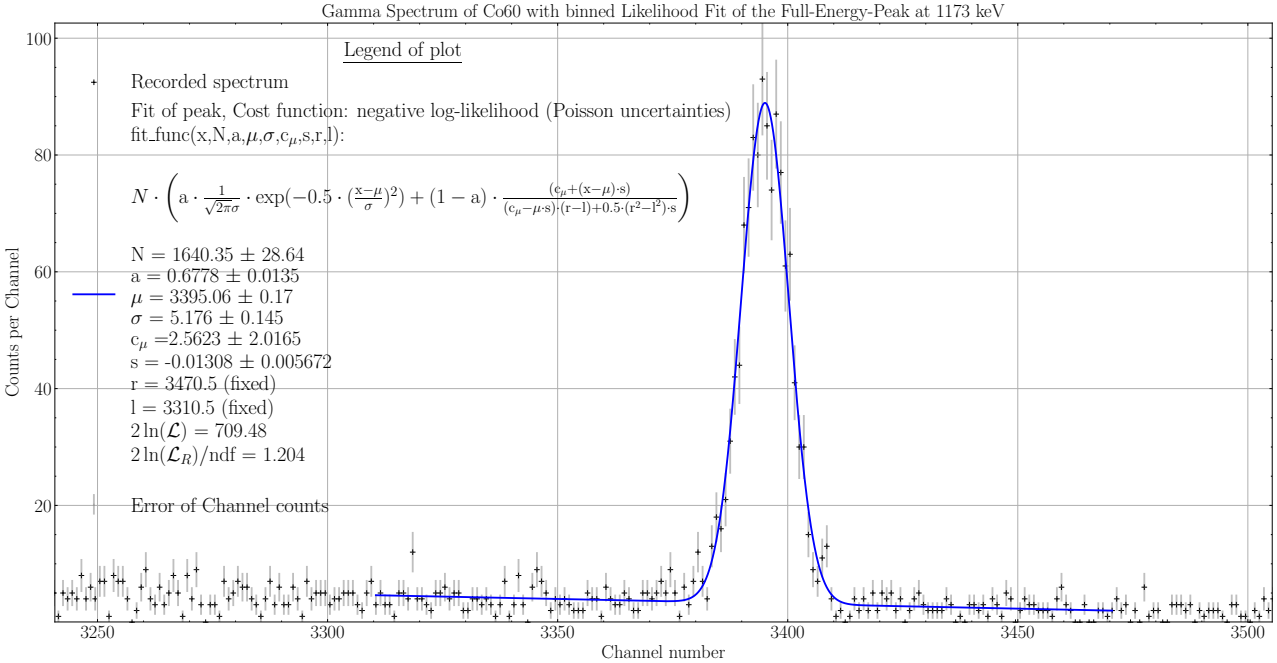

Figure 5.6: Analysis of the Co60 1173 keV photopeak, recorded with the MCPHA by Pavel Denim - Standard Red Pitaya STEMlab 125-14

CHAPTER 6

CONCLUSION AND OUTLOOK

This study aimed to evaluate the suitability of the Red Pitaya STEMlab 125-14 in combination with the MCPHA by Pavel Denim for recording γ-spectra in the physics lab of the Karlsruhe Institute of Technology. There is no doubt about the fact that the Red Pitaya system is suitable for recording and displaying γ-spectra in physics labs. The system impresses with its ease of use and was able to replace a large part of the outdated experimental set-ups to an equal extent. Despite some weaknesses of the MCPHA, e.g. the non-use of calibration data or poor documentation of the source code and software applications, the system provides a solid basis for further improvements and advanced applications in spectroscopy.
The feedback from students who are already using the system at the time of publication of the thesis has also been consistently positive.
However, it should be noted that although the system is sufficient for educational purposes, the same cannot yet be said about professional applications in the field of spectroscopy. At the time of publication of this study, further studies are in progress to investigate not only the energy resolution of the Red Pitaya STEM Lab 125-14 system in combination with the MCPHA, but also the suitability to use the system for time-dependent applications like in coincidence-spectroscopy.

APPENDIX A

PROGRAM CODE, TABLES & PLOTS

A.1 Example of Analysis Code for Photopeaks

```
import numpy as np
import matplotlib.pyplot as plt
from scipy.signal import find_peaks
from scipy.optimize import curve_fit
from matplotlib.gridspec import GridSpec
from kafe2 import XYContainer,XYFit, HistContainer,HistFit
import kafe2
import scienceplots

#Settings
plt.style.use("science")
plt.rcParams["text.usetex"] = True
#Fit Function
def fit_func(x,N,a,mu,sig,c_mu,s,r,l) :
    return N*(a*np.exp(-1/2*((x-mu)/sig)**2)* 1/(sig * np.sqrt(2*np.pi)) + (
                                        1-a)*(c_mu + (x-mu)*s)/((c_mu - mu
                                        *s)*(r-l)+(1/2*(r**2-l**2))*s) )
# load data
file = 'Na22_679V_2.hst'
#save data
fit_results = np.array([])
hst1 = np.loadtxt(file,dtype=np.uint32)
hst = hst1[0:4096]
x_hst = np.linspace(0.5,4095.5,4096)
# Create HistContainer for data
bin_edges_hist = np.linspace(0,4096,4097)
xy_data = HistContainer(bin_edges= bin_edges_hist)
xy_data.set_bins(hst)
xy_data.label = 'Spektrum'
# Peakfinder
indices_besser = find_peaks(hst[1100:1600], height = 200, distance = 200,
                                        width = 10,prominence= 200) #returns
                                        dictionary
peaks_RP  = indices_besser[0]+1100 #gives indices of peak
y_data_Peaks= indices_besser[1]["peak_heights"]
y_data_prominence = indices_besser[1]["prominences"]
c_mu = y_data_Peaks-y_data_prominence
peaks = XYContainer(x_data = peaks_RP, y_data= indices_besser[1]["
                                        peak_heights"])
peaks.label = "Peaks of scipy.signal.find_peaks"
# Define Fit-Borders by looking in the spectrum
RP_xlim = np.array([1150.5,1630.5])

# Red-Pitaya Fit and Plot
fit_results = np.array([])
index_Peak = 0
```

```
xlim_links = RP_xlim[0]
xlim_rechts = RP_xlim[1]
# Determine x-range for fit
len = int(xlim_rechts-xlim_links)
x_plot = np.linspace(xlim_links,xlim_rechts,100000)
x_r = np.linspace(xlim_links,xlim_rechts,len+1)
x_range = np.linspace(xlim_links-0.5,xlim_rechts+0.5,len+2)
y_range = hst1[int(xlim_links-0.5):int(xlim_rechts+0.5)]
err_val = np.sqrt(y_range)
xy_data_fit = HistContainer(bin_edges= x_range)# HistContainer for fitting
                                        the peak interval
xy_data_fit.set_bins(y_range)
xy_data_fit.label = " Counts in fit-range "+str(index_Peak+1)
#Fit
Ergebnis_Fit = HistFit(data = xy_data_fit, model_function= fit_func,density=
                                         False, cost_function="poisson") # NLL
                                        -method with poisson-uncertainties and
                                         binned Histogramm Fit with kafe2
#Determine N = Counts in fit-interval
N_start = 0
for k in x_r :
    N_start = hst1[int(k)] + N_start
#Set starting values
s_start = -0.236 #determined by gradient triangle
c_mu_start = c_mu[index_Peak]
sig_start = indices_besser[1]["widths"][index_Peak]/2.3548
a_start = y_data_prominence[index_Peak]/y_data_Peaks[index_Peak]
Ergebnis_Fit.set_parameter_values(mu = peaks_RP[index_Peak]+0.5,sig=
                                        sig_start, a = a_start,s = s_start,
                                        c_mu = c_mu_start)
Ergebnis_Fit.limit_parameter("sig",0.4*sig_start,1.5*sig_start)
Ergebnis_Fit.limit_parameter("a",0,1)
Ergebnis_Fit.limit_parameter("s",1.5*s_start,0.5*s_start)
Ergebnis_Fit.limit_parameter("mu",peaks_RP[index_Peak]-30,peaks_RP[
                                        index_Peak]+30)#always good agreement
Ergebnis_Fit.limit_parameter("c_mu",c_mu_start*0.5,1.5*c_mu_start)
Ergebnis_Fit.fix_parameter("r",xlim_rechts)
Ergebnis_Fit.fix_parameter("l",xlim_links)
Ergebnis_Fit.add_parameter_constraint(name = "N", value = N_start,
                                        uncertainty= np.sqrt(N_start),
                                        relative = False)

Ergebnis_Fit.do_fit(asymmetric_parameter_errors=True)
fit_results = np.append(fit_results,Ergebnis_Fit)
Ergebnis_Fit.report(asymmetric_parameter_errors=True)

par_values = Ergebnis_Fit.parameter_values
par_errors = Ergebnis_Fit.parameter_errors
GoF = Ergebnis_Fit.goodness_of_fit
ndf = Ergebnis_Fit.ndf
cost = Ergebnis_Fit.cost_function_value
guete= GoF/ndf
#Plot of Fit with matplotlib
fig = plt.figure(tight_layout = True,figsize=(20,20))
gs = GridSpec(4,4, figure = fig)
ax1 = fig.add_subplot(gs[:, :])
ax1.set_title(r"Gamma Spectrum of Na22 with binned Likelihood Fit of the
                                        Full-Energy-Peak at 511 keV",fontsize
```

```
                                        = 20)
ax1.set_xlabel(r"Channel number",fontsize = 20)
ax1.set_ylabel(r"Counts per Channel",fontsize = 20)
ax1.errorbar(x_hst, hst, yerr=np.sqrt(hst), zorder=1, label=r'Error of
                                        Channel counts',
                fmt='.', color='grey', markersize=1, linewidth=2, alpha=0.5
                                                                )
ax1.scatter(x_hst,hst ,color = "black",label = r"Recorded spectrum",marker =
                                         "+",zorder=1)
ax1.plot(x_plot,fit_func(x_plot,*par_values),zorder = 3,linewidth = 2,color
                                        = "blue",label = r"Fit of peak, Cost
                                        function: negative log-likelihood (
                                        Poisson uncertainties) -- fit_func(x,N
                                        ,a,$\mu$,$\sigma$,$\text{c}_{\mu}$,s,r
                                        ,l):"+
        "\n"+
        "\n"+r"$N \cdot \biggl(\text{a} \cdot \frac{1}{\sqrt{2\pi}\sigma}\
                                                cdot \exp(-0.5 \cdot (\frac{\
                                                text{x}-\mu}{\sigma})^2)+ (1
                                                -\text{a}) \cdot \frac{(\text
                                                {c}_\mu + (\text{x}-\mu) \
                                                cdot \text{s})}{(\text{c}_\mu
                                                - \mu \cdot \text{s})\cdot(\
                                                text{r}-\text{l})+ 0.5 \cdot
                                                (\text{r}^2-\text{l}^2)\cdot
                                                \text{s}} \biggl)$"+
        "\n"+
        "\n"+" \t N = {:.2f} $\pm$ {:.2f}".format(par_values[0],par_errors[
                                                0])+
        "\n"+"a = {:.4f} $\pm$ {:.4f}".format(par_values[1],par_errors[1])+
        "\n"+"$\mu$ = {:.2f} $\pm$ {:.2f}".format(par_values[2],par_errors[
                                                2])+
        "\n"+"$\sigma$ = {:.3f} $\pm$ {:.3f}".format(par_values[3],
                                                par_errors[3])+
        "\n"+r"$\text{c}_\mu$ ="+ "{:.4f} $\pm$ {:.4f}".format(par_values[4
                                                ],par_errors[4])+
        "\n"+"s = {:.5f} $\pm$ {:.6f}".format(par_values[5],par_errors[5])+
        "\n"+"r = {} (fixed)".format(par_values[6])+
        "\n"+"l = {} (fixed)".format(par_values[7])+
        "\n"+ r"$2\ln(\mathcal{L})$ = "+"{:.2f}".format(cost)+
        "\n"+ r"$2\ln(\mathcal{L}_R)/\text{ndf}$ = "+"{:.3f}".format(guete)
                                                +"\n")
ax1.legend(loc = "upper left",title = r"\underline{Legend of plot}",fontsize
                                         = 25, title_fontsize = 30)
ax1.autoscale(tight = True)
ax1.grid()
plt.show()
```

A.2 Measurement Tables

A.2.1 Chapter 1 - Analysis of the ADC linearity

Table A.1: Measured values of the DC voltage with the oscilloscope in OS 2.00-30

Imput Voltage in mV	Factory calibration in mV	Default in mV	Auto DC calibration in mV
20.0	19.7	8.9	20.0
50.1	49.9	37.6	50.1
100.6	100.1	84.8	100.6
200.1	199.6	179.2	200.5
250.3	249.9	226.2	250.9
350.4	349.7	320.9	351.0
400.3	399.4	368.6	401.0
500.1	499.2	462.8	501.1
650.0	649.1	604.6	651.2
701.0	700.1	652.3	702.1
800.0	798.2	745.8	801.3
851.0	849.1	794.7	852.9
900.0	898.7	841.4	902.2
950.0	948.2	889.4	952.3
1000.0	997.9	935.9	1000

Table A.2: Measured values of the DC voltage with the MCPHA by Pavel Denim

Imput Voltage in mV	MCPHA in mV
20.0	9.0
50.1	34.5
100.6	80.0
200.1	167.0
250.3	211.0
350.4	299.0
400.3	343.5
500.1	431.5
650.0	564.0
701.0	608.0
800.0	697.0
851.0	739.5
900.0	784.0
950.0	827.5
1000.0	871.0

A.2.2 Chapter 1 - Analysis of the Pulse Generator

Red-marked fall times indicate that a pile-up can be seen in the oscilloscope from that point. Brown-marked fall times indicate that a strong background can be seen in the spectrum and that the peaks are heavily distorted. The fall time is always given in μs and μ & σ in channel numbers.

Table A.3: Measured values of the Peak position for rate = 1 ksps and rise time = 50 ns

fall time		Peak2	Peak 4	Peak 6	Peak 8	Peak 10	Peak 12	Peak 14	Peak 16
5	σ	0.996	0.926	0.919	0.944	0.922	0.91	0.916	0.894
	μ	275.17	550.56	826.35	1101.69	1377.15	1652.0	1926.87	2201.62
8	σ	1.111	1.004	0.943	0.962	0.915	0.934	0.901	0.941
	μ	274.773	550.393	826.268	1101.958	1377.37	1652.297	1927.18	2202.058
10	σ	1.123	1.017	1.015	0.983	0.941	0.946	0.943	0.903
	μ	274.71	550.347	826.21	1101.765	1377.257	1652.131	1927.135	2201.952
20	σ	1.164	1.115	1.077	1.056	1.019	0.96	0.971	0.954
	μ	274.243	549.58	825.738	1101.168	1376.559	1651.695	1926.371	2201.289
40	σ	1.181	1.137	1.108	1.065	1.032	1.047	1.041	0.973
	μ	273.74	549.165	824.796	1100.266	1375.901	1650.807	1925.488	2200.063
50	σ	1.201	1.165	1.123	1.119	1.071	1.039	1.055	1.04
	μ	273.806	549.073	824.93	1100.27	1375.69	1650.379	1925.267	2199.898
80	σ	1.185	1.175	1.13	1.13	1.066	1.072	1.066	1.024
	μ	273.466	548.541	824.422	1099.957	1375.358	1650.212	1924.985	2199.795
90	σ	1.201	1.146	1.11	1.151	1.125	1.054	1.08	1.038
	μ	273.437	548.593	824.188	1099.952	1375.143	1649.684	1924.695	2199.297
100	σ	1.222	1.197	1.141	1.108	1.092	1.066	1.08	1.078
	μ	273.474	548.591	824.181	1099.916	1375.069	1649.631	1924.694	2199.239

Table A.4: Measured values of the Peak position rate = 3 ksps and rise time = 50 ns

fall time		Peak2	Peak 4	Peak 6	Peak 8	Peak 10	Peak 12	Peak 14	Peak 16
5	σ	1.039	0.947	0.927	0.943	0.931	0.918	0.918	0.917
	μ	275.171	550.566	826.306	1101.745	1377.164	1651.965	1926.827	2201.58
8	σ	1.087	1.015	0.966	0.948	0.948	0.939	0.932	0.937
	μ	274.779	550.363	826.19	1101.875	1377.218	1652.141	1926.977	2201.808
10	σ	1.093	1.014	1.013	0.975	0.97	0.938	0.935	0.94
	μ	274.654	550.254	826.079	1101.63	1377.104	1651.919	1926.92	2201.682
20	σ	1.164	1.111	1.041	1.011	0.998	0.977	0.976	0.984
	μ	274.205	549.47	825.626	1101.05	1376.417	1651.458	1926.205	2201.082
40	σ	1.209	1.148	1.111	1.055	1.05	1.038	1.026	1.013
	μ	273.805	549.053	824.635	1100.078	1375.626	1650.514	1925.164	2199.678
50	σ	1.21	1.164	1.115	1.118	1.068	1.052	1.029	1.044
	μ	273.77	548.983	824.782	1100.138	1375.449	1650.187	1924.928	2199.517
70	σ	1.339	1.188	1.186	1.162	1.216	1.154	1.141	1.204
	μ	272.964	548.276	824.045	1099.515	1374.703	1649.561	1924.365	2198.954
80	σ	1.354	1.201	1.195	1.16	1.227	1.153	1.14	1.218
	μ	272.976	548.291	824.046	1099.473	1374.651	1649.484	1924.274	2198.833
100	σ	1.403	1.24	1.197	1.263	1.314	1.183	1.242	1.286
	μ	272.63	548.097	823.566	1099.072	1373.981	1648.698	1923.546	2197.934

Table A.5: Measured values of the Peak position for rate = 5 ksps and rise time = 50 ns

fall time		Peak2	Peak 4	Peak 6	Peak 8	Peak 10	Peak 12	Peak 14	Peak 16
5	σ	1.015	0.958	0.94	0.939	0.928	0.921	0.917	0.901
	μ	275.157	550.447	826.167	1101.555	1376.923	1651.688	1926.519	2201.199
8	σ	1.092	0.986	0.951	0.947	0.945	0.921	0.929	0.933
	μ	274.732	550.282	826.163	1101.713	1377.089	1651.975	1926.777	2201.609
10	σ	1.122	1.02	0.989	0.994	0.962	0.941	0.94	0.943
	μ	274.597	550.13	825.917	1101.399	1376.814	1651.581	1926.511	2201.205
20	σ	1.167	1.099	1.054	1.028	1.024	0.979	0.988	0.979
	μ	274.148	549.344	825.428	1100.789	1376.091	1651.063	1925.768	2200.568
40	σ	1.429	1.244	1.159	1.138	1.299	1.226	1.135	1.139
	μ	272.955	548.552	824.114	1099.444	1374.57	1649.482	1924.148	2198.564
50	σ	1.441	1.27	1.289	1.219	1.304	1.24	1.208	1.292
	μ	272.485	548.053	823.673	1099.009	1373.88	1648.724	1923.42	2197.77
80	σ	1.39	1.306	1.321	1.337	1.37	1.368	1.397	1.497
	μ	271.729	547.435	822.853	1098.153	1372.919	1647.779	1922.404	2196.581
90	σ	1.389	1.284	1.31	1.308	1.361	1.343	1.388	1.494
	μ	271.805	547.527	823.019	1098.394	1373.197	1648.098	1922.824	2197.045
100	σ	1.289	1.284	1.256	1.417	1.356	1.39	1.522	1.48
	μ	271.582	547.122	822.505	1097.547	1372.274	1647.078	1921.527	2195.735

Table A.6: Measured values of the Peak position for rate = 10 ksps and rise time = 50 ns

fall time		Peak2	Peak 4	Peak 6	Peak 8	Peak 10	Peak 12	Peak 14	Peak 16
5	σ	1.034	0.973	0.944	0.935	0.929	0.92	0.919	0.923
	μ	275.044	550.286	825.876	1101.208	1376.524	1651.203	1925.952	2200.566
8	σ	1.103	1.007	0.975	0.951	0.936	0.947	0.941	0.922
	μ	274.625	550.1	825.835	1101.336	1376.607	1651.407	1926.113	2200.847
10	σ	1.1	1.033	0.98	0.987	0.957	0.946	0.934	0.952
	μ	274.589	550.079	825.848	1101.334	1376.693	1651.487	1926.383	2201.076
20	σ	1.383	1.191	1.191	1.149	1.215	1.182	1.12	1.215
	μ	272.894	548.771	824.567	1100.072	1375.013	1650.051	1924.92	2199.429
40	σ	1.412	1.427	1.419	1.603	1.553	1.576	1.714	1.682
	μ	271.082	546.801	822.233	1097.4	1372.159	1647.02	1921.6	2195.868
50	σ	1.423	1.544	1.669	1.823	1.765	1.928	2.035	2.111
	μ	270.537	546.096	821.356	1096.274	1371.114	1645.735	1920.131	2194.364
70	σ	1.649	1.888	2.079	2.13	2.334	2.51	2.706	2.891
	μ	269.858	544.985	819.997	1094.785	1369.393	1643.839	1917.915	2191.827
80	σ	1.651	1.922	2.085	2.115	2.334	2.525	2.685	2.881
	μ	269.827	544.931	819.938	1094.655	1369.284	1643.704	1917.817	2191.722
100	σ	1.8	2.005	2.205	2.381	2.607	2.831	3.105	3.389
	μ	269.222	544.143	818.904	1093.403	1367.795	1641.98	1915.863	2189.514

Table A.7: Measured values of the Peak position for rate = 20 ksps and rise time = 50 ns

fall time		Peak2	Peak 4	Peak 6	Peak 8	Peak 10	Peak 12	Peak 14	Peak 16
5	σ	1.01	0.972	0.934	0.928	0.921	0.911	0.91	0.922
	μ	275.203	550.532	826.216	1101.602	1376.996	1651.76	1926.586	2201.291
8	σ	1.103	1.007	0.975	0.951	0.936	0.947	0.941	0.922
	μ	274.625	550.1	825.835	1101.336	1376.607	1651.407	1926.113	2200.847
10	σ	1.349	1.236	1.187	1.182	1.239	1.203	1.21	1.249
	μ	272.762	548.715	824.445	1099.936	1374.839	1649.84	1924.748	2199.208
20	σ	1.832	1.937	2.004	2.262	2.169	2.217	2.617	2.369
	μ	269.788	545.513	820.991	1096.151	1371.005	1645.924	1920.543	2194.834
40	σ	2.544	2.891	3.133	3.289	3.547	3.79	3.98	4.233
	μ	266.867	541.702	816.502	1091.15	1365.659	1639.86	1913.905	2187.695

Table A.8: Measured values of the Peak position for rate = 30 ksps and rise time = 50 ns

fall time		Peak2	Peak 4	Peak 6	Peak 8	Peak 10	Peak 12	Peak 14	Peak 16
5	σ	1.216	1.079	0.952	1.035	1.112	1.062	1.054	1.095
	μ	273.791	549.544	824.879	1100.515	1375.419	1650.301	1925.119	2199.528
8	σ	1.57	1.581	1.612	1.601	1.654	1.637	1.66	1.678
	μ	271.626	547.605	823.331	1098.854	1373.681	1648.795	1923.73	2198.174
10	σ	2.099	2.114	2.186	2.202	2.235	2.299	2.355	2.418
	μ	270.119	545.97	821.51	1096.939	1371.668	1646.653	1921.452	2195.771
20	σ	3.04	3.415	3.769	3.892	3.996	4.292	4.393	4.59
	μ	265.974	541.089	816.046	1090.875	1365.655	1640.16	1914.474	2188.535
40	σ	3.331	3.871	4.296	4.707	5.064	5.508	5.748	5.821
	μ	262.021	535.957	810.074	1084.092	1357.983	1631.597	1905.233	2179.118

Table A.9: Measured values of the Peak position for rate = 50 ksps and rise time = 50 ns

fall time		Peak2	Peak 4	Peak 6	Peak 8	Peak 10	Peak 12	Peak 14	Peak 16
5	σ	2.223	2.291	2.36	2.376	2.436	2.406	2.453	2.486
	μ	270.24	545.898	821.37	1096.663	1371.289	1646.195	1920.958	2195.179
8	σ	3.661	3.981	4.123	4.469	4.406	4.451	4.694	4.625
	μ	265.6	541.041	816.329	1091.405	1366.157	1640.999	1915.542	2189.801
10	σ	4.217	4.677	5.058	5.291	5.292	5.585	5.715	5.909
	μ	263.473	538.581	813.697	1088.536	1363.252	1637.826	1912.331	2186.356
20	σ	5.059	5.85	6.391	6.909	7.363	7.588	8.046	8.69
	μ	257.331	531.189	805.123	1079.631	1353.225	1627.552	1903.323	2174.043

A.3 Additional Plots

It should be noted that, due to the maximum correlation of the parameters s and c_μ, large uncertainties often occur. These can be reduced by skillfully choosing the starting values, but it turned out that these uncertainties are irrelevant for the parameters σ and μ and their statistical uncertainty. The energy of the photopeaks is given below without decimal places, for the energy calibration the exact value is used.

A.3.1 Chapter 4- Comparison of Red Pitaya and the Leybold Cassy System

A.3.1.1 Energy Calibration

Na22

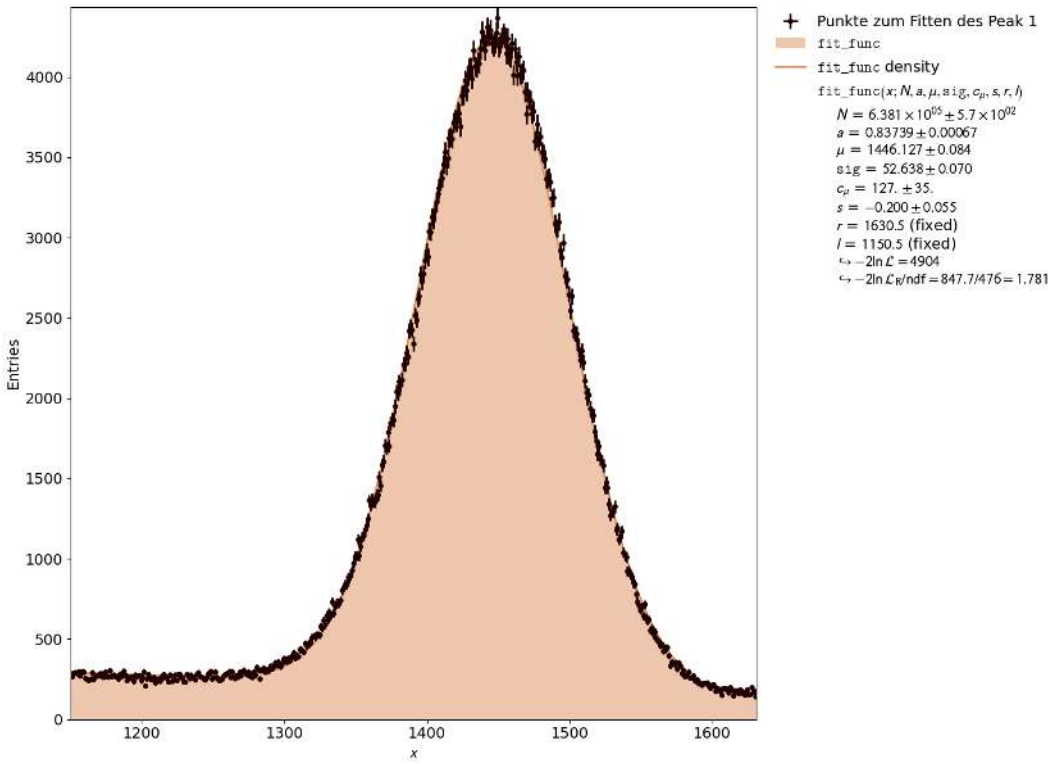

Figure A.1: Analysis of the Na22 511 keV annihilation peak at a detector voltage of 679 V, recorded with the MCPHA by Pavel Denim. $\Phi = 0.0364$

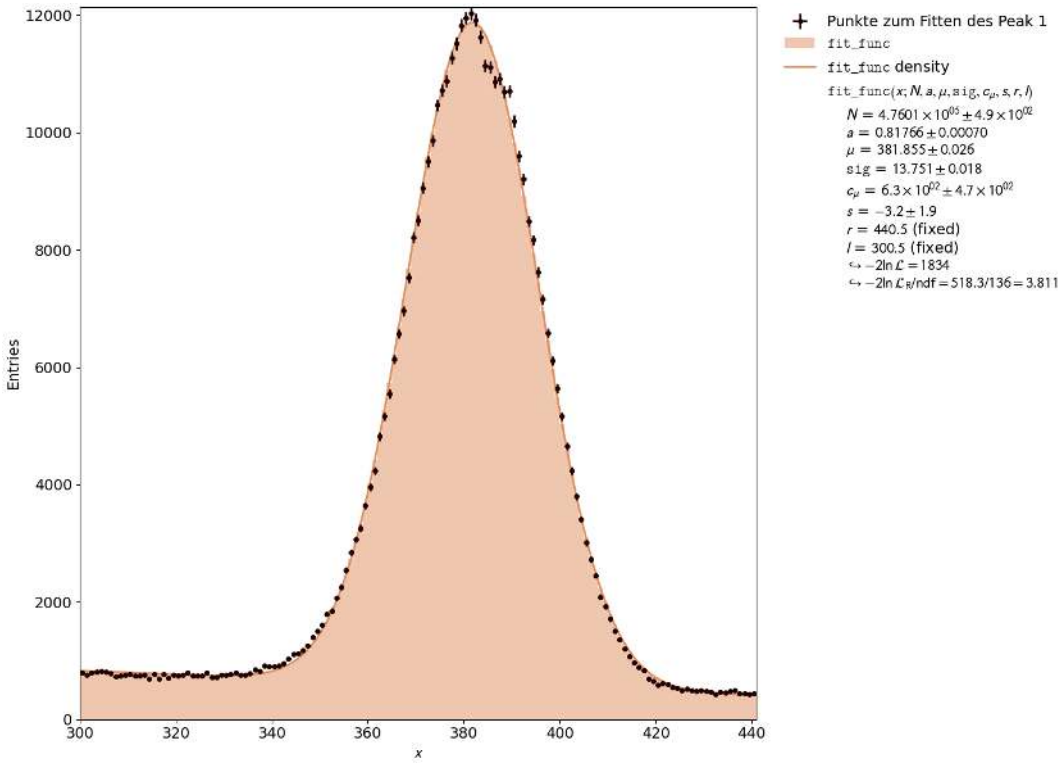

Figure A.2: Analysis of the Na22 511 keV annihilation peak at a detector voltage of 679 V, recorded with the Cassy Lab2 and internal amplification factor 5.52. $\Phi = 0.0360$

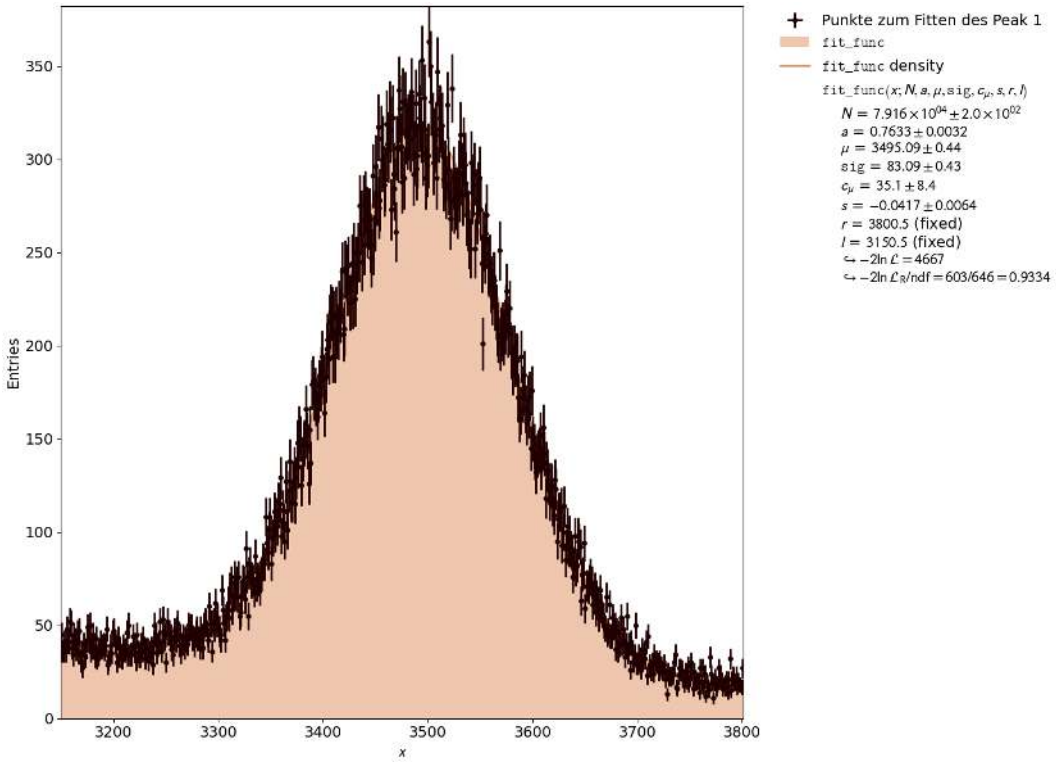

Figure A.3: Analysis of the Na22 1275 keV photopeak at a detector voltage of 679 V, recorded with the MCPHA by Pavel Denim. $\Phi = 0.0238$

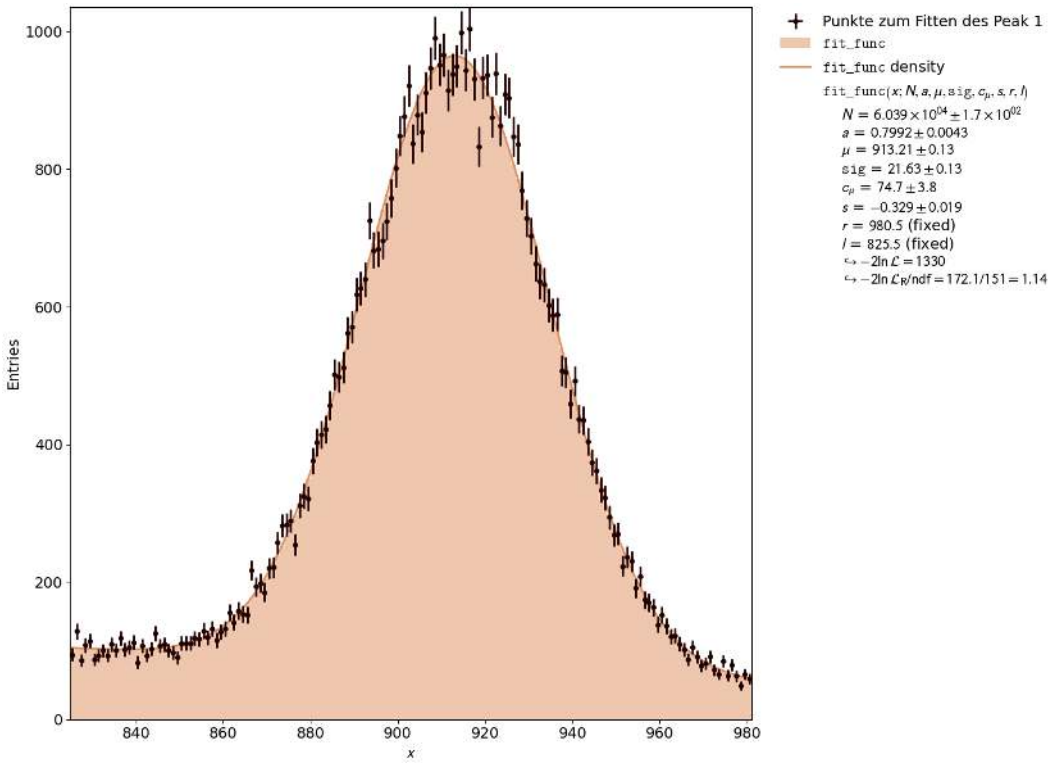

Figure A.4: Analysis of the Na22 1275 keV photopeak at a detector voltage of 679 V, recorded with the Cassy Lab2 and internal amplification factor 5.52. $\Phi = 0.0237$

Cs137

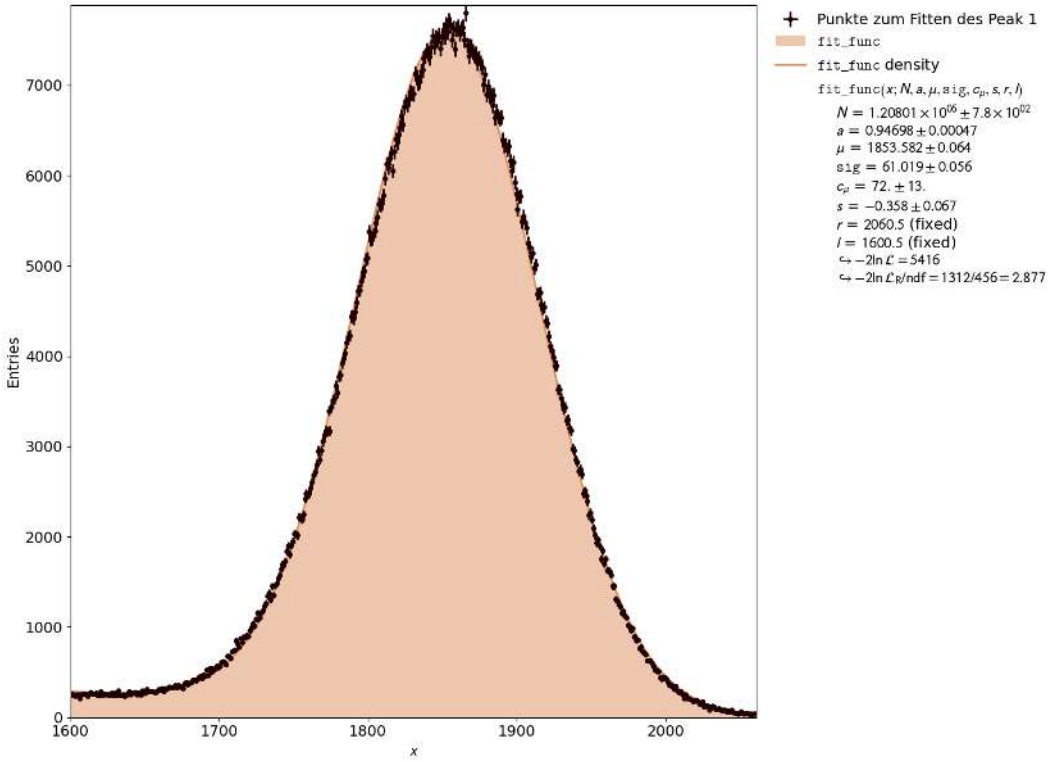

Figure A.5: Analysis of the Cs137 662keV photopeak at a detector voltage of 679 V, recorded with the MCPHA by Pavel Denim. $\Phi = 0.0329$

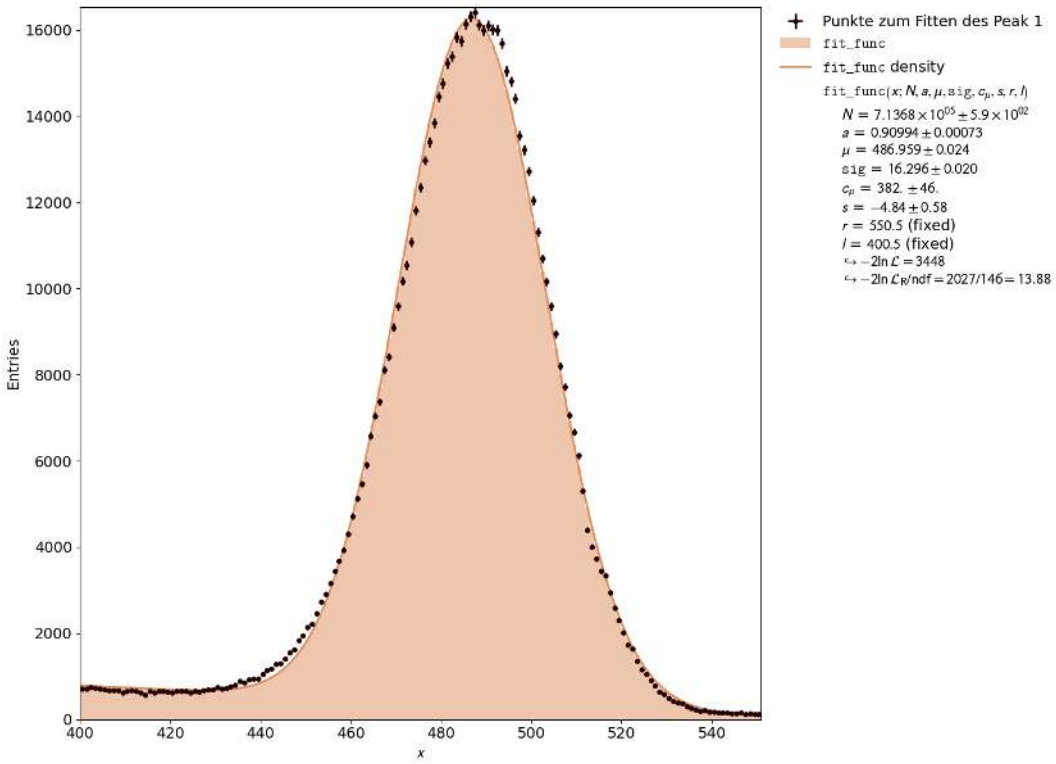

Figure A.6: Analysis of the Cs137 662keV photopeak at a detector voltage of 679 V, recorded with the Cassy Lab2 and internal amplification factor 5.52. $\Phi = 0.0335$

Co60

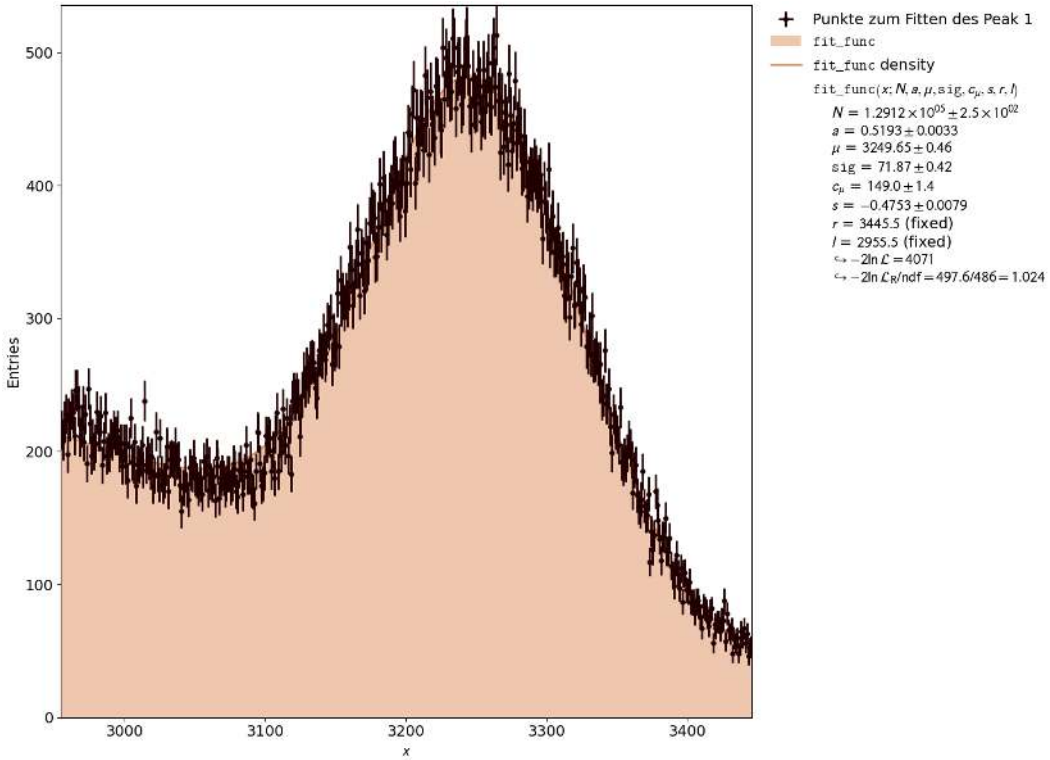

Figure A.7: Analysis of the Co60 1173 keV photopeak at a detector voltage of 679 V, recorded with the MCPHA by Pavel Denim. $\Phi = 0.0221$

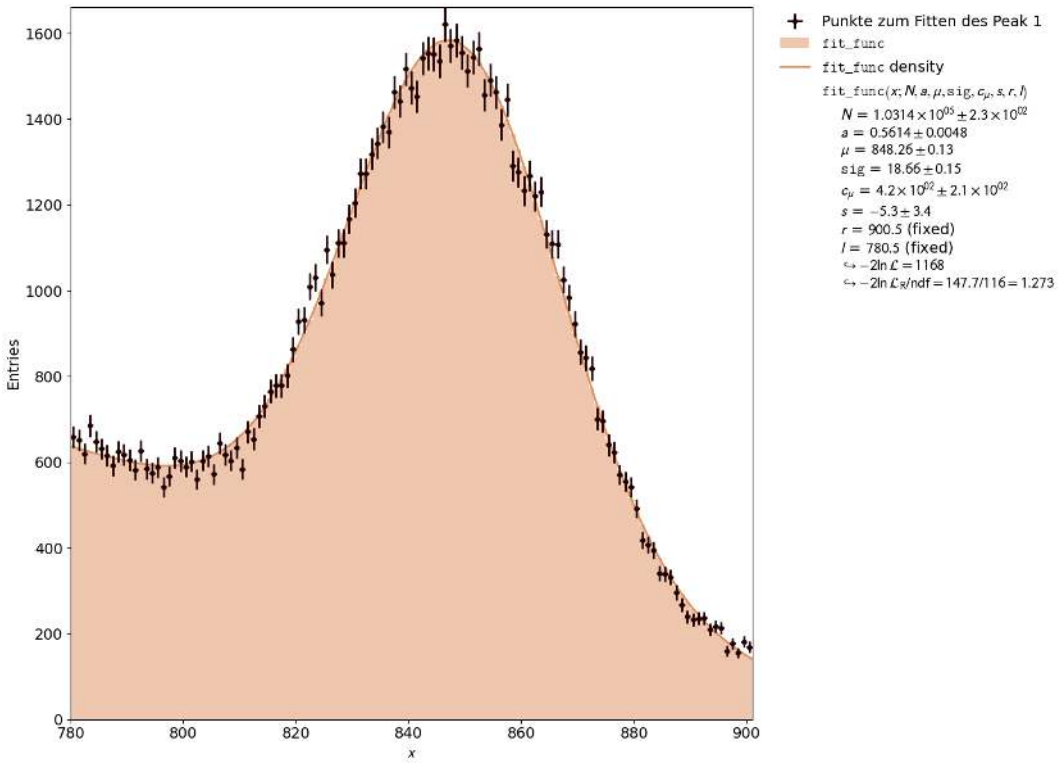

Figure A.8: Analysis of the Co60 1173 keV photopeak at a detector voltage of 679 V, recorded with the Cassy Lab2 and internal amplification factor 5.52. $\Phi = 0.0220$

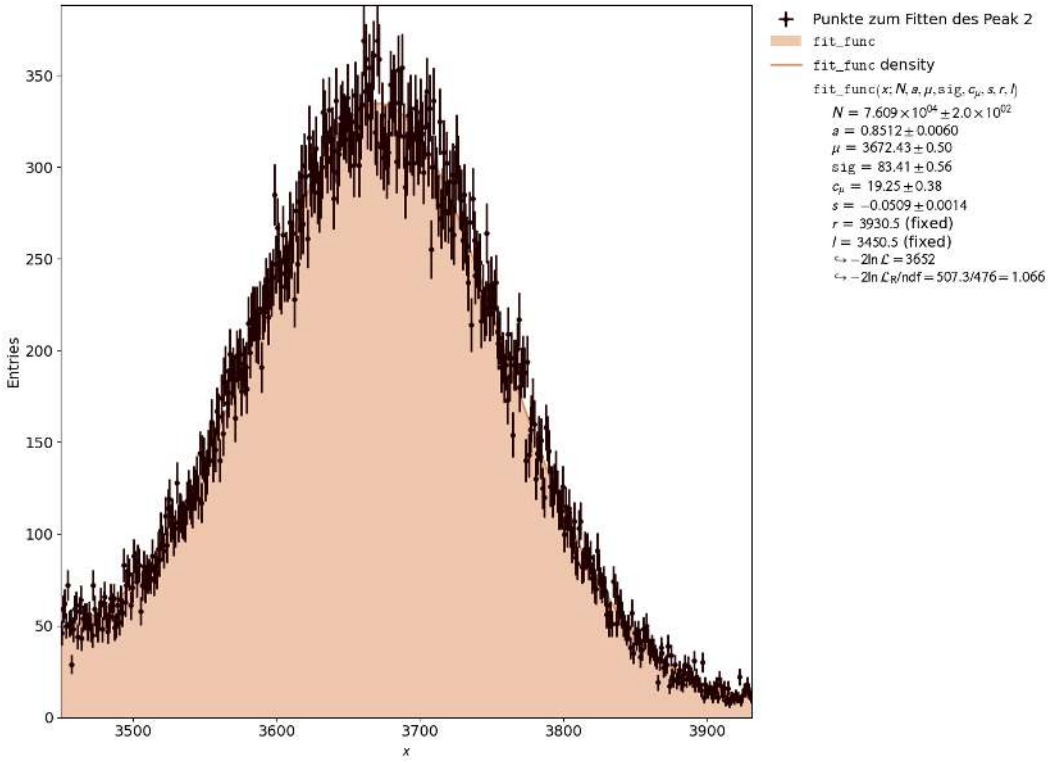

Figure A.9: Analysis of the Co60 1332 keV photopeak at a detector voltage of 679 V, recorded with the MCPHA by Pavel Denim. $\Phi = 0.0227$

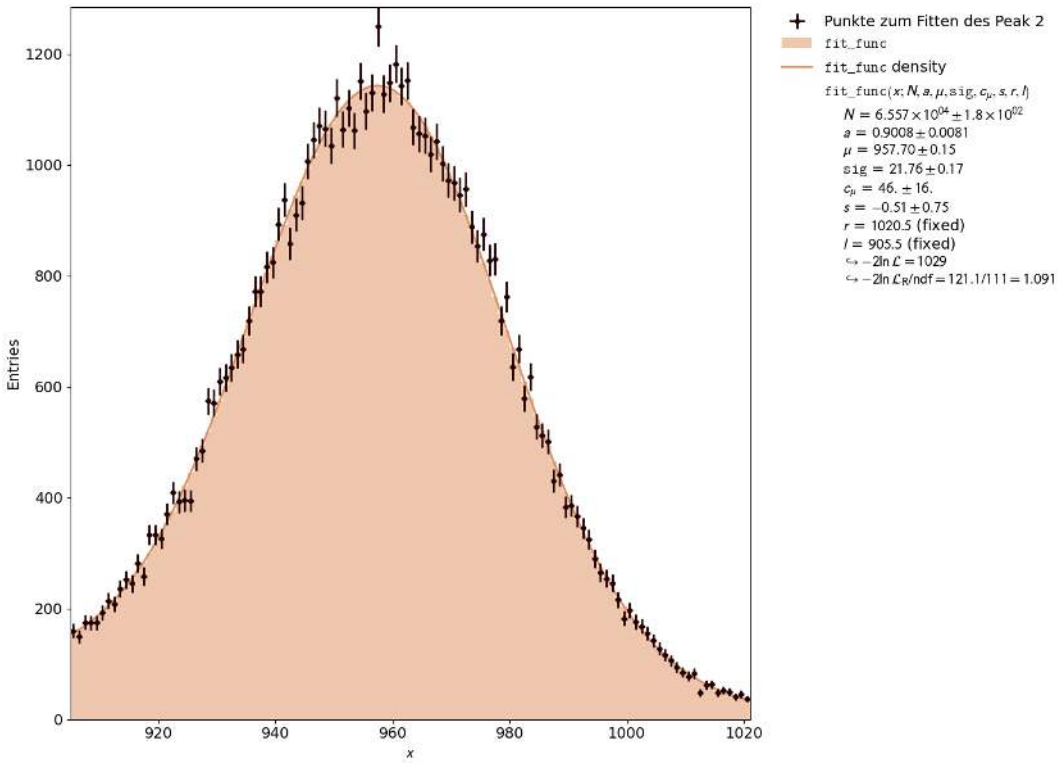

Figure A.10: Analysis of the Co60 1332 keV photopeak at a detector voltage of 679 V, recorded with the Cassy Lab2 and internal amplification factor 5.52. $\Phi = 0.0227$

Ra226

The second peak appearing in the Ra226 spectrum represents a superposition of K_α-conversion lines, which can lie in the range of 74.8-83.8 keV (according to [Zie10b]). According to Leybold didactic [Did], these are probably the lines of Bi-214 at 77.1 keV and Po-214 at 79.3 keV. For the energy calibration, the value of Po-214 at 79.3 keV is used, as this also represents the mean value of the data from Eckert & Ziegler. An energy calibration without the two first peaks of the Ra226 spectrum provides the result shown in the following figure A.11. However, since the data points in the range of low γ-energies < 150 keV are thereby missing, these two peaks are still considered for the energy calibration.

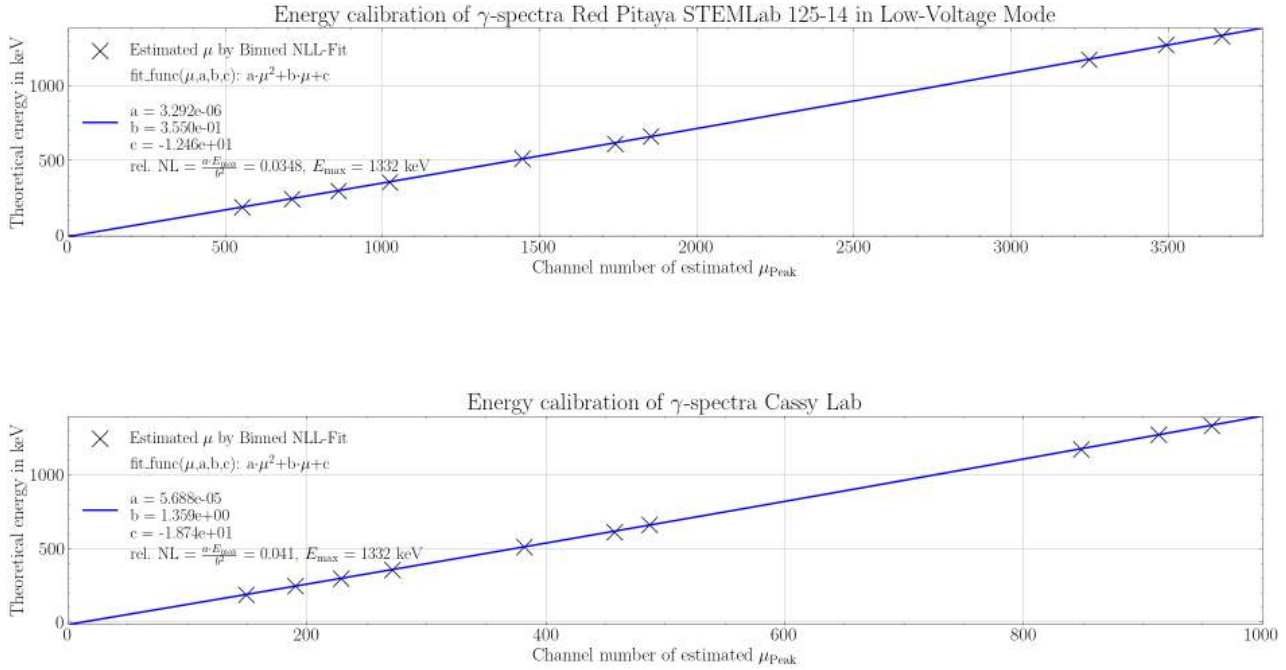

Figure A.11: Energy calibration of MCPHA and Cassy in a direct comparison, without the 79.3 keV and 53 keV Peak of the Ra226 γ-spectrum

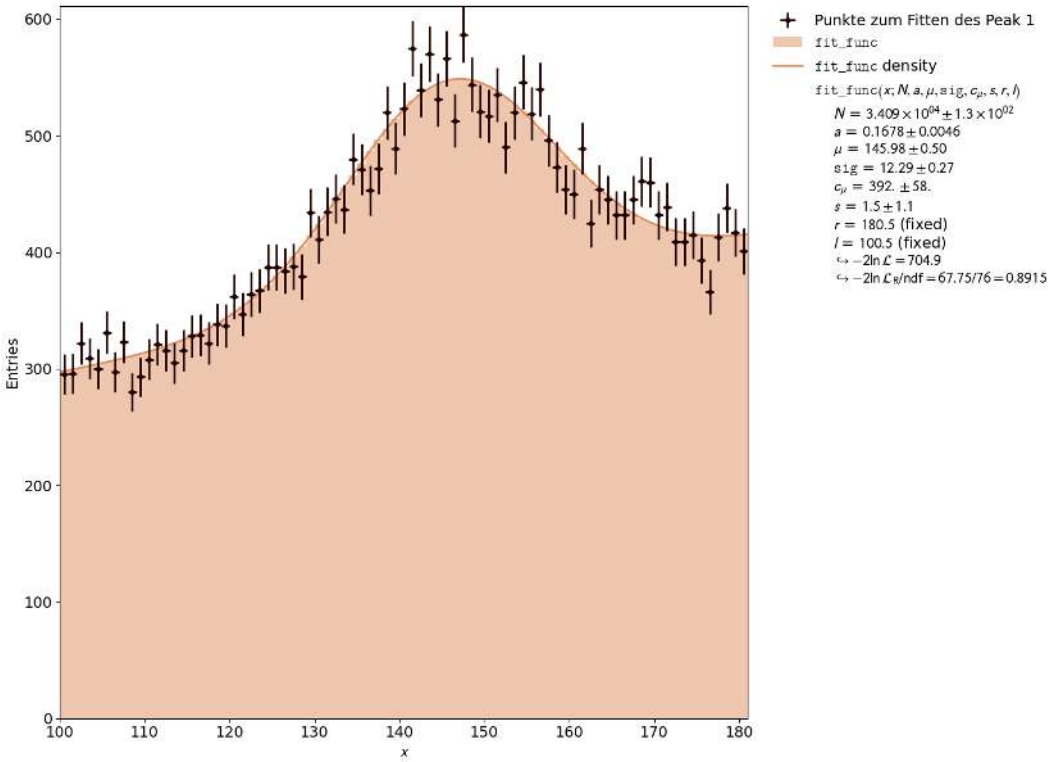

Figure A.12: Analysis of the Ra226 53 keV photopeak at a detector voltage of 679 V, recorded with the MCPHA by Pavel Denim. $\Phi = 0.0842$

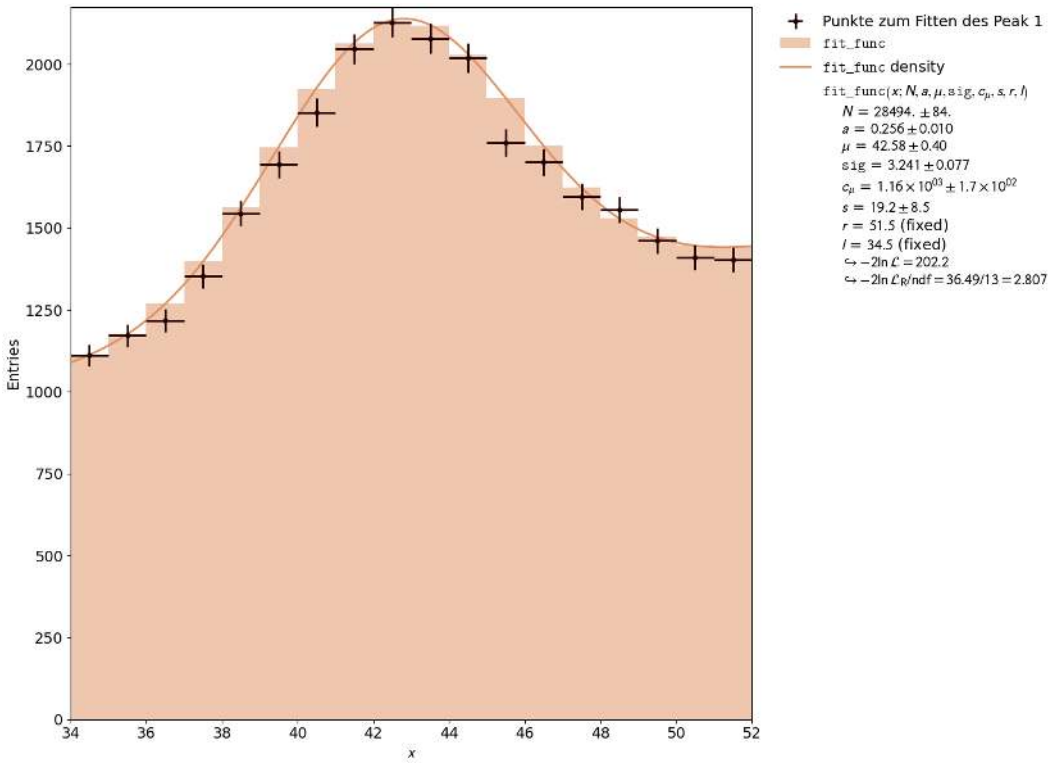

Figure A.13: Analysis of the Ra226 53 keV photopeak at a detector voltage of 679 V, recorded with the Cassy Lab2 and internal amplification factor 5.52. $\Phi = 0.0761$

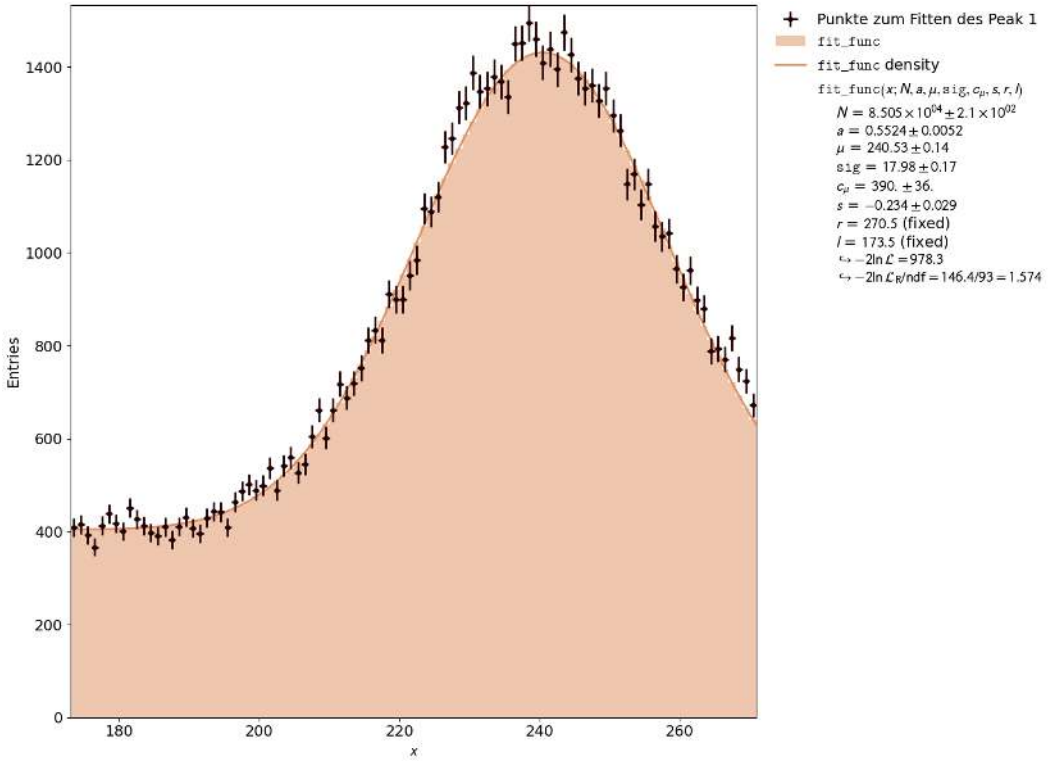

Figure A.14: Analysis of the Ra226 79.3 keV peak at a detector voltage of 679 V, recorded with the MCPHA by Pavel Denim. $\Phi = 0.0748$

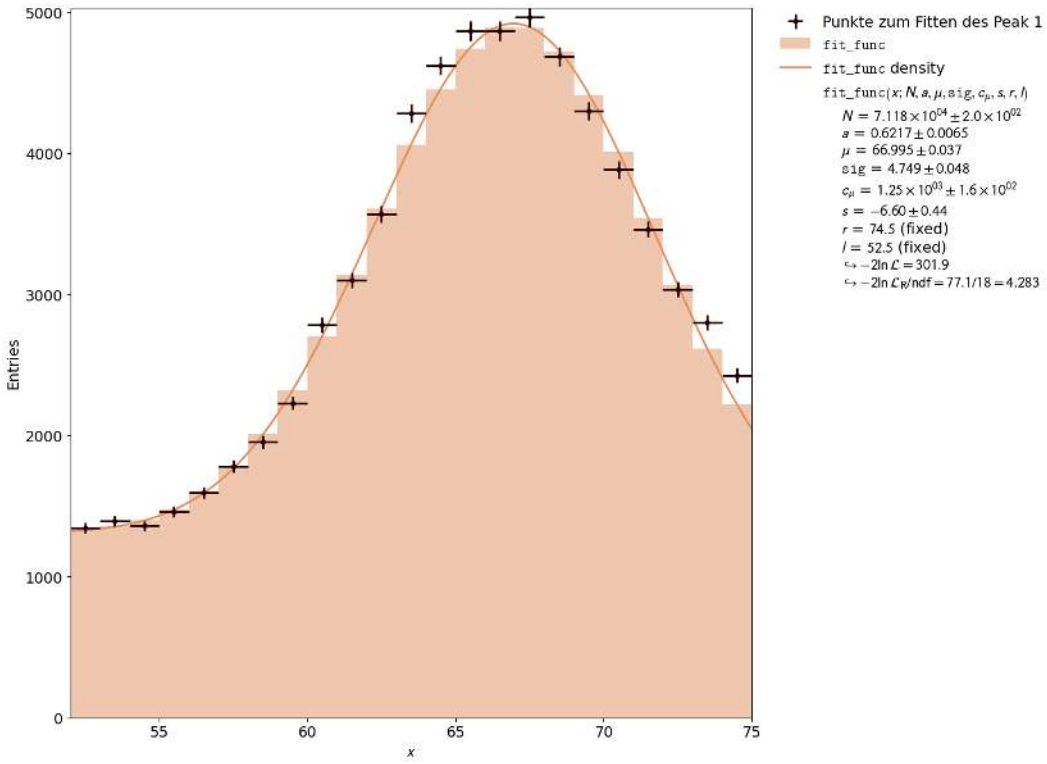

Figure A.15: Analysis of the Ra226 79.3 keV peak at a detector voltage of 679 V, recorded with the Cassy Lab2 and internal amplification factor 5.52. $\Phi = 0.0709$

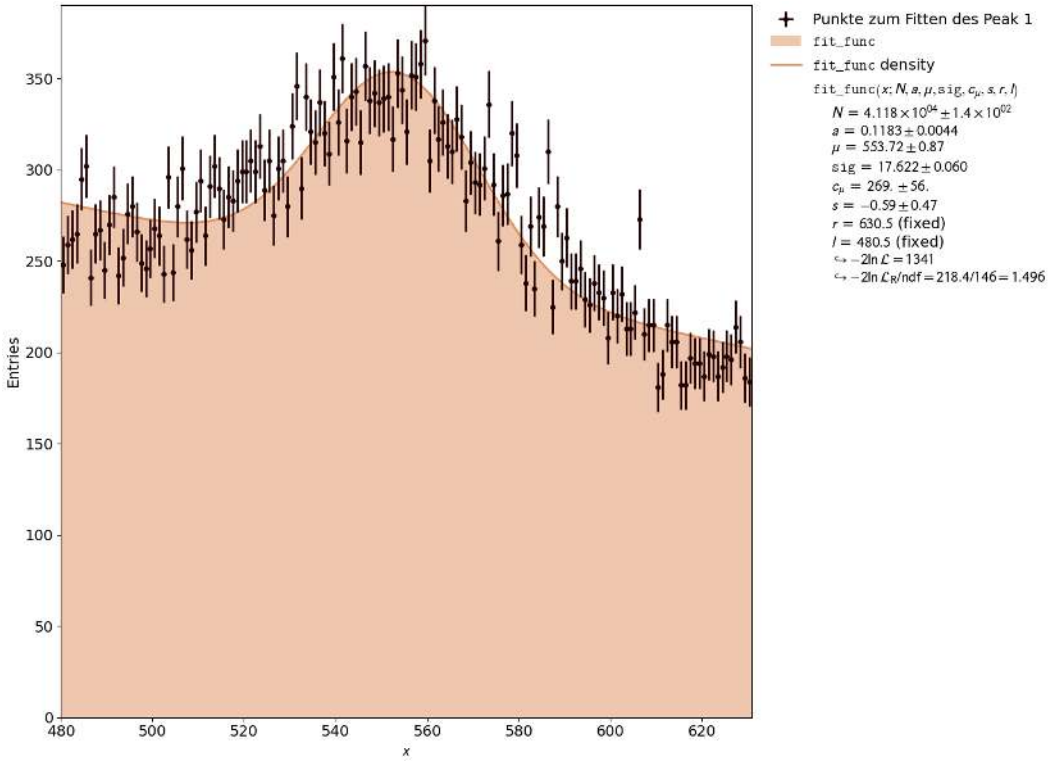

Figure A.16: Analysis of the Ra226 186 keV photopeak at a detector voltage of 679 V, recorded with the MCPHA by Pavel Denim. $\Phi = 0.0318$

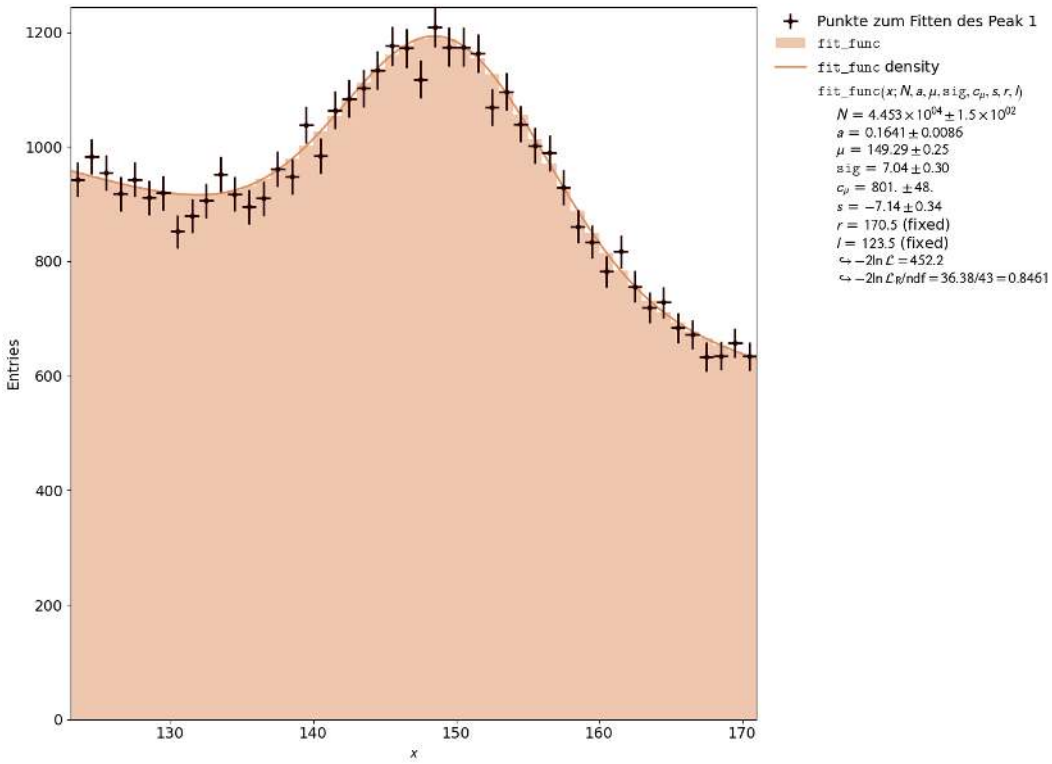

Figure A.17: Analysis of the Ra226 186 keV photopeak at a detector voltage of 679 V, recorded with the Cassy Lab2 and internal amplification factor 5.52. $\Phi = 0.0471$

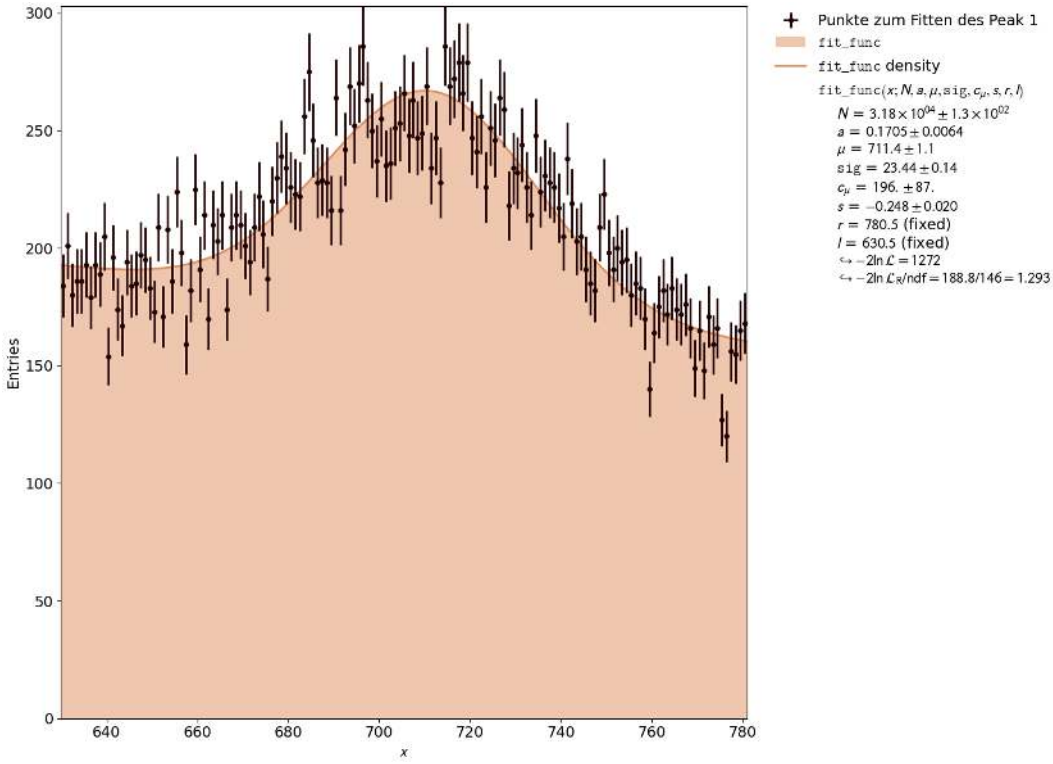

Figure A.18: Analysis of the Ra226 242 keV photopeak at a detector voltage of 679 V, recorded with the MCPHA by Pavel Denim. $\Phi = 0.0329$

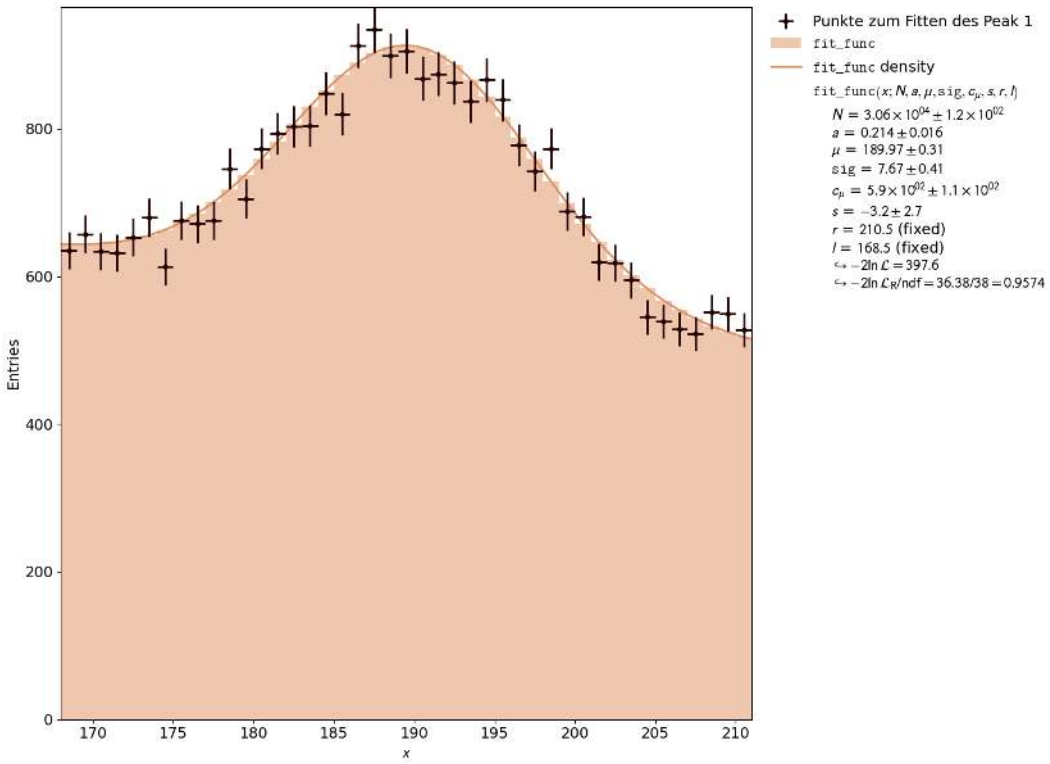

Figure A.19: Analysis of the Ra226 242 keV photopeak at a detector voltage of 679 V, recorded with the Cassy Lab2 and internal amplification factor 5.52. $\Phi = 0.0404$

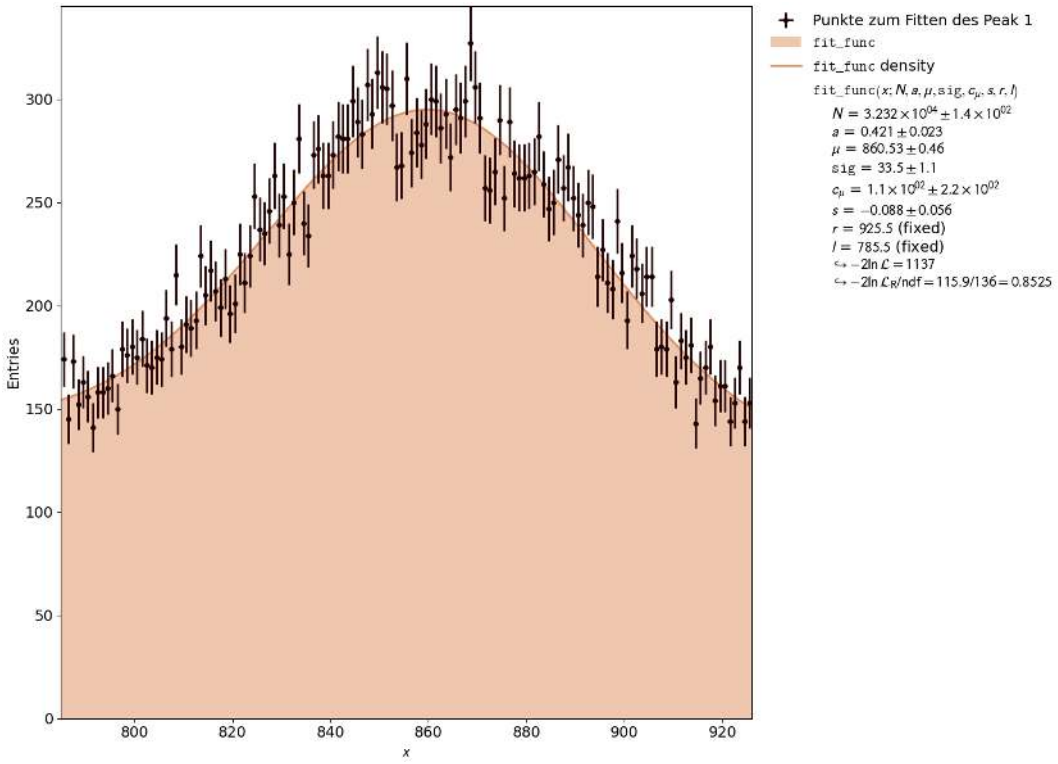

Figure A.20: Analysis of the Ra226 295 keV photopeak at a detector voltage of 679 V, recorded with the MCPHA by Pavel Denim. $\Phi = 0.0389$

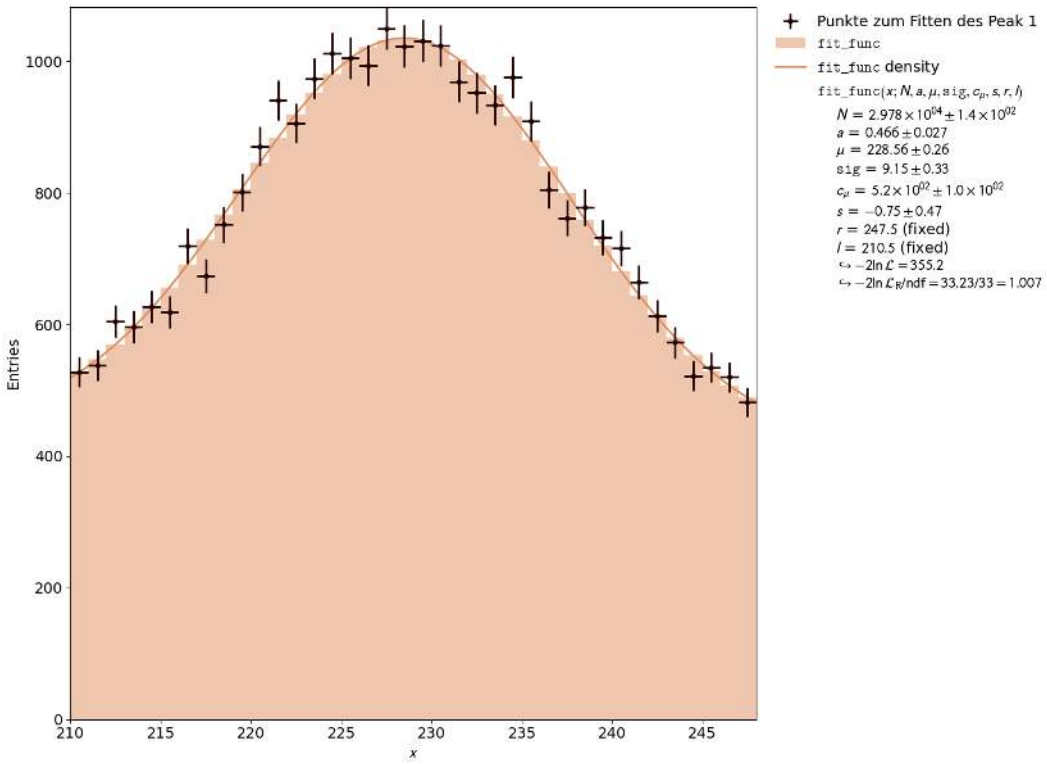

Figure A.21: Analysis of the Ra226 295 keV photopeak at a detector voltage of 679 V, recorded with the Cassy Lab2 and internal amplification factor 5.52. $\Phi = 0.0400$

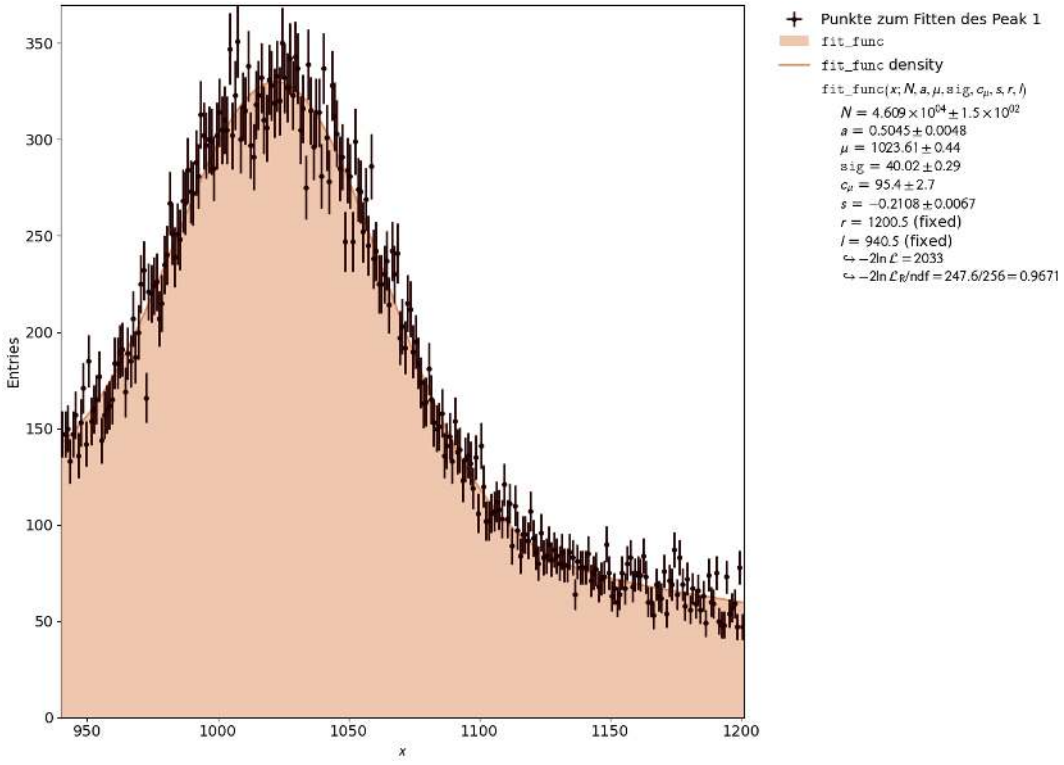

Figure A.22: Analysis of the Ra226 352 keV photopeak at a detector voltage of 679 V, recorded with the MCPHA by Pavel Denim. $\Phi = 0.0391$

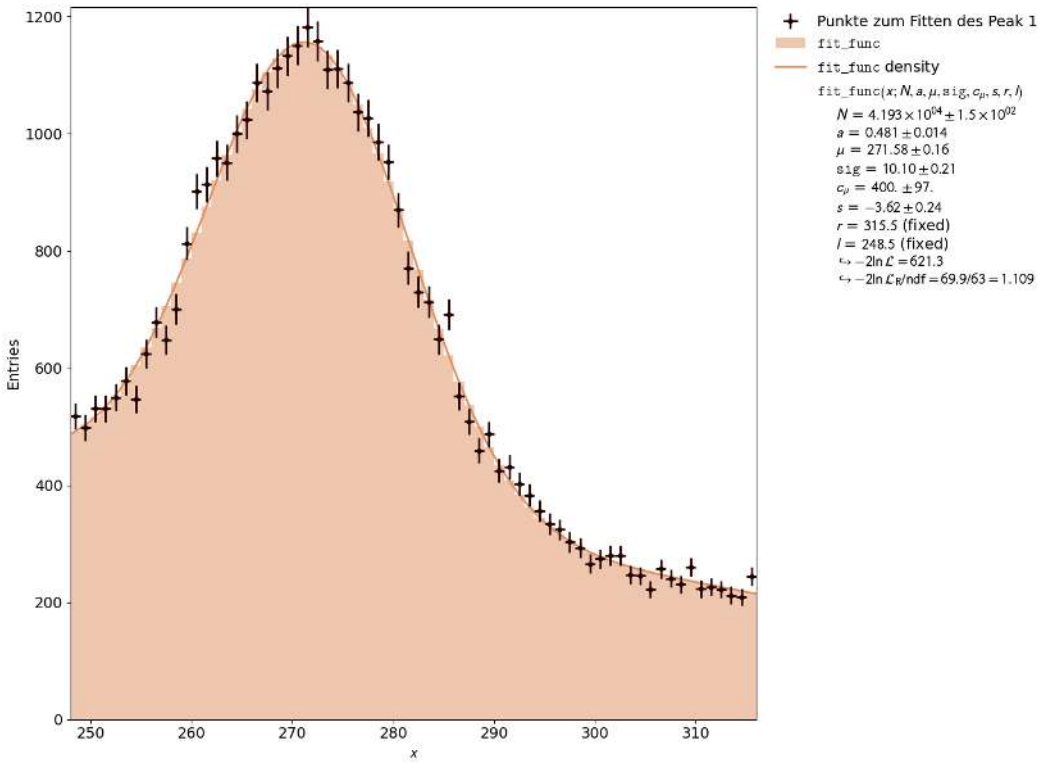

Figure A.23: Analysis of the Ra226 352 keV photopeak at a detector voltage of 679 V, recorded with the Cassy Lab2 and internal amplification factor 5.52. $\Phi = 0.0372$

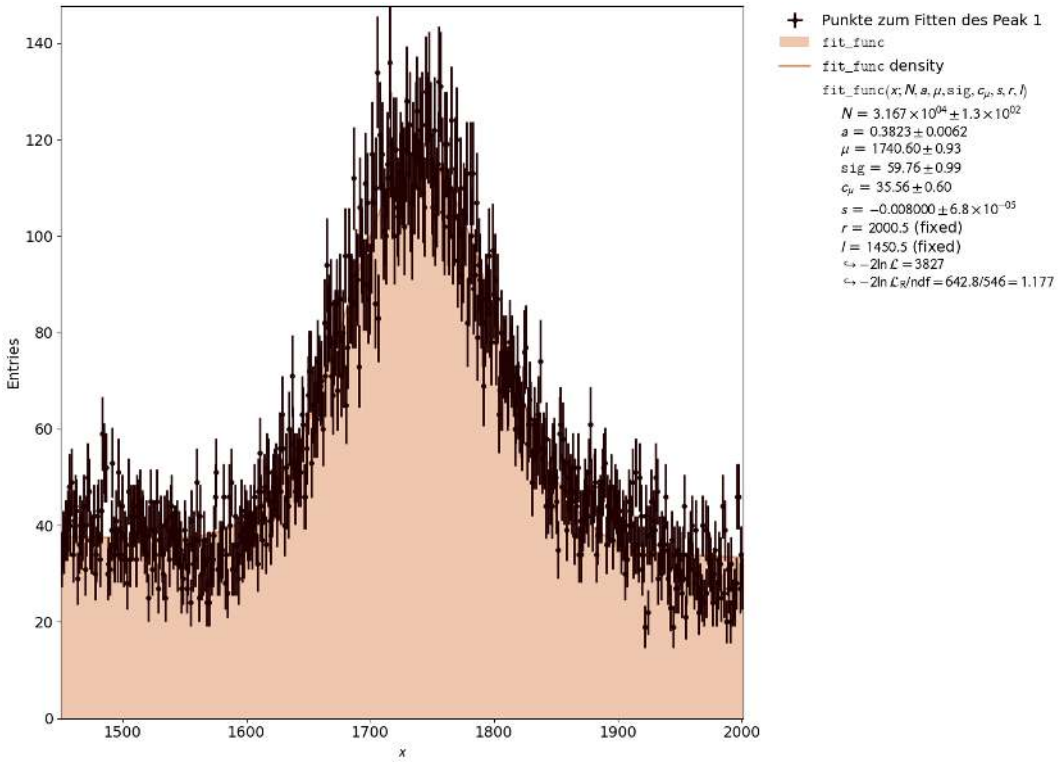

Figure A.24: Analysis of the Ra226 609 keV photopeak at a detector voltage of 679 V, recorded with the MCPHA by Pavel Denim. $\Phi = 0.0343$

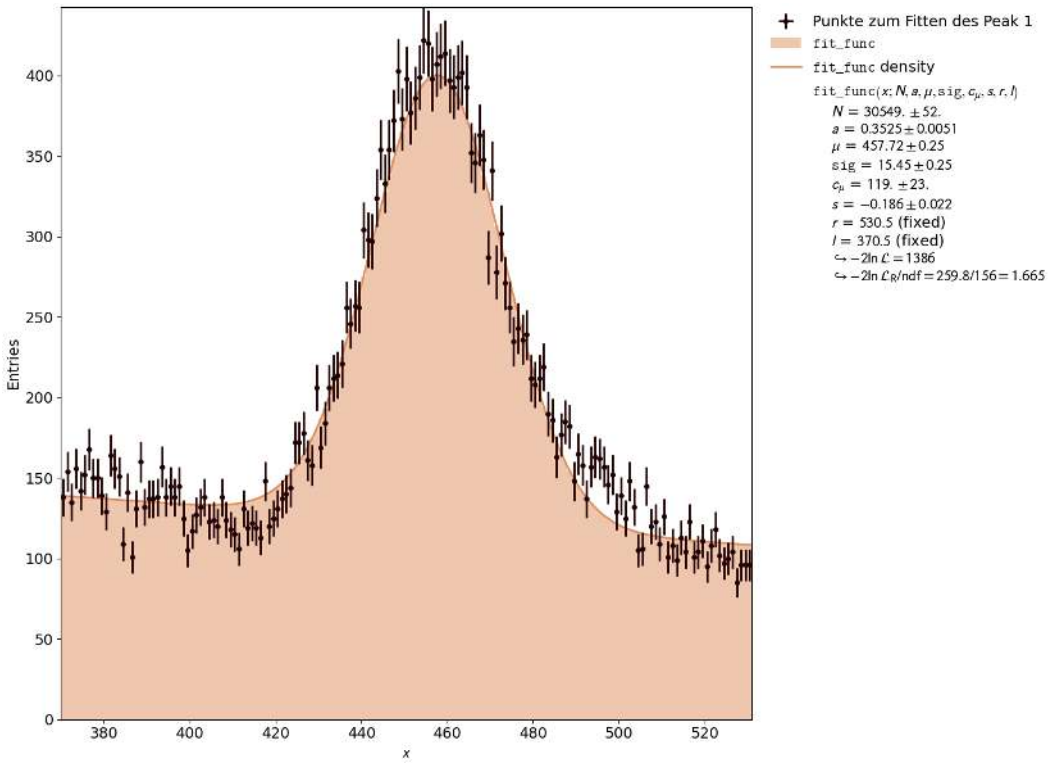

Figure A.25: Analysis of the Ra226 609 keV photopeak at a detector voltage of 679 V, recorded with the Cassy Lab2 and internal amplification factor 5.52. $\Phi = 0.0338$

A.3.1.2 Comparison of Relative Energy Resolution Φ

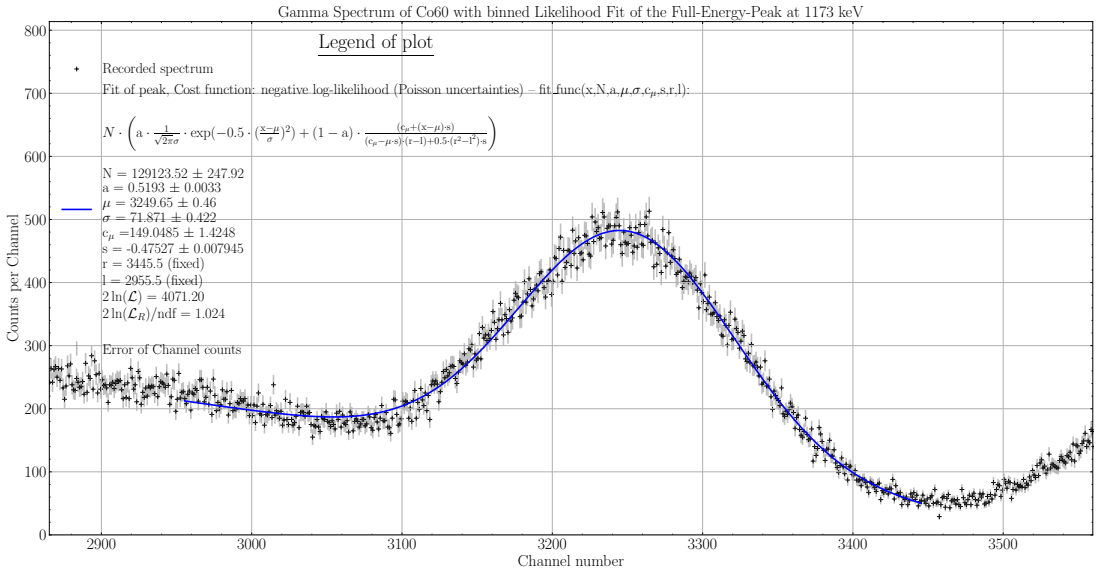

Figure A.26: Analysis of the Co60 1173 keV photopeak at a detector voltage of 679 V, recorded with the MCPHA by Pavel Denim. $\Phi = 0.0221$

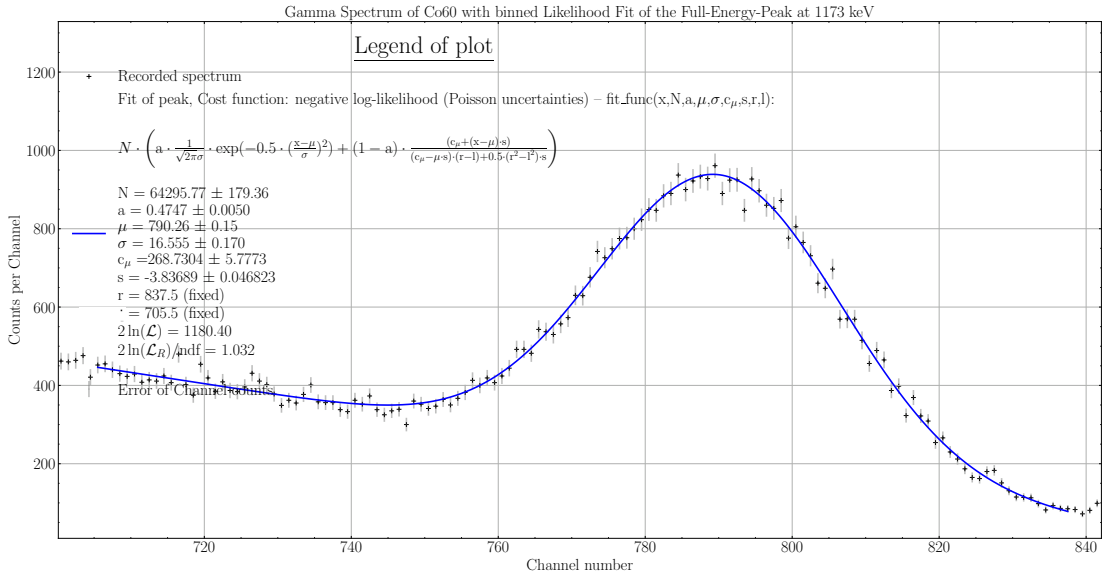

Figure A.27: Analysis of the Co60 1173 keV photopeak at a detector voltage of 821 V, recorded with the Cassy Lab2 and internal amplification factor 1. $\Phi = 0.0210$

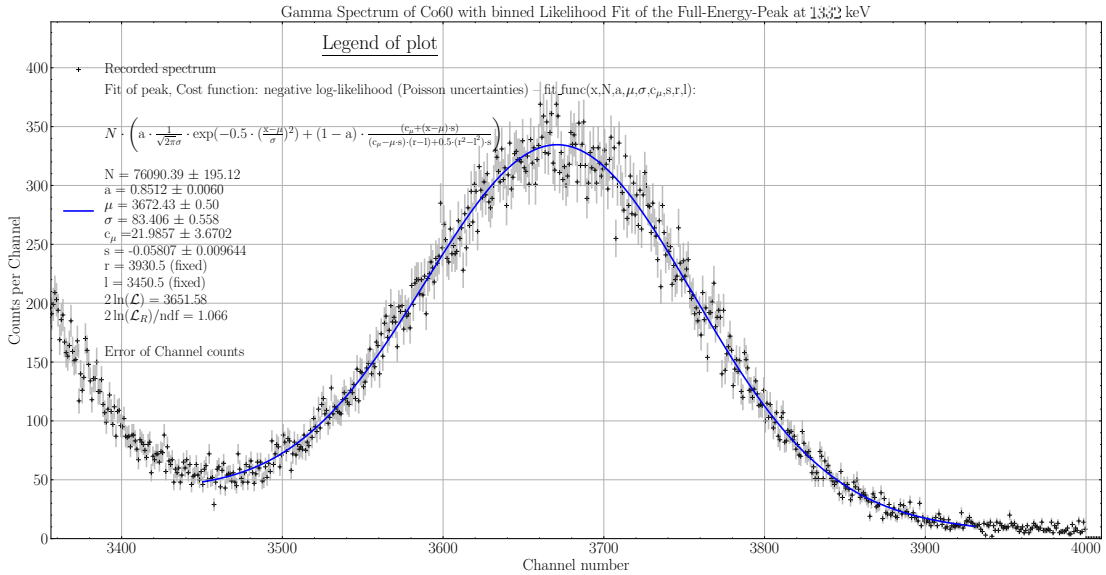

Figure A.28: Analysis of the Co60 1332 keV photopeak at a detector voltage of 679 V, recorded with the MCPHA by Pavel Denim. $\Phi = 0.0227$

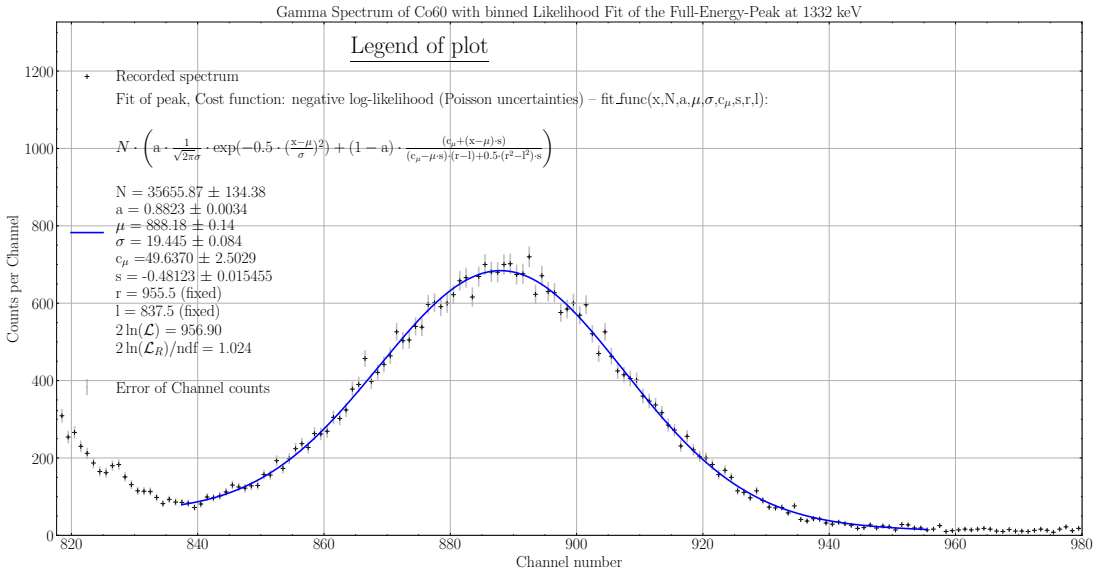

Figure A.29: Analysis of the Co60 1332 keV photopeak at a detector voltage of 821 V, recorded with the Cassy Lab2 and internal amplification factor 1. $\Phi = 0.0219$

A.3.2 Chapter 5 - Comparison of Red Pitaya and the MCA-System by FAST ComTec

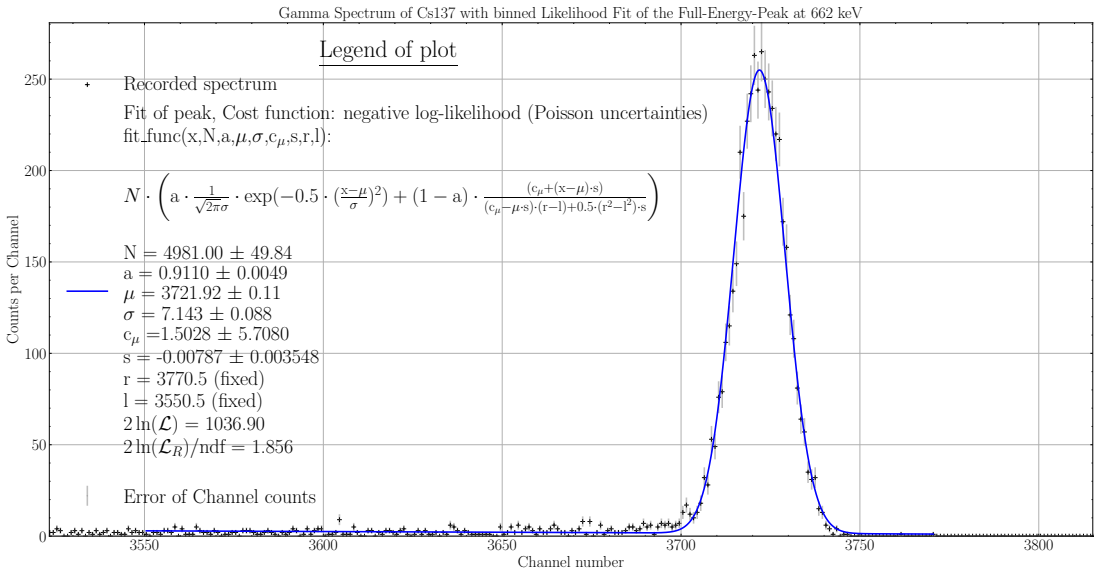

Figure A.30: Analysis of the Cs137 662 keV photopeak, recorded with the MCPHA by Pavel Denim, $\Phi = 0.00192$.

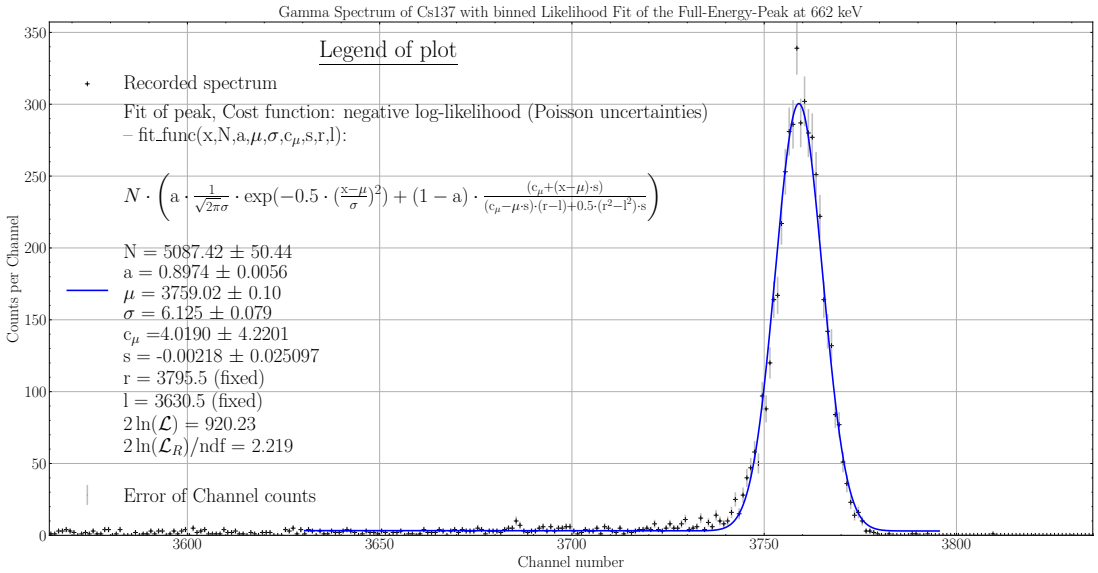

Figure A.31: Analysis of the Cs137 662 keV photopeak, recorded with MPANT by FAST ComTec, $\Phi = 0.00163$.

APPENDIX B

AUTO DC-CALIBRATION IN OS 2.00-30

The following tools are required to perform the Auto DC ADC and DAC Calibration in OS 2.00-30:

- Red Pitaya STEMlab 125-14 and Micro SD-card with OS 2.00-30
- Adjustable DC power supply, min. range 0-5 V
- 2 SMA-Cable
- Multimeter
- SMA T-splitter
- SMA Short-terminator

Note: Checking the voltage using a multimeter is essential to obtain calibration data that is as good as or better than the factory calibration

1. Start Auto DC Calibration application.

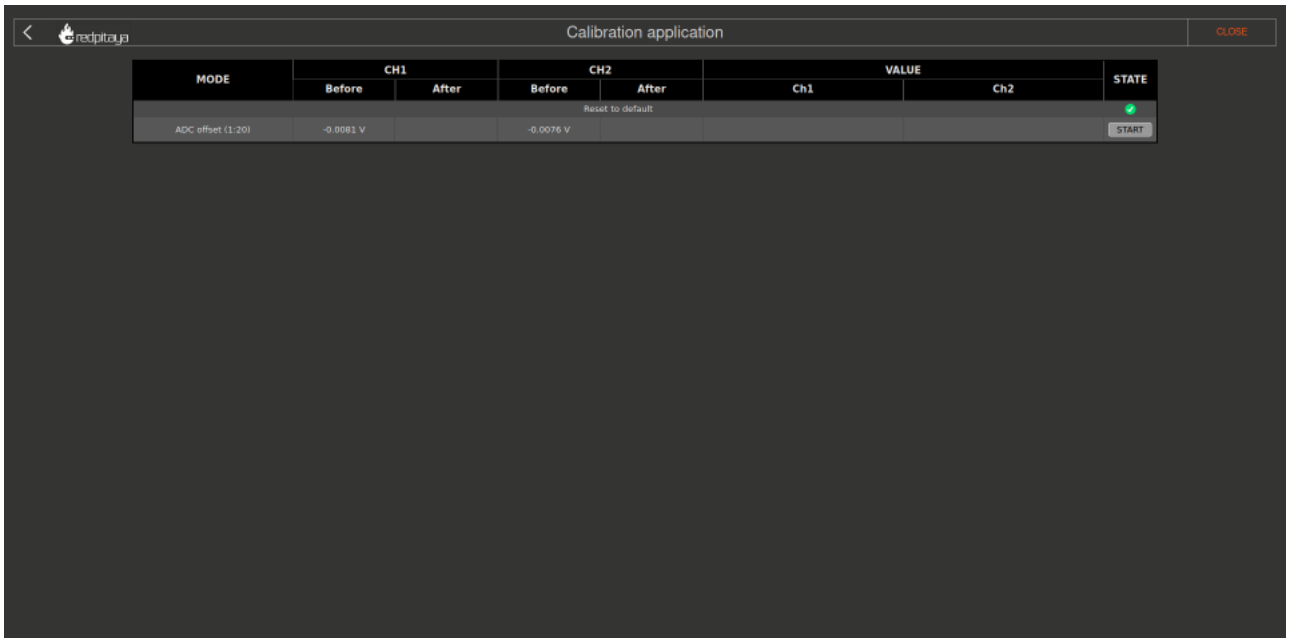

2. Switch Jumpers to HV Mode and connect IN1 and IN2 to GND (Connect both of them with the short termination by the T-Splitter).

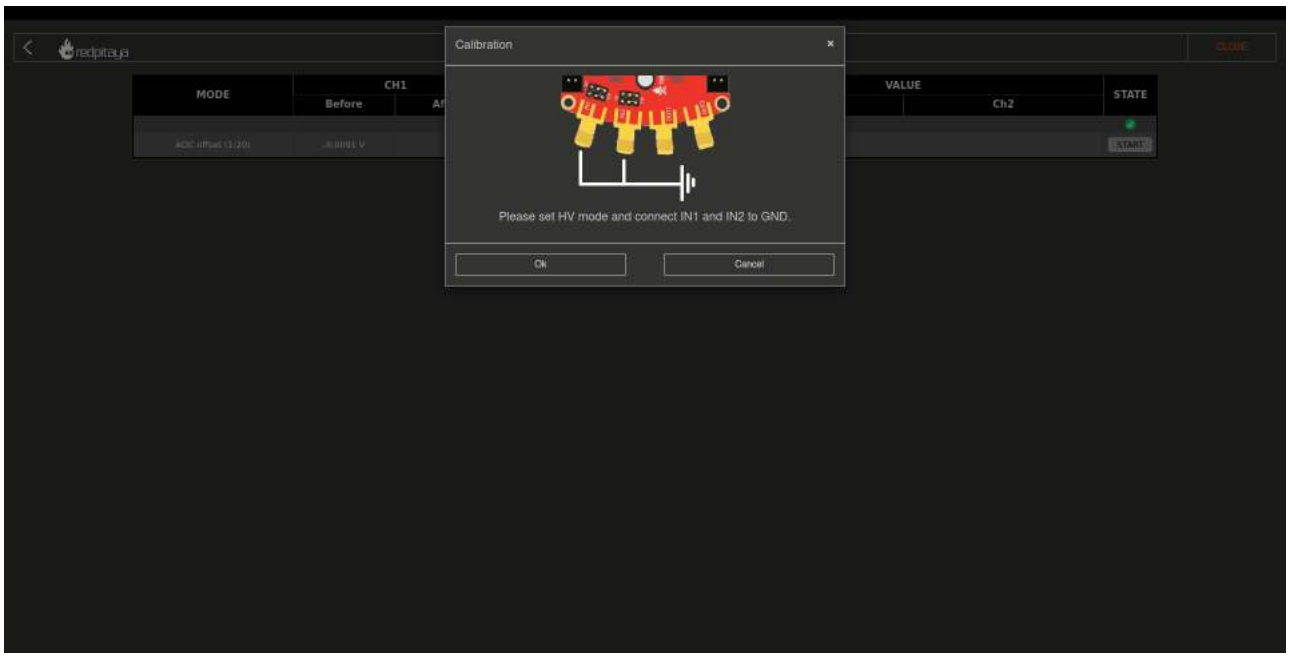
redpitaya
CLOSE
MODE
CH1
Before
VALUE
Ch2
STATE
START
Calibration
Please set HV mode and connect IN1 and IN2 to GND.
Ok
Cancel

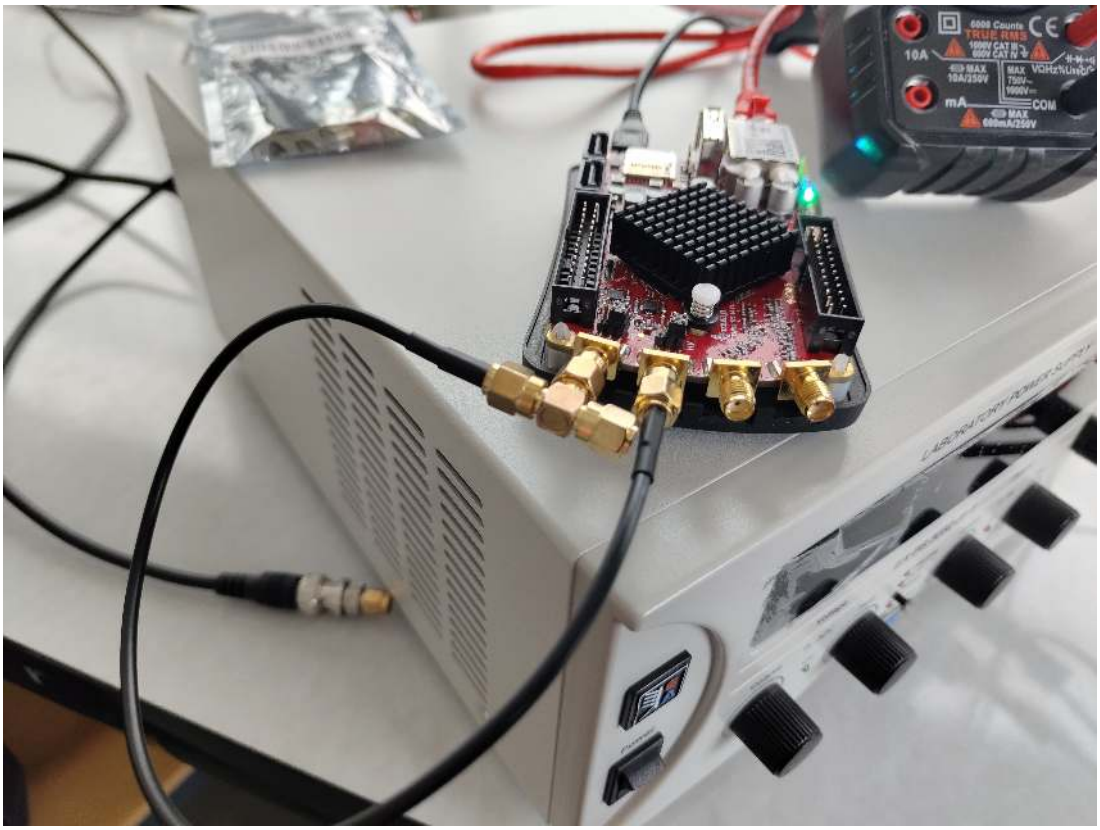
6000 Counts
TRUE RMS
10A
mA
COM

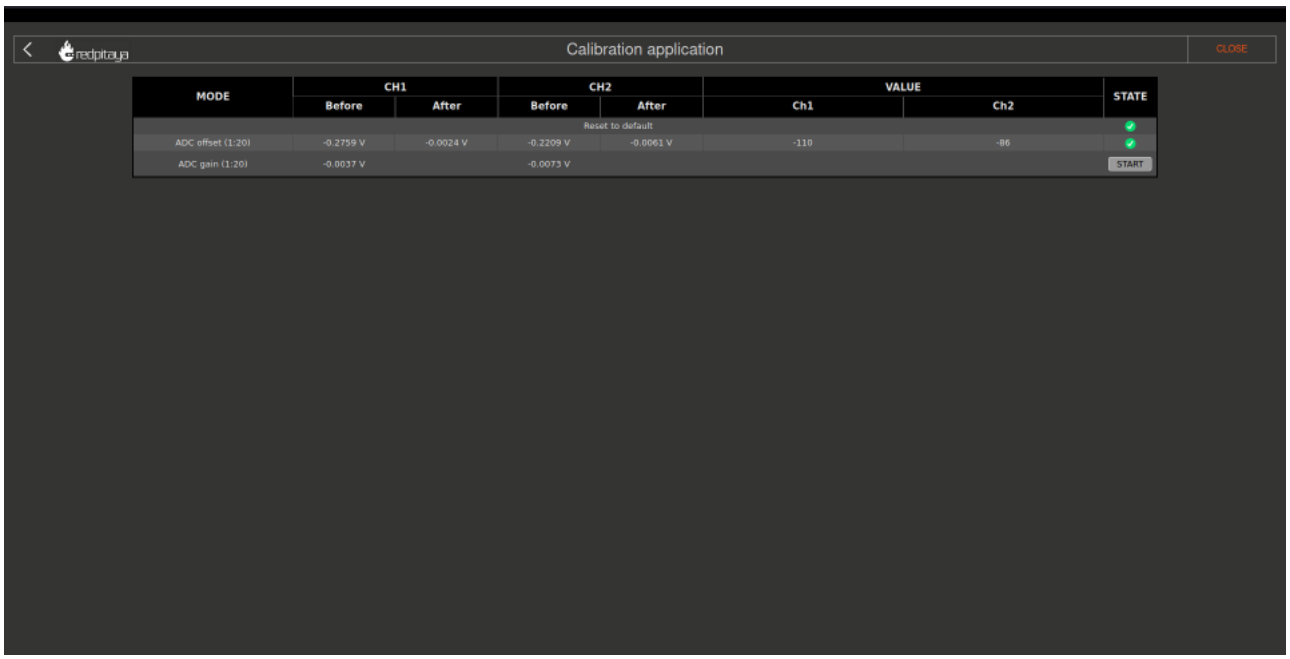

3. Connect IN1 and IN2 with DC Power Supply and and enter the voltage value close to 5V, checked with the multimeter.

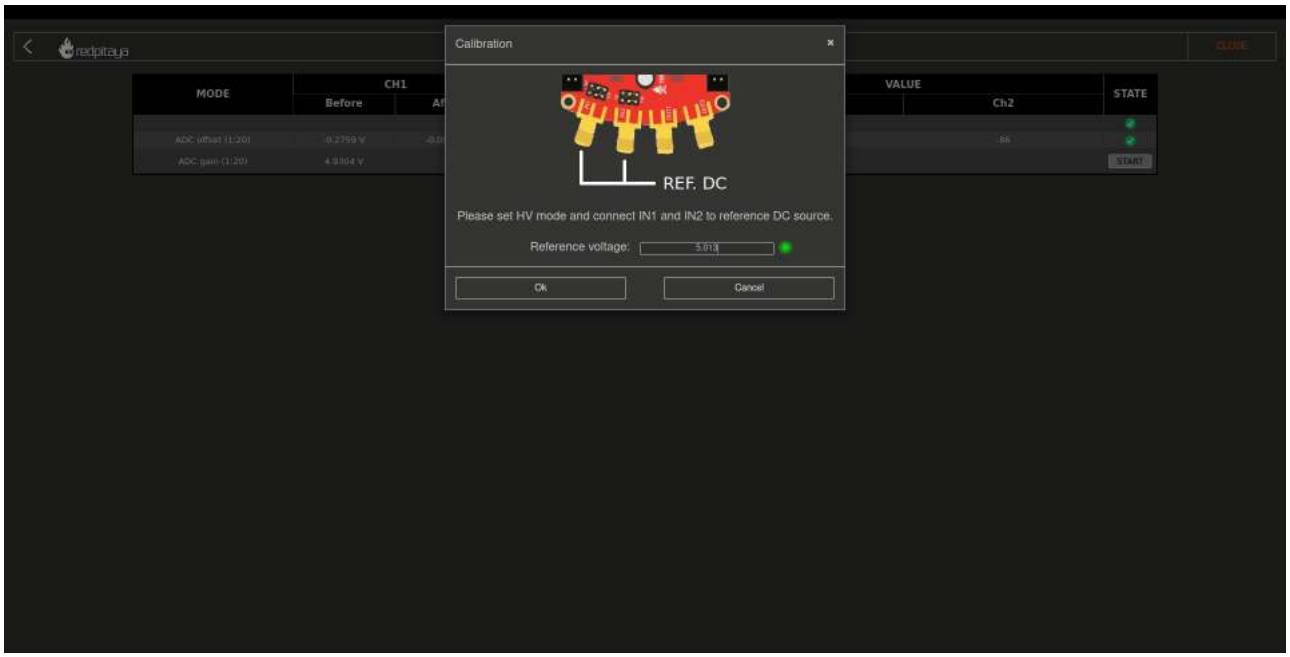

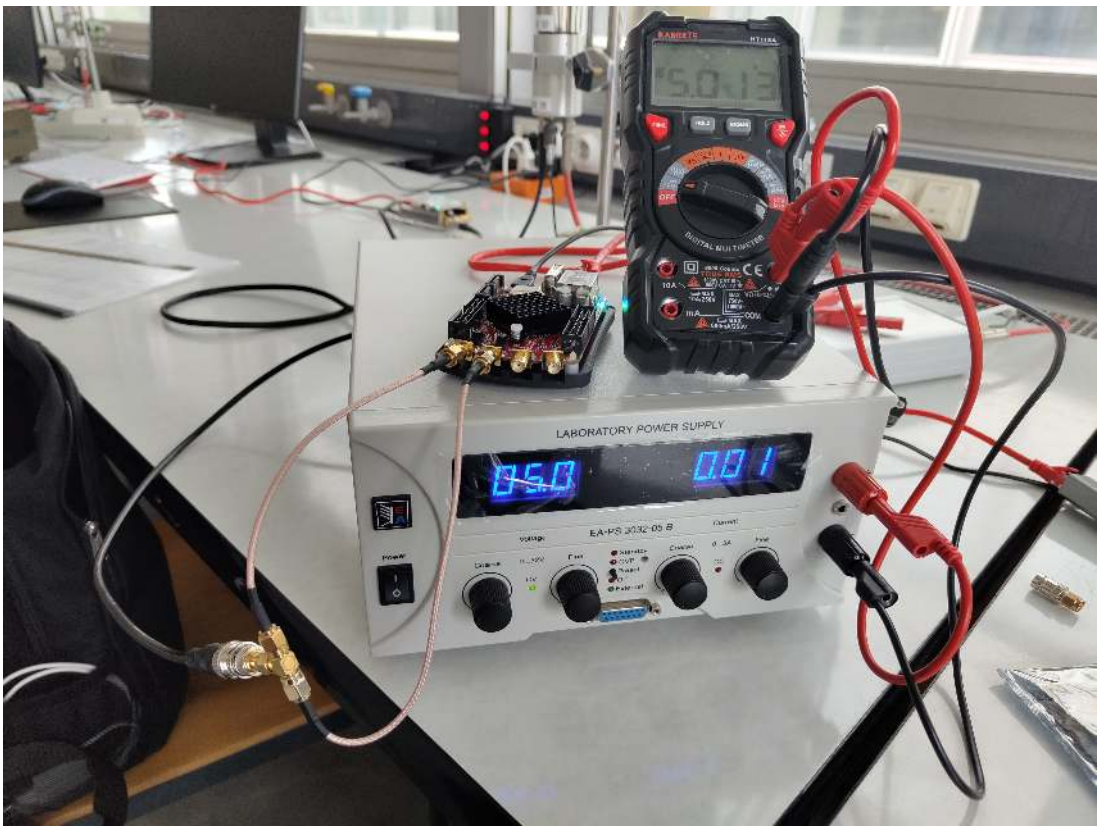

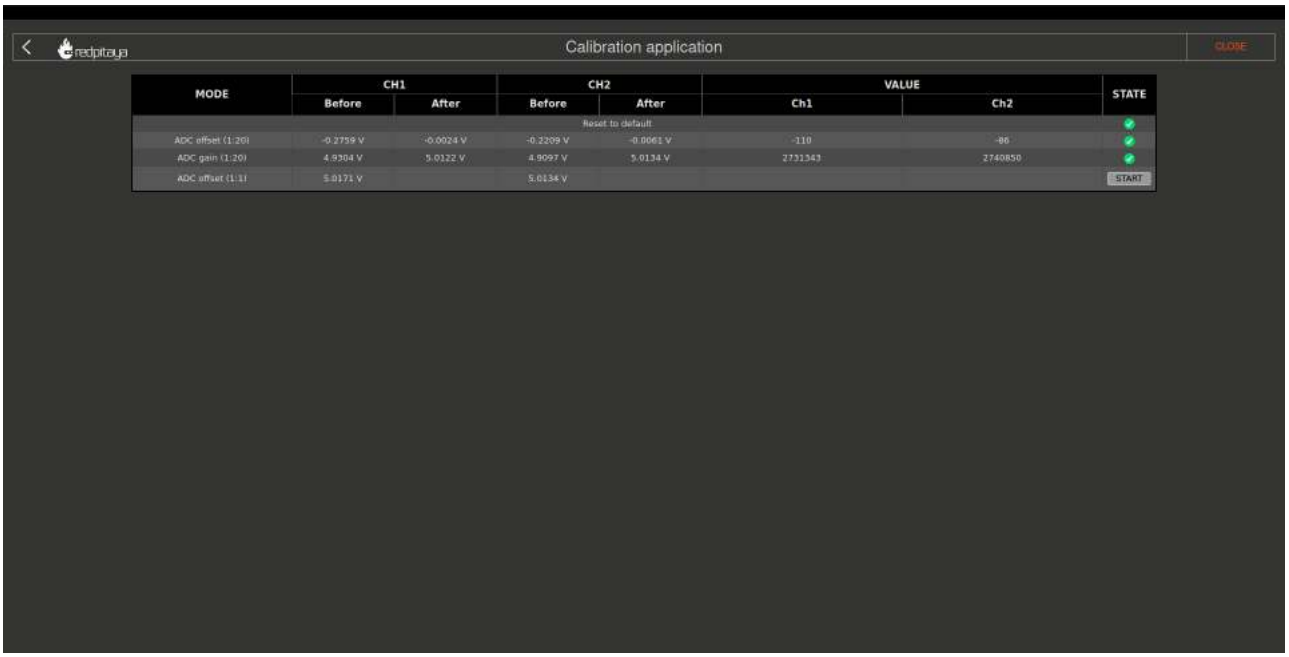

4. Switch Jumpers to LV Mode and connect IN1 and IN2 to GND (Connect both with the short termination by the T-Splitter).

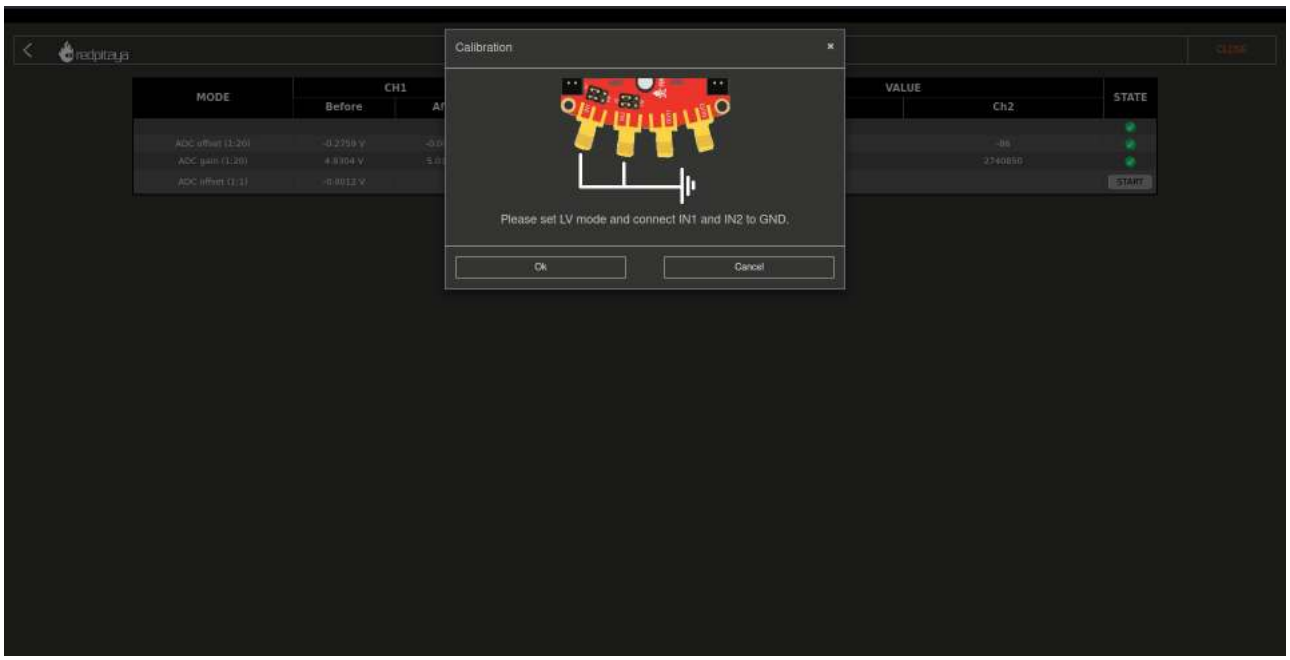
redpitaya
MODE
CH1
Before
VALUE
Ch2
STATE
START
Calibration
Please set LV mode and connect IN1 and IN2 to GND.
Ok
Cancel

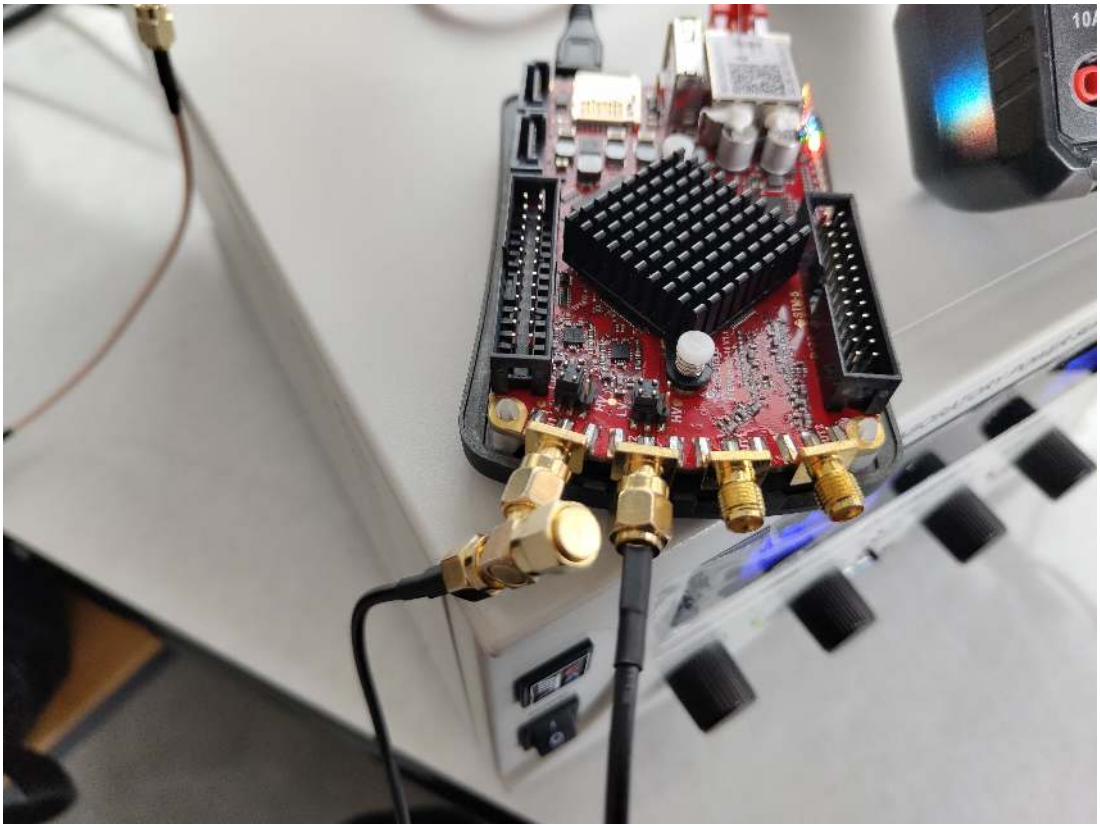

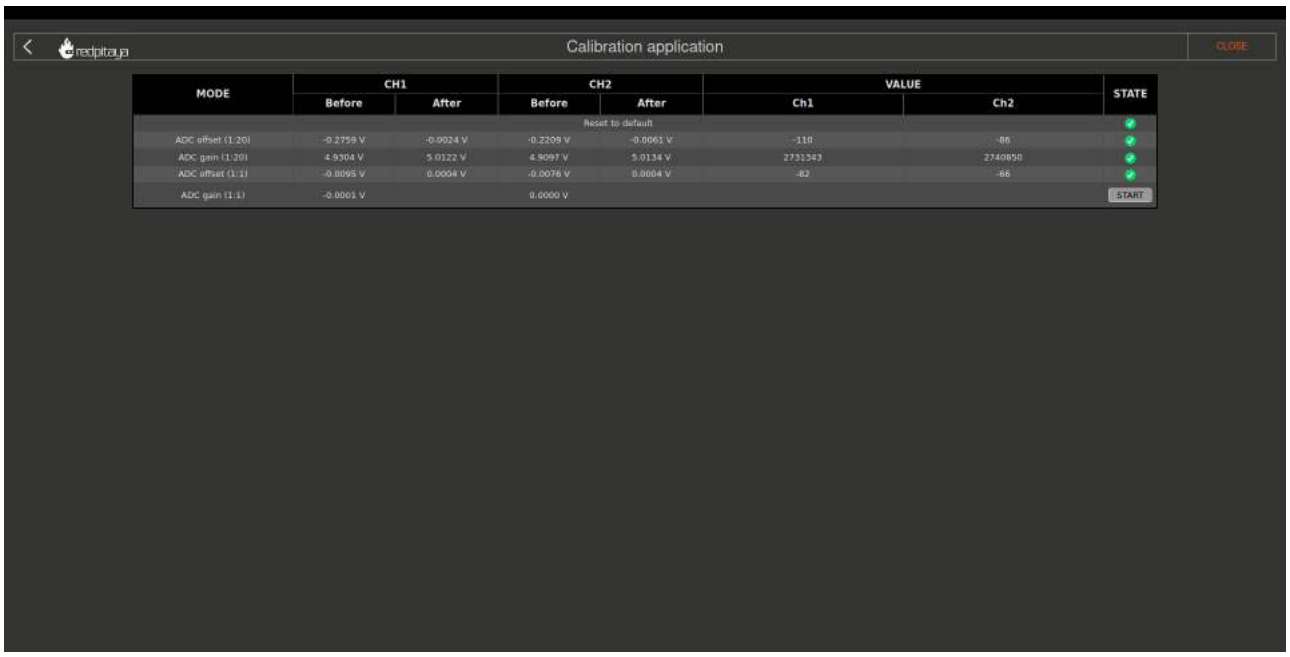

5. Connect IN1 and IN2 with DC Power Supply and enter the voltage value close to 500 mV, checked with the multimeter.

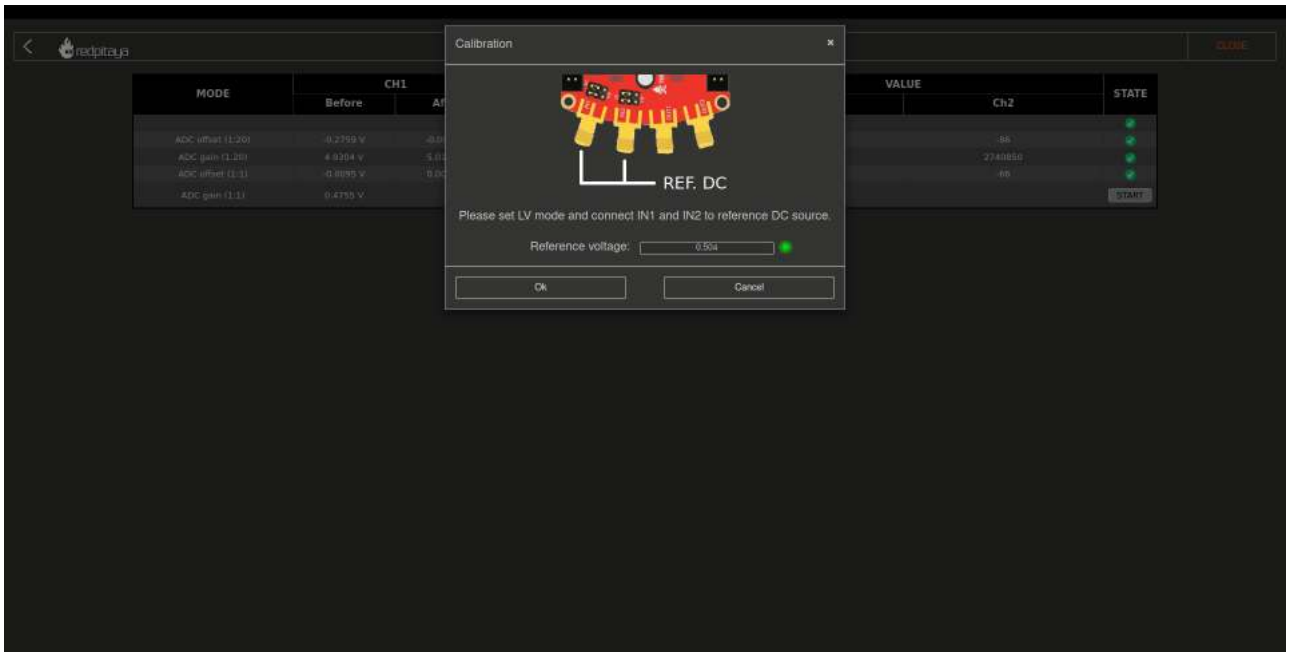

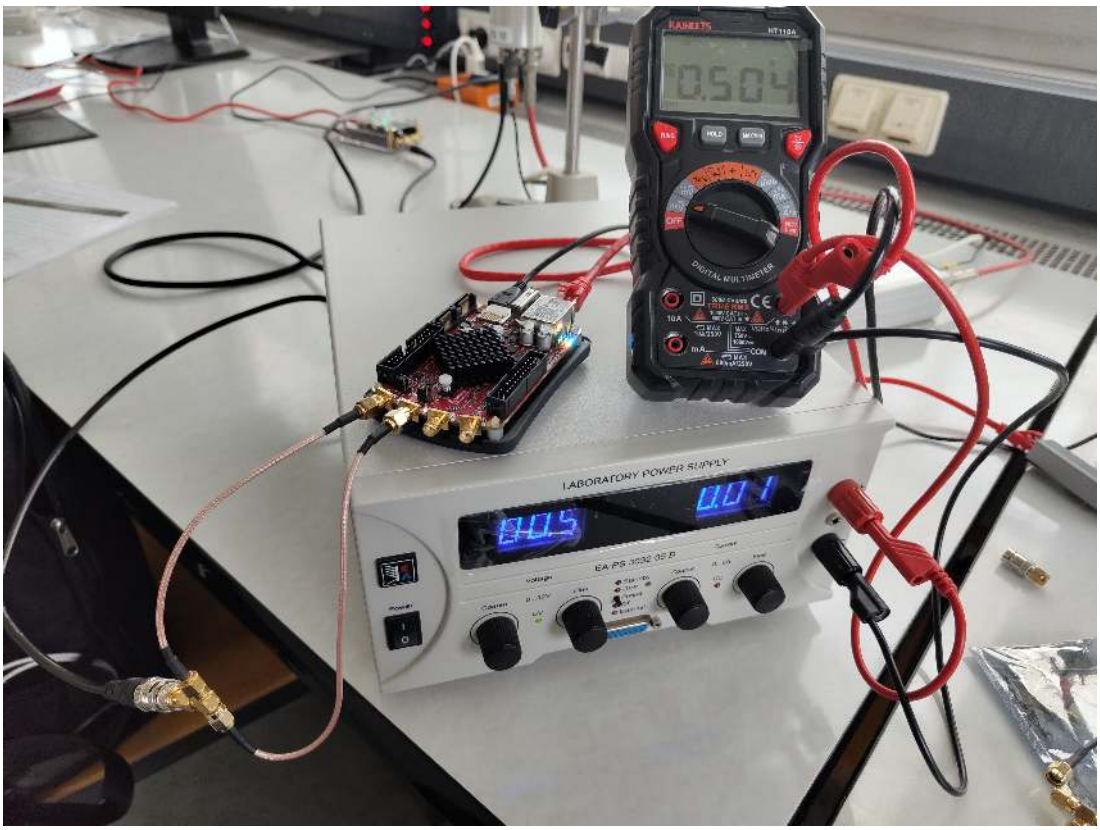

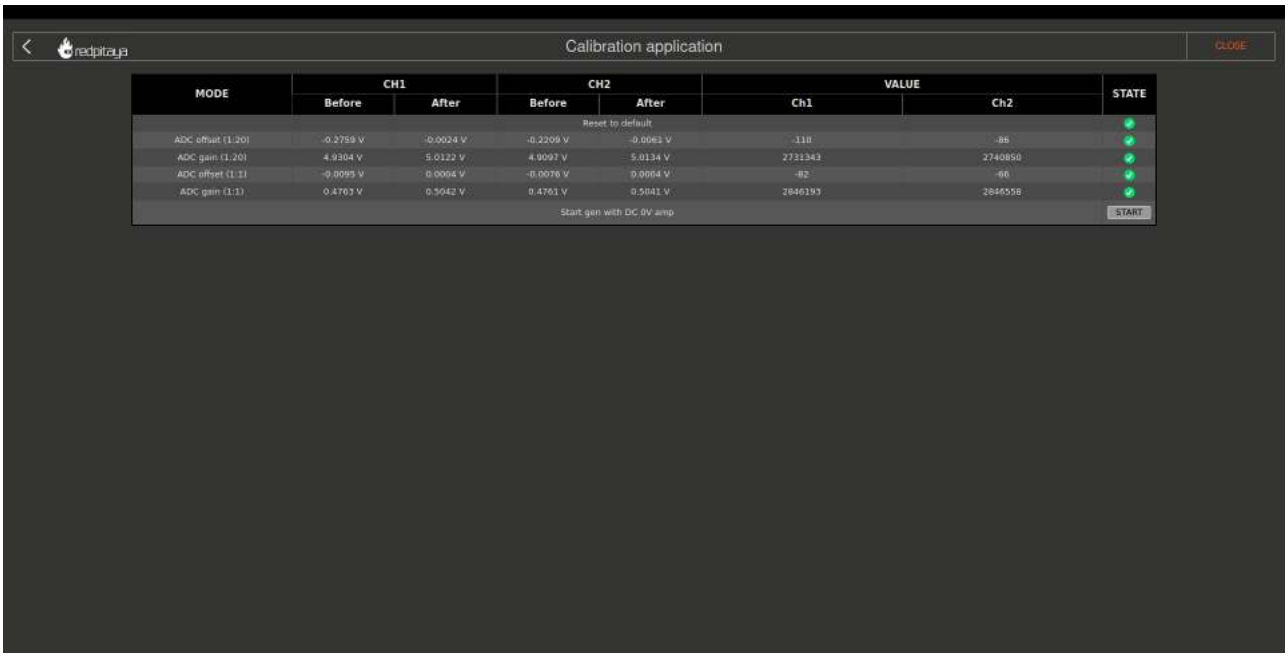

6. Connect IN1 to OUT1 and IN2 to Out2

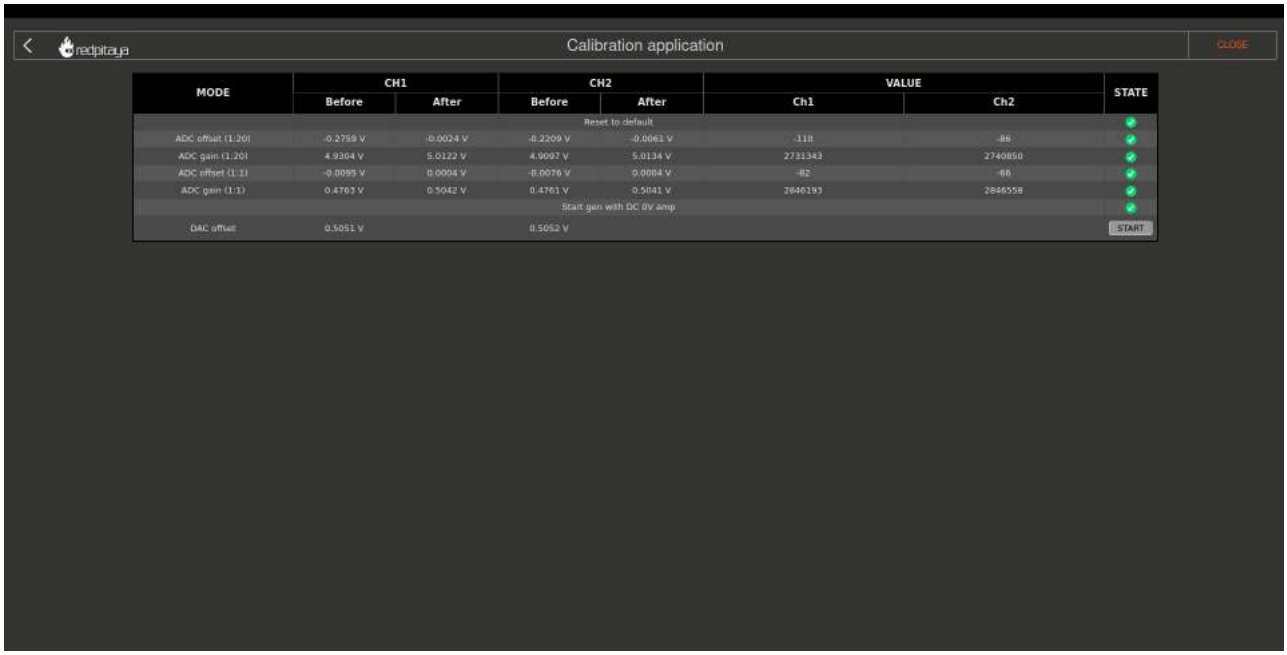
redpitaya
Calibration application
CLOSE
MODE
CH1
Before
After
CH2
Before
After
VALUE
Ch1
Ch2
STATE
Reset to default
ADC offset (1:20)
-0.2759 V
-0.0024 V
-0.2209 V
-0.0061 V
-110
-86
ADC gain (1:20)
4.9304 V
5.0122 V
4.9097 V
5.0134 V
2731343
2740850
ADC offset (1:1)
-0.0095 V
0.0004 V
-0.0076 V
0.0004 V
-82
-66
ADC gain (1:1)
0.4763 V
0.5042 V
0.4761 V
0.5041 V
2846193
2846558
Start gen with DC 0V amp
DAC offset
0.5051 V
0.5052 V
START

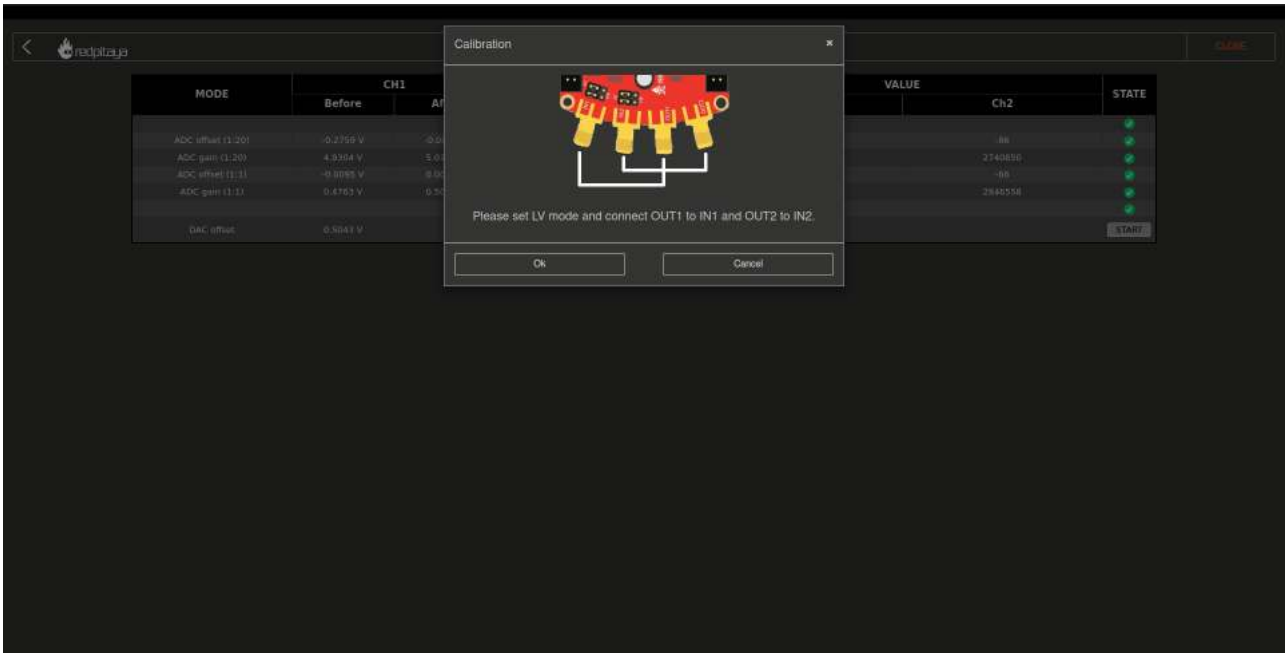
redpitaya
CLOSE
MODE
CH1
Before
VALUE
Ch2
STATE
START
Calibration
Please set LV mode and connect OUT1 to IN1 and OUT2 to IN2.
Ok
Cancel

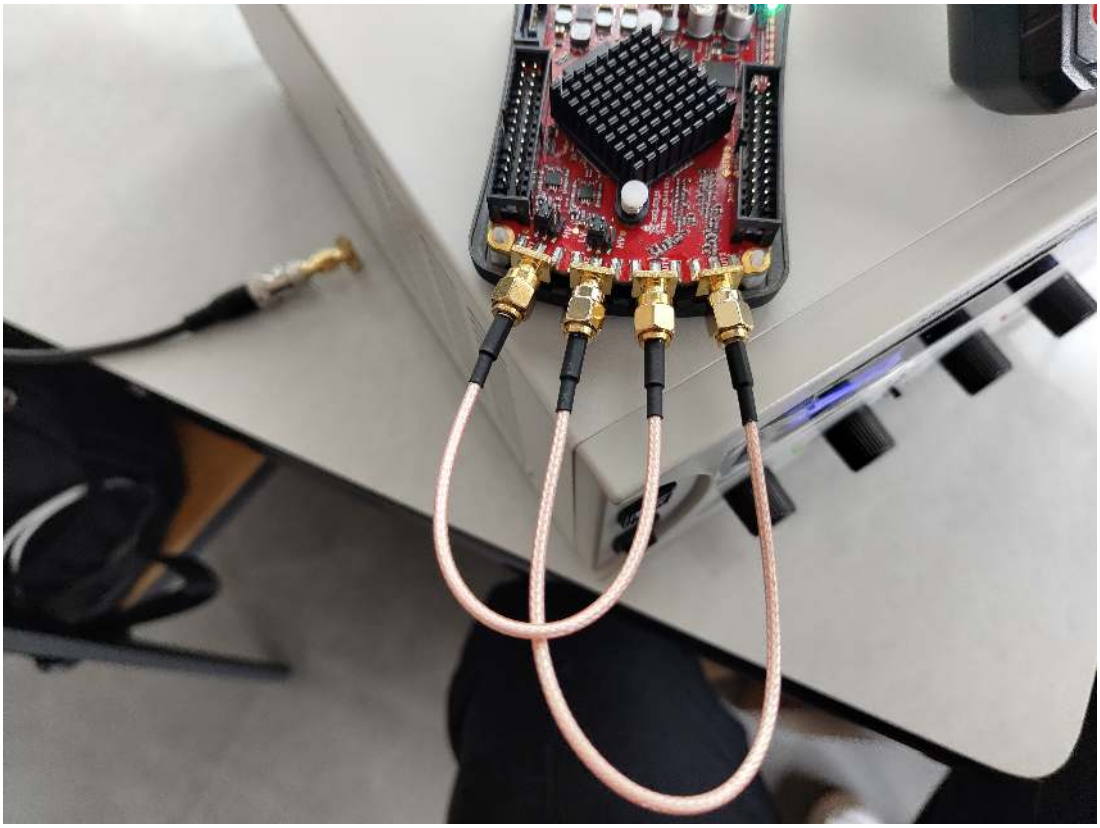

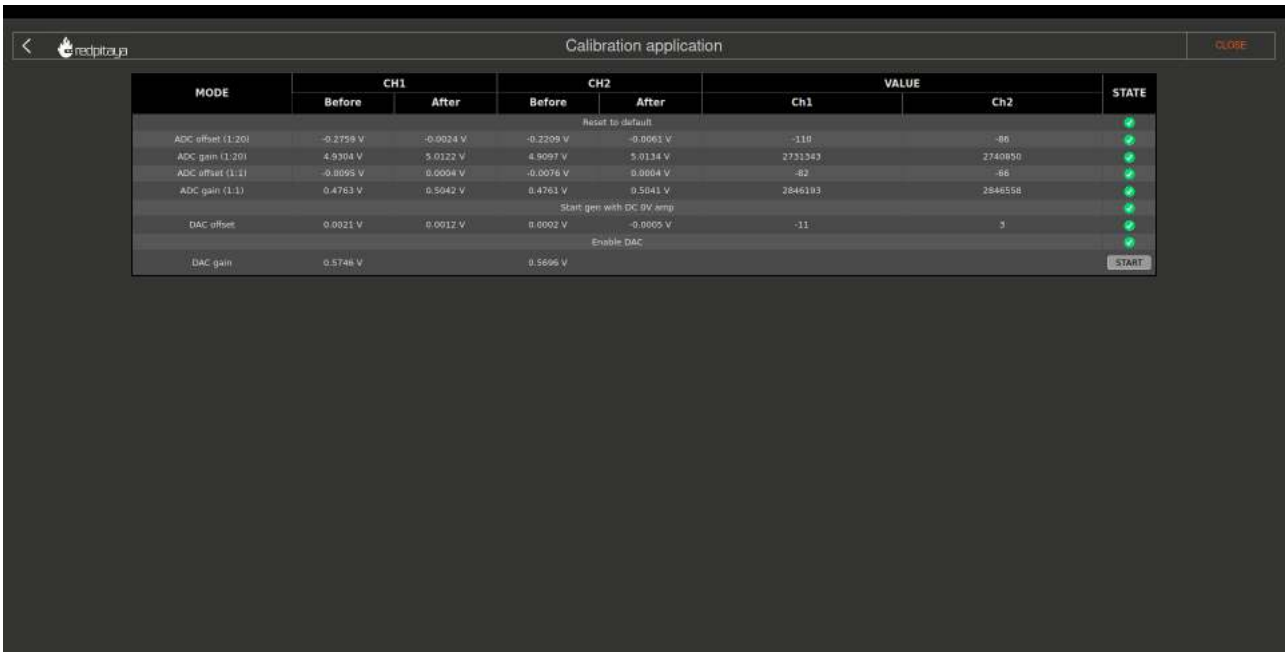
redpitaya
Calibration application
CLOSE
MODE
CH1
Before
After
CH2
Before
After
VALUE
Ch1
Ch2
STATE
Reset to default
ADC offset (1:20) -0.2759 V -0.0024 V -0.2209 V -0.0061 V -110 -86
ADC gain (1:20) 4.9304 V 5.0122 V 4.9097 V 5.0134 V 2731343 2740850
ADC offset (1:1) -0.0095 V 0.0004 V -0.0076 V 0.0004 V -82 -66
ADC gain (1:1) 0.4763 V 0.5042 V 0.4761 V 0.5041 V 2846193 2846558
Start gen with DC 0V amp
DAC offset 0.0021 V 0.0012 V 0.0002 V -0.0005 V -11 3
Enable DAC
DAC gain 0.5748 V 0.5696 V
START

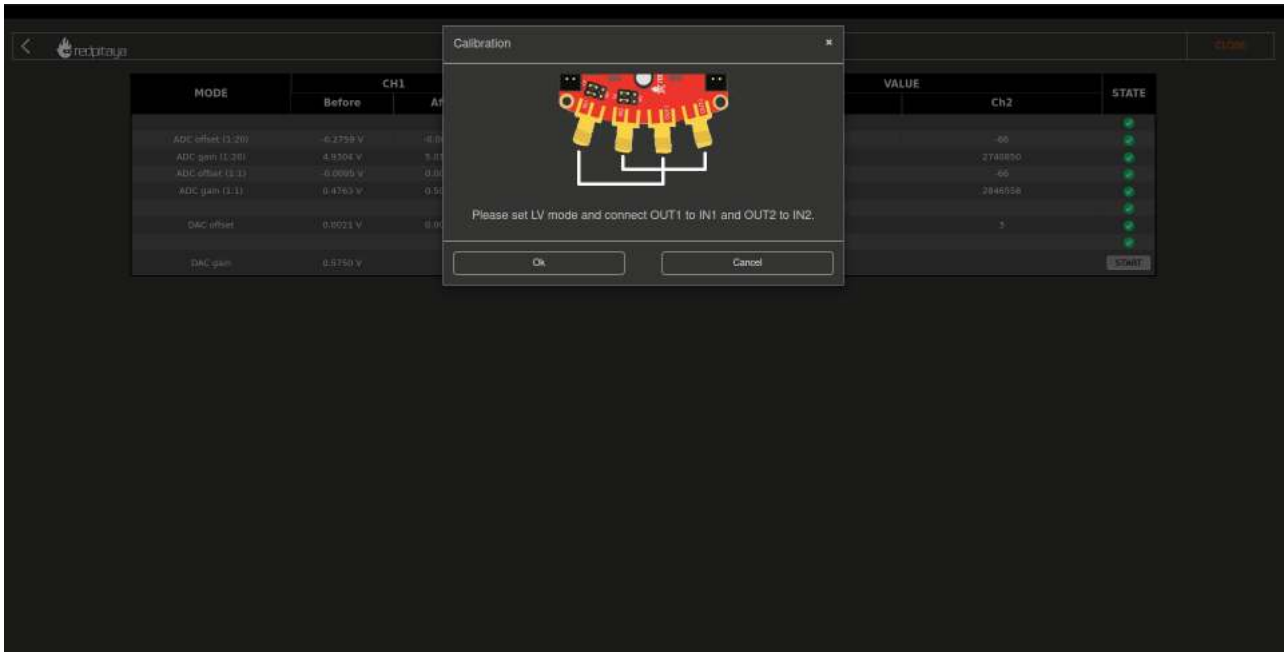

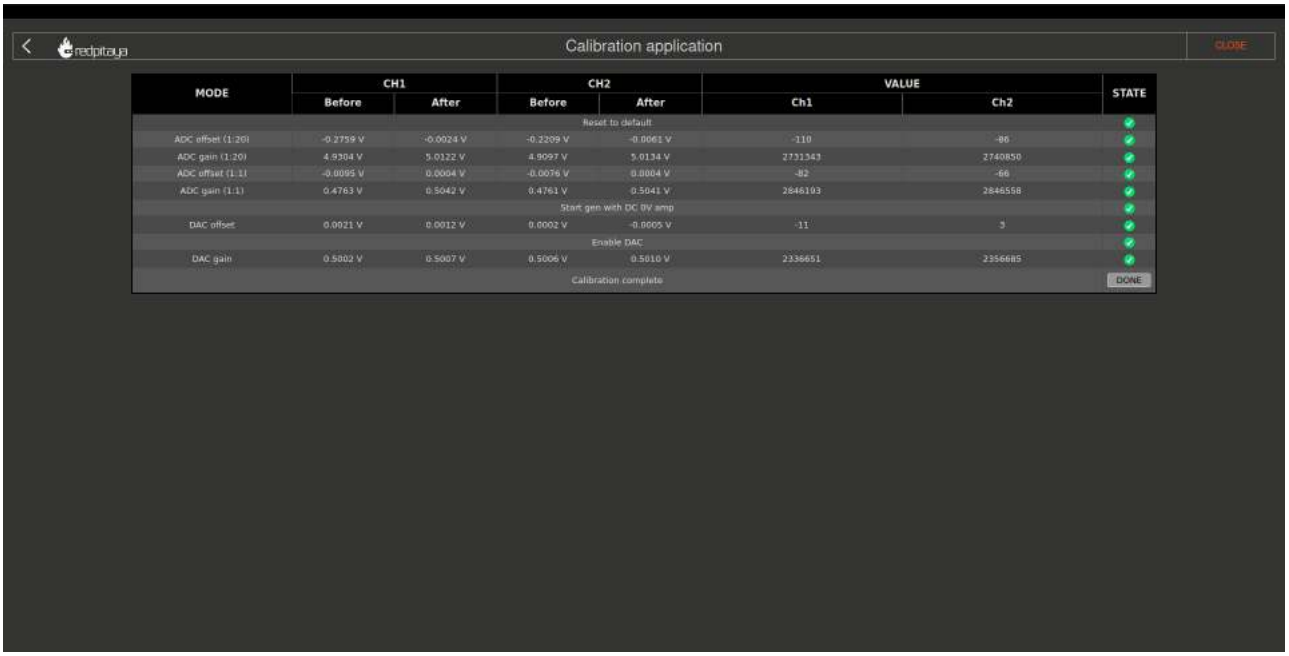

7. Check new Offset and Gain parameter in Manual Calibration settings

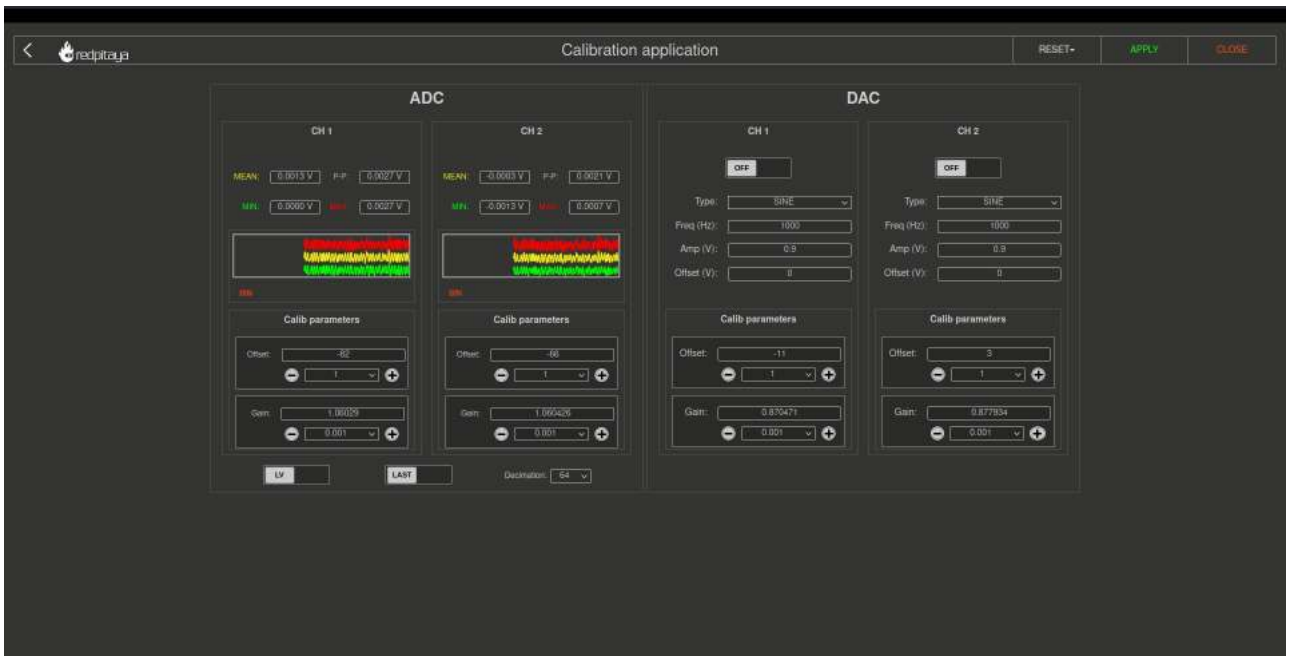
redpitaya
Calibration application
RESET
APPLY
CLOSE
ADC
CH 1
CH 2
MEAN:
0.0013 V
P-P
0.0027 V
MIN:
0.0000 V
MAX
0.0027 V
MEAN:
-0.0003 V
P-P
0.0021 V
MIN:
-0.0013 V
MAX
0.0007 V
Calib parameters
Offset:
-82
Gain:
1.00029
Offset:
-66
Gain:
1.000426
LV
LAST
Decimation:
64
DAC
CH 1
CH 2
OFF
Type:
SINE
Freq (Hz):
1000
Amp (V):
0.9
Offset (V):
0
Calib parameters
Offset:
-11
Gain:
0.870471
Offset:
3
Gain:
0.877934

BIBLIOGRAPHY

[Doc] Red Pitaya. *Red Pitaya Documentation.* https://redpitaya.readthedocs.io/en/latest/.

[ST125-14] Red Pitaya. *Red Pitaya STEMlab 125-14 product datasheet.* https://redpitaya.com/de/stemlab-125-14/.

[PC19] Marco Platzner and Plessl Christian. *FPGAs (Field Programmable Gate Arrays) im Rechenzentrum.* https://gi.de/informatiklexikon/fpgas-field-programmable-gate-arrays-im-rechenzentrum. 2019.

[DocHW] Red Pitaya. *Red Pitaya Hardware Documentation.* https://redpitaya.readthedocs en/latest/developerGuide/hardware/125-14/top.html.

[DocSW] Red Pitaya. *Red Pitaya Software Documentation.* https://redpitaya.readthedocs. en/latest/developerGuide/software/software.html.

[RS] Rhod and Schwarz. *Importance of deep memory in oscilloscopes.* https://www.rohde-schwarz.com/se/applications/importance-of-deep-memory-in-oscilloscopes-application-card_56279-409160.html.

[Git-RP] Red Pitaya. *GitHub repository of Red Pitaya.* https://github.com/RedPitaya/RedPitaya.

[OscSig] Red Pitaya. *Red Pitaya Oscilloscope and Signalgenerator Documentation.* https://redpitaya.readthedocs.io/en/latest/appsFeatures/applications/oscSigGen/osc.html.

[GitHub-MCPHA] Pavel Denim. *GitHub repositroy of the MCPHA.* https://github.com/pavel-demin/red-pitaya-notes/tree/master/projects/mcpha.

[GitLab-MCPHA] Günter Quast. *GitLab repositroy of the MCPHA customized by Günter Quast.* https://gitlab.kit.edu/guenter.quast/redpitaya-mcpha.

[kafe2] Günter Quast. *kafe2 documentation.* https://etpwww.etp.kit.edu/~quast/kafe2/htmldoc/index.html.

[Dem17] Wolfgang Demtröder. *Experimentalphysik 4: Kern-, Teilchen- und Astrophysik 5. Auflage.* Springer Spektrum, 2017. ISBN: 9783662528846.

[DK23] Guido Drexlin and Markus Klute. *Moderne Experimentalphysik III - Teilchen und Hadronen.* Lecture in Summer semester 2023. 2023.

[Pov14] Bogdan Povh et. al. *Teilchen und Kerne : Eine Einführung in die physikalischen Konzepte 9. Auflage.* Springer Spektrum, 2014. ISBN: 9783642378225.

[Wol23] Joachim Wolf. "Einführung in das Kern- und Teilchenphysikalische Praktikum". In: (2023).

[Col22] The KATRIN Collaboration. "Direct neutrino-mass measurement with sub-electronvolt sensitivity". In: (2022). DOI: https://doi.org/10.1038/s41567-021-01463-1.

[KW20] Hermann Kolanoski and Norbert Wermes. *Particle detectors: fundamentals and applications*. Oxford University Press, 2020. ISBN: 9780198858362.

[GM12] Rudlof Gross and Achim Marx. *Festkörperphysik, 1.Auflage*. De Gruyter Oldenbourg, 2012. ISBN: 9783486712940.

[Cow98] Glen Cowan. *Statistical data analysis : [with applications from particle physics]*. Oxford : Clarendon Press, 1998. ISBN: 0198501560.

[Sim] Hans Simonis. *Versuchsanleitung : Gamma-Spektroskopie*. https://etpwww.etp.kit.edu/~simonis/praktikum/p2/p2-versuchsanleitungen/Gammaspektroskopie.pdf.

[Zie10a] Eckert & Ziegler. *Recommended Nuclear Decay Data for Cs137*. https://www.ezag.com/fileadmin/ezag/user-uploads/isotopes/isotopes/Isotrak/isotrak-pdf/Decay_Schema_Data/Cs-137.pdf. 2010.

[Zie10b] Eckert & Ziegler. *Recommended Nuclear Decay Data for Ra226*. https://www.ezag.com/fileadmin/ezag/user-uploads/isotopes/isotopes/Isotrak/isotrak-pdf/Decay_Schema_Data/Ra-226.pdf. 2010.

[Did] Leybold Didactic. *Ra-226*. https://www.ld-didactic.de/software/524221en/.

[Age] International Atomic Energy Agency. *γ-ray energies and emission probabilities ordered by energy*. https://www-nds.iaea.org/xgamma_standards/genergiesb.htm.

[Zie10c] Eckert & Ziegler. *Recommended Nuclear Decay Data for Na22*. https://www.ezag.com/fileadmin/ezag/user-uploads/isotopes/isotopes/Isotrak/isotrak-pdf/Decay_Schema_Data/Na-22.pdf. 2010.

[Zie10d] Eckert & Ziegler. *Recommended Nuclear Decay Data for Co60*. https://www.ezag.com/fileadmin/ezag/user-uploads/isotopes/isotopes/Isotrak/isotrak-pdf/Decay_Schema_Data/Co-60.pdf. 2010.

[Qua] Günter Quast. *Skript: Funktionsanpassung mit der χ^2-Methode*. https://etpwww.etp.kit.edu/~quast/gq.

[Dee] DeepL. *Online-Übersetzungsdienst*. https://www.deepl.com/de/translator.

ACKNOWLEDGEMENT

I would like to express my special thanks to my supervisor for this thesis, Prof. Dr. Günter Quast. He was always open to any of my questions that arose during this study and I always received a prompt answer that was not only understandable and detailed, but also helped me to solve my problem. No matter how trivial the questions were, I was always welcome in his office, could always come around spontaneously and I always left with more knowledge and a better understanding. The same applies to my second supervisor, Dr. Joachim Wolf, who always helped me to solve problems with the experimental setup and he was always able to answer my questions about detectors and electronics. I would also like to thank Mr. Huppuch and Mr. Flühr, as well as Ms. Huck, who always gave me access to the physics lab, which allowed me to work independently and freely.

I would also like to extend a special thanks to my study group "Pizza Banane", especially to Niklas Reus and Niclas Riffert, with whom I have always worked on the exercise sheets since the first semester, discussed physical problems and who have answered my often unnecessary and pointless questions in hours of conversation, and who are now good friends of mine whom I really appreciate.
I would also like to thank my good friend Jan-Philipp Christ, who had to convince me to study physics since school and without whom I would probably have chosen a different technical degree. Without him, I would never have survived the first semester during the Corona lockdown, as he was able to answer any physical or mathematical question I had during our nightly gaming sessions.
Finally, I would like to thank my parents in a special way for always supporting me during my school time and degree and making sure that I could focus on my studies and always supported me in the best possible way and always encouraged me to achieve my goals.